

# **Computer Modeling and Simulation of Morphotropic Phase Boundary Ferroelectrics**

**Weifeng Rao**

Dissertation submitted to the faculty of the Virginia Polytechnic Institute and State  
University in partial fulfillment of the requirements for the degree of

Doctor of Philosophy

In

Materials Science and Engineering

Dr. Yu Wang, Committee Chair

Dr. Dwight D. Viehland

Dr. William T. Reynolds, Jr.

Dr. Alexander O. Aning

Dr. David Y. Gao

July 31, 2009  
Blacksburg, Virginia

Keywords: Phase Field Modeling, Ferroelectrics, Morphotropic Phase Boundary, Phase  
Coexistence, Domain Microstructure and Evolution, Domain Engineering,  
Piezoelectricity

# **Computer Modeling and Simulation of Morphotropic Phase Boundary Ferroelectrics**

**Weifeng Rao**

## **ABSTRACT**

Phase field modeling and simulation is employed to study the underlying mechanism of enhancing electromechanical properties in single crystals and polycrystals of perovskite-type ferroelectrics around the morphotropic phase boundary (MPB). The findings include:

(I) Coherent phase decomposition near MPB in PZT is investigated. It reveals characteristic multidomain microstructures, where nanoscale lamellar domains of tetragonal and rhombohedral phases coexist with well-defined crystallographic orientation relationships and produce coherent diffraction effects.

(II) A bridging domain mechanism for explaining the phase coexistence observed around MPBs is presented. It shows that minor domains of metastable phase spontaneously coexist with and bridge major domains of stable phase to reduce total system free energy, which explains the enhanced piezoelectric response around MPBs.

(III) We demonstrate a grain size- and composition-dependent behavior of phase coexistence around the MPBs in polycrystals of ferroelectric solid solutions. It shows that grain boundaries impose internal mechanical and electric boundary conditions, which give rise to the grain size effect of phase coexistence, that is, the width of phase coexistence composition range increases with decreasing grain sizes.

(IV) The domain size effect is explained by the domain wall broadening mechanism. It shows that, under electric field applied along the nonpolar axis, without domain wall

motion, the domain wall broadens and serves as embryo of field-induced new phase, producing large reversible strain free from hysteresis.

(V) The control mechanisms of domain configurations and sizes in crystallographically engineered ferroelectric single crystals are investigated. It reveals that highest domain wall densities are obtained with intermediate magnitude of electric field applied along non-polar axis of ferroelectric crystals.

(VI) The domain-dependent internal electric field associated with the short-range ordering of charged point defects is demonstrated to stabilize engineered domain microstructure. The internal electric field strength is estimated, which is in agreement with the magnitude evaluated from available experimental data.

(VII) The poling-induced piezoelectric anisotropy in untextured ferroelectric ceramics is investigated. It is found that the maximum piezoelectric response in the poled ceramics is obtained along a macroscopic nonpolar direction; and extrinsic contributions from preferred domain wall motions play a dominant role in piezoelectric anisotropy and enhancement in macroscopic nonpolar direction.

(VIII) Stress effects on domain microstructure are investigated for the MPB-based ferroelectric polycrystals. It shows that stress alone cannot pole the sample, but can be utilized to reduce the strength of poling electric field.

(IX) The effects of compressions on hysteresis loops and domain microstructures of MPB-based ferroelectric polycrystals are investigated. It shows that longitudinal piezoelectric coefficient can be enhanced by compressions, with the best value found when compression is about to initiate the depolarization process.

Dedicated to my parents, wife, and sister  
and to my lovely daughters, Sophia C. Rao and Cindy Y. Rao

## ACKNOWLEDGMENTS

I would like to express my sincere gratitude to my advisor Dr. Yu U. Wang for his faith, guidance and support throughout the course of my Ph.D. research and also for giving me the opportunity to work on these interesting topics. I will always be thankful for his enthusiasm, wisdom and knowledge as well as the motivation and challenge he gave me.

I would also like to thank Dr. Yongmei Jin for her encouragement and her great help on writing parallel programs. She generously shared her knowledge and experience in every aspect of the scientific research. Without her help, my research would not go smoothly.

Thanks to Dr. Dwight Viehland, Dr. Bill Reynolds, Dr. Alex Aning and Dr. David Gao for serving on my committee and taking time out of their busy schedules to evaluate my work. They are greatly appreciated for their continuous help during my entire Ph.D. study.

I would like to express my gratitude to my colleague, Tianle Cheng and Kewei Xiao, for all the helpful discussions, and all my fellow graduate students in the MSE department for all the fun that we have shared together. Thanks also to all the friends I have come to know in Blacksburg, who made my life here more colorful.

Thanks to the Division of Materials Research of the National Science Foundation for funding of my work. The computing resources of System X at Virginia Tech, DataStar at San Diego Supercomputer Center, and LoneStar at Texas Advanced Computing Center are gratefully acknowledged.

I owe my sincere appreciation to my parents and my sister, whose support and encouragement makes me get this far. Last but not least, my special thanks go to my dear wife, Xiaoling Yang, for her love, company, understanding, and persistent support.

# TABLE OF CONTENTS

Abstract .....	ii
Acknowledgments .....	v
Table of Contents.....	vi
List of Figures .....	viii
List of Tables .....	xiii
I. Introduction.....	1
I.1. Background .....	1
I.2. Objectives and Arrangements .....	10
I.3. References .....	11
II. Phase Field Model for Ferroelectric Materials .....	15
II.1. Formulation .....	15
II.2. Numerical Simulations .....	22
II.3. References .....	23
III. Phase-Coexisting Domain Microstructure .....	25
III.1. Introduction .....	25
III.2. Coherent Phase Decomposition .....	28
III.3. Bridging Domain Mechanism .....	36
III.4. Grain Size Effect .....	46
III.5. References .....	54
IV. Crystallographic Domain Engineering.....	57
IV.1. Introduction .....	57
IV.2. Domain Wall Broadening Mechanism .....	60
IV.3. Engineering of Domain Configuration.....	68
IV.4. Stabilization of Domain Microstructure.....	81
IV.5. References .....	93
V. Piezoelectricity under External Fields.....	95
V.1. Introduction .....	95
V.2. Anisotropic Piezoelectricity .....	97

V.3.	Domain Microstructure under Stresses .....	111
V.4.	Piezoelectricity under Electric and Mechanical Fields .....	122
V.5.	References .....	131
<b>VI.</b>	<b>Conclusions and Future Work .....</b>	<b>132</b>
VI.1.	Conclusions .....	132
VI.2.	Future Work .....	134
<b>Appendix</b>	<b>.....</b>	<b>138</b>
A.1.	Intrinsic Electrostrictive and Piezoelectric Properties.....	138
A.2.	References .....	154

## List of Figures

Figure 1-1.	Piezoelectric effects in ferroelectrics (after ref. 2) .....	2
Figure 1-2.	Schematic phase diagram of perovskite pseudo-binary solid solutions.....	2
Figure 1-3.	Real phase diagrams for PZT (upper, after ref. 3.), PMN-PT (lower left, after ref. 4), and PZN-PT (lower right, after ref. 5), where the MPBs are highlighted in red.....	5
Figure 3-1.	(After ref. 7). Computed equilibrium phase diagrams for PZT solid solutions exhibiting ideal behavior with atomic exchange mixing parameter $w=0$ (a); exhibiting nonideal behavior with $w=2.75$ (b). Both are peritectoid diagrams with invariant lines located at 617 K in (a) and 592 K in (b). .....	30
Figure 3-2.	(After ref. 1). Computer simulation of coherent microstructures of phase decomposition in PZT near MPB at room temperature. ....	31
Figure 3-3.	Kinetic pathways of phase decomposition in PZT. ....	37
Figure 3-4.	(After ref. 2). Computer simulation of bridging domains and mosaic domain microstructures of coexisting phases in PZT system at room temperature with near MPB compositions: (a) $x=0.49$ and (b) $x=0.50$ . .....	40
Figure 3-5.	Free energies of ferroelectrics around MPB in the polarization space (calculated from ref. 30) on (a) the rhombohedral side, and (b) tetragonal side.....	43
Figure 3-6.	(After ref. 3). Computer simulation of grain size-dependent phase coexistence phenomenon around MPB in ferroelectric polycrystals. ..	48
Figure 3-7.	(After ref. 3). Computer simulation of grain size- and composition-dependent phase-coexisting domain microstructures around MPB in ferroelectric polycrystals. ....	50
Figure 3-8.	Volume fraction of tetragonal phase versus the mole fraction of PT for $N=256$ . .....	54



Figure 4-1.	(After ref. 1). Domain size effect in [111]-oriented tetragonal barium titanate single crystals. ....	62
Figure 4-2.	(After ref. 1). Computer simulation of domain wall broadening behavior under electric field along non-polar axis. ....	63
Figure 4-3.	A sequence of domain wall broadening under electric field along non-polar axis. ....	65
Figure 4-4.	Energy space of MPB-based ferroelectrics on tetragonal side (a) without and (b) with electric field applied along the nonpolar [111] direction. ....	70
Figure 4-5.	Domain evolution and formation of (100) rhombohedral twins in MPB-based ferroelectric single crystal of rhombohedral composition cooling across Curie temperature with an electric field applied along the non-polar [100] direction. ....	71
Figure 4-6.	Domain evolution and formation of (110) rhombohedral twins in MPB-based ferroelectric single crystal of rhombohedral composition cooling across Curie temperature with an electric field applied along the non-polar [110] direction. ....	72
Figure 4-7.	Domain evolution and formation of (110) tetragonal twins in MPB-based ferroelectric single crystal at a tetragonal composition cooling across the Curie temperature with an electric field applied along the non-polar [111] direction. ....	73
Figure 4-8.	The dependence of average domain size (domain wall density) on the magnitude of electric field applied along non-polar [111] direction at room temperature. ....	75
Figure 4-9.	The effects of non-polar [111] electric field on energy difference for different variants versus the polarization length for PZT of tetragonal composition $x = 0.6$ (calculated from ref.21). ....	77
Figure 4-10.	The dependence of average domain size (domain wall density) on the percentage of initial offset under a small non-polar [111] electric field ( $\sim E_a$ ). ....	79
Figure 4-11.	The dependence of average domain size (domain wall density) on	

	the magnitude of electric field applied along non-polar [111] direction at 250°C.....	80
Figure 4-12.	Domain stabilization and recovery behaviors of an aged tetragonal PZT of composition $x=0.6$ during a rapid heating-cooling cycle. The internal bias electric field is about 1.0 kV/cm.....	85
Figure 4-13.	Random domain evolution of an insufficiently aged tetragonal PZT of composition $x=0.6$ during a rapid heating-cooling cycle. The internal bias electric field is about 0.05 kV/cm.....	87
Figure 4-14.	Statistical results on the domain microstructure recovery of 10 aged tetragonal PZT samples of composition $x=0.6$ during a rapid heating-cooling cycle. ....	88
Figure 4-15.	Domain stabilization and recovery behaviors of an aged tetragonal PZT of composition $x=0.6$ during a rapid heating-cooling cycle. The internal bias electric field is about 0.42 kV/cm.....	89
Figure 4-16.	Domain stabilization and recovery behaviors of an aged tetragonal PZT of composition $x=0.6$ during a rapid heating-cooling cycle. The internal bias electric field is about 0.065 kV/cm.....	91
Figure 5-1.	A typical domain microstructure in a MPB-based ferroelectric polycrystal of randomly oriented 64 grains. ....	99
Figure 5-2.	Two typical electric field-strain curves for training MPB-based ferroelectric polycrystals. ....	101
Figure 5-3.	Longitudinal strain versus strength of electric field for poled ferroelectric polycrystals around MPB.....	102
Figure 5-4.	A typical domain microstructure for a poled tetragonal PZT polycrystal ( $x = 0.65$ ). ....	103
Figure 5-5.	Electromechanical response of poled ferroelectric polycrystals. (a) Longitudinal strain versus the strength of electric field applied along $D_a$ , where $\gamma$ increases from $0^\circ$ to $90^\circ$ at a pace of $5^\circ$ . For clarity, the curves are shifted with different constants. (b) Normalized strain difference versus $\gamma$ , read from figures like (a). ....	106
Figure 5-6.	Coordinate system for correlating the crystallographic $\langle 100 \rangle$ axes	

	(black axes) to the global coordinate system (blue axes) in each individual grain.....	107
Figure 5-7.	Strain change induced by domain wall motions, where red is the numerical solution for a randomly distributed polycrystal, green is the analytical solution for a polycrystal with fixed [001], and the blue is $\pi / 2.4$ times of green curve. ....	109
Figure 5-8.	Macroscopic responses of MPB-based ferroelectric polycrystals under mechanical field, where (a) is for averaged polarization versus stress fields, (b) is for stress-strain curves, and (c) is two selected curves in (a), for whom the domain evolution will be discussed.....	112
Figure 5-9.	Evolution of the domain microstructure of a MPB-based ferroelectric polycrystal under pure mechanical stresses along the horizontal direction.....	116
Figure 5-10.	Evolution of domain microstructure of a MPB-based ferroelectric polycrystal under pure mechanical stresses along the vertical direction.....	117
Figure 5-11.	Average polarization of a MPB-based ferroelectric polycrystal under different strengths of externally applied electric field. ....	121
Figure 5-12.	One cycle of typical hysteresis and butterfly loops for MPB-based ferroelectric polycrystals under constant compressions.....	123
Figure 5-13.	(a)Maximum polarizations (red dots), remnant polarizations (green triangles), coercive fields (pink square), and (b) longitudinal piezoelectric coefficients of MPB-based ferroelectric polycrystals under constant compressions read from Fig. 5-12. ....	125
Figure 5-14.	Domain microstructures of a MPB-ferroelectric polycrystal under fixed compression and variable strengths of electric fields. ....	127
Figure A-1.	(After ref.1) Lattice parameters of tetragonal and rhombohedral phases of PZT within respective phase stability composition ranges at room temperature, as determined from the diffraction data and Rietveld refinement results reported in the literature. <sup>16-30</sup> .....	144

Figure A-2.	(After ref.1) Spontaneous polarization of tetragonal (blue symbols) and rhombohedral (red symbols) phases of PZT within respective phase stability composition ranges at room temperature, as determined from Eqs. (A.8) and (A.9) and the Rietveld refinement results reported in the literature. <sup>19,20,22-24,27,29,30</sup> .....	145
Figure A-3.	(After ref.1) Electrostrictive coefficients of PZT at room temperature, as determined from the diffraction data and Rietveld refinement results reported in the literature. <sup>16-30</sup> .....	147
Figure A-4.	(After ref.1) Calculated lattice parameters of tetragonal and rhombohedral phases of PZT by using the LGD theories, <sup>3-9</sup> as shown in black and green lines.....	149
Figure A-5.	(After ref. 2) Rhombohedral lattice parameter, $a_r$ (red symbols), and weighted average of tetragonal lattice parameters, $(c_t + 2a_t)/3$ (blue symbols), of PZT as a function of composition at room temperature, as determined from the diffraction data and Rietveld refinement results reported in the literature. <sup>16-30</sup> .....	150
Figure A-6.	(After ref. 1) Effect of electrostrictive coefficient ratio $Q_{44}/Q_{11}$ on piezoelectric anisotropy of rhombohedral PZT at MPB composition $x=0.46$ . .....	152
Figure A-7.	(After ref. 1) Effect of electrostrictive coefficients $Q_{11}$ , $Q_{12}$ and $Q_{44}$ on piezoelectric anisotropy of rhombohedral PZT at composition range $0.4 \leq x \leq 0.48$ . .....	154

## List of Tables

Table 1.	Parameter values of the functions in Eq. (26) obtained by fitting to the simulation data.....	51
----------	---	----

# Chapter I

## Introduction

### I.1. Background

Ferroelectrics, first reported in 1921 by Valasek,<sup>1</sup> are a family of functional materials with spontaneous polarizations and domain microstructures that can convert energies of mechanical to electric and vice versa under externally applied fields. As demonstrated by Fig. 1-1, they are widely employed to manufacture piezoelectric and electrostrictive actuators, sensors, transducers, et al.<sup>2</sup>

For engineering applications, the perovskite-type solid solutions ( $ABO_3$ ), such as  $Pb(Zr_{1-x}Ti_x)O_3$  (PZT),<sup>3</sup>  $Pb[(Zn_{1/3}Nb_{2/3})_{1-x}Ti_x]O_3$  (PZN-PT),<sup>4</sup> and  $Pb[(Mg_{1/3}Nb_{2/3})_{1-x}Ti_x]O_3$  (PMN-PT),<sup>5</sup> are of the most interest. The schematic phase diagram, Fig. 1-2, shows that, at certain temperature, the paraelectric cubic phase will transform to rhombohedral or tetragonal phases at low or high PT composition, respectively. These two phases are separated by a nearly vertical phase boundary, called morphotropic phase boundary (MPB). The real phase diagrams are shown in Fig. 1-3, with the MPBs highlighted in red. Because the best piezoelectric properties of these materials are obtained at compositions

in the vicinity of their MPBs,<sup>3,6-8</sup> the underlying mechanism for the enhanced properties around MPBs is a question of both scientific and technological importance.

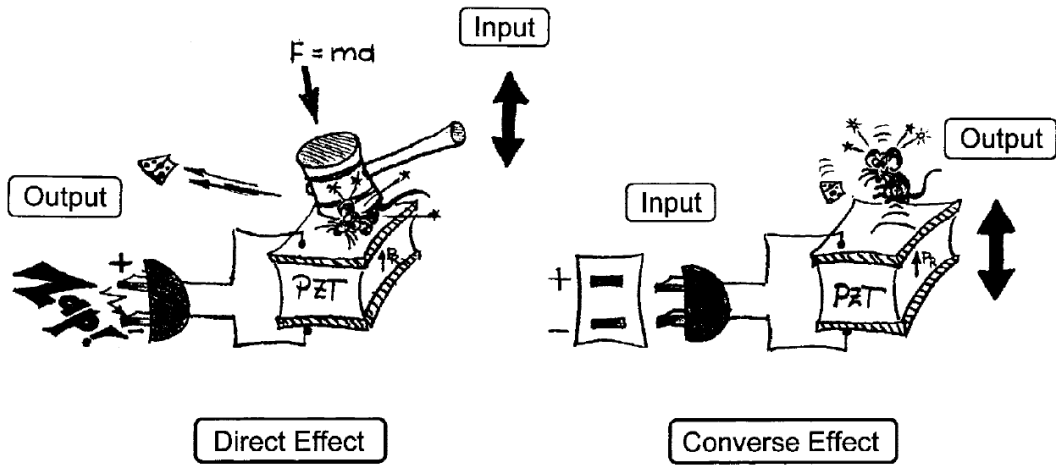


FIG. 1-1. Piezoelectric effects in ferroelectrics (after ref. 2).

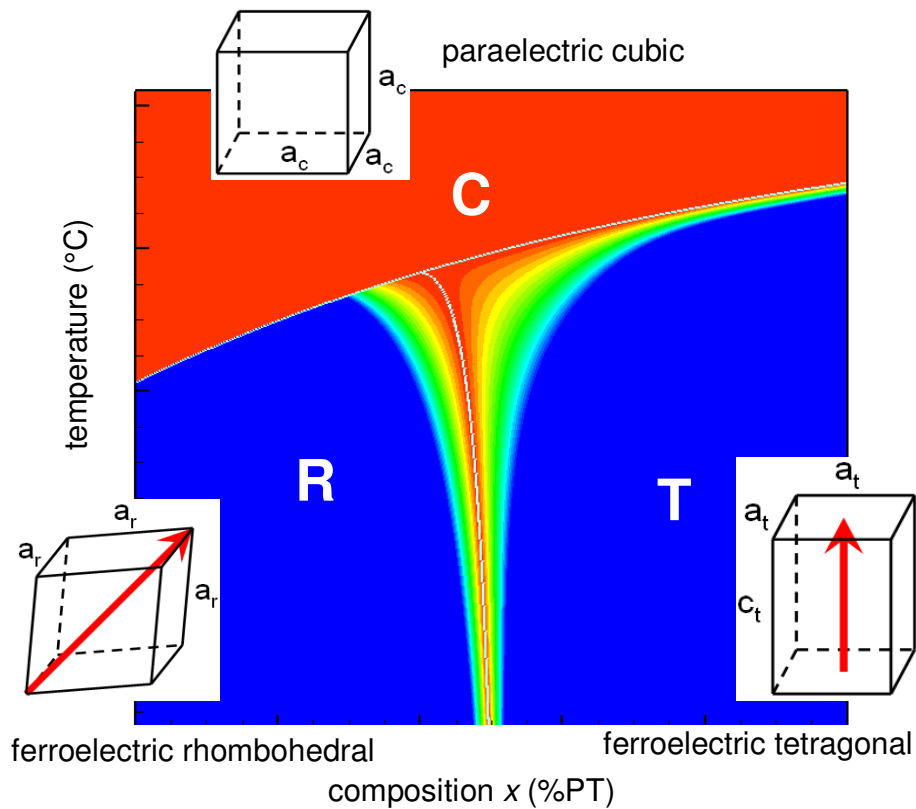


FIG. 1-2. Schematic phase diagram of perovskite pseudo-binary solid solutions.

There are two methods available to theoretically analyze the ferroelectric phase transformation. One is the microscopic theory in terms of crystal lattice dynamics, called Soft-Modes theory,<sup>9,10</sup> another is the macroscopic, thermodynamic theory, which can successfully describe the successive phase transitions in BaTiO<sub>3</sub> single domain single crystal.<sup>11</sup> But because of the complication of the mesoscale domain microstructure around MPBs and its evolution under externally applied fields, the origin of the exceptional properties around the MPBs cannot be explained by aforementioned approaches, and is yet to be clarified, in spite of the investigations over decades.

Recently, new intermediate MPB phases were observed by high-resolution X-ray and neutron diffractions,<sup>12</sup> which renews the interest in the phase diagrams of these ferroelectric solid solutions. Some investigators attribute the origin of the exceptional properties to the presence of new intermediate MPB phases.<sup>12</sup> It is known that the phases in ferroelectric solid solutions are usually identified by x-ray or neutron powder diffractions. When the microstructure size is much smaller than the coherence length of radiations, i.e., nanoscale microstructures, scattered waves from individual nanodomains coherently superimpose in diffraction, where the resultant diffraction intensity profiles only reflect the average diffraction effect of crystal lattices over multiple nanodomains. Recent nanotwin diffraction analysis shows that nanotwins of tetragonal and rhombohedral phases are perceived by x-ray and neutron diffractions as monoclinic phases, where adaptive Bragg reflection peaks appear between the conventional twin peaks of coarse domains, and the positions of the new peaks are determined by the relative thicknesses of nanotwin variants.<sup>13</sup> Such extraordinary diffraction peaks cannot be explained by conventional diffraction theory of coarse domains, and an introduction of



monoclinic phase is found to improve the Rietveld refinement of diffraction data, which leads to the report of new monoclinic phase.<sup>12</sup>

It is worth noting that the monoclinic lattice corresponds to the average symmetry of the nanotwins and exhibits intrinsic lattice parameter relationships,<sup>14,15</sup> as predicted by both diffraction analysis<sup>13</sup> and crystallographic analysis through nanodomain averaging.<sup>14,15</sup> Moreover, nanotwins of tetragonal and rhombohedral phases with domain sizes about 10nm have recently been directly observed. Experiments of transmission electron microscopy (TEM) in combination with selected area electron diffraction (SAED) and convergent beam electron diffraction (CBED) observe nanotwins of tetragonal phase with {101} twin plane<sup>16</sup> and rhombohedral phase with {110} twin plane<sup>17</sup> with average size ~10nm in ferroelectric PMN-PT; in particular, the high-resolution electron microscopy (HREM) together with image simulation provide the atomic-resolution imaging of nanotwins of rhombohedral phase in PMN-PT.<sup>17</sup> These nanotwins appear as monoclinic  $M_C$  and  $M_B$  phases, respectively, in previous diffraction experiments. Nanodomains with typical size ~10nm are also observed in ferroelectric PZT by complementary TEM, SAED, CBED, electron paramagnetic resonance (EPR) and high-resolution synchrotron X-ray diffraction experiments;<sup>18-21</sup> most importantly, the high-resolution diffraction combined with TEM imaging establish a direct correlation between the appearance of extraordinary diffraction peak profiles and the formation of nanodomains;<sup>19,20</sup> although the new reflection peaks suggest a monoclinic phase, CBED and EPR only detect rhombohedral and tetragonal phases, while monoclinic phase is not observed.<sup>19,20</sup>

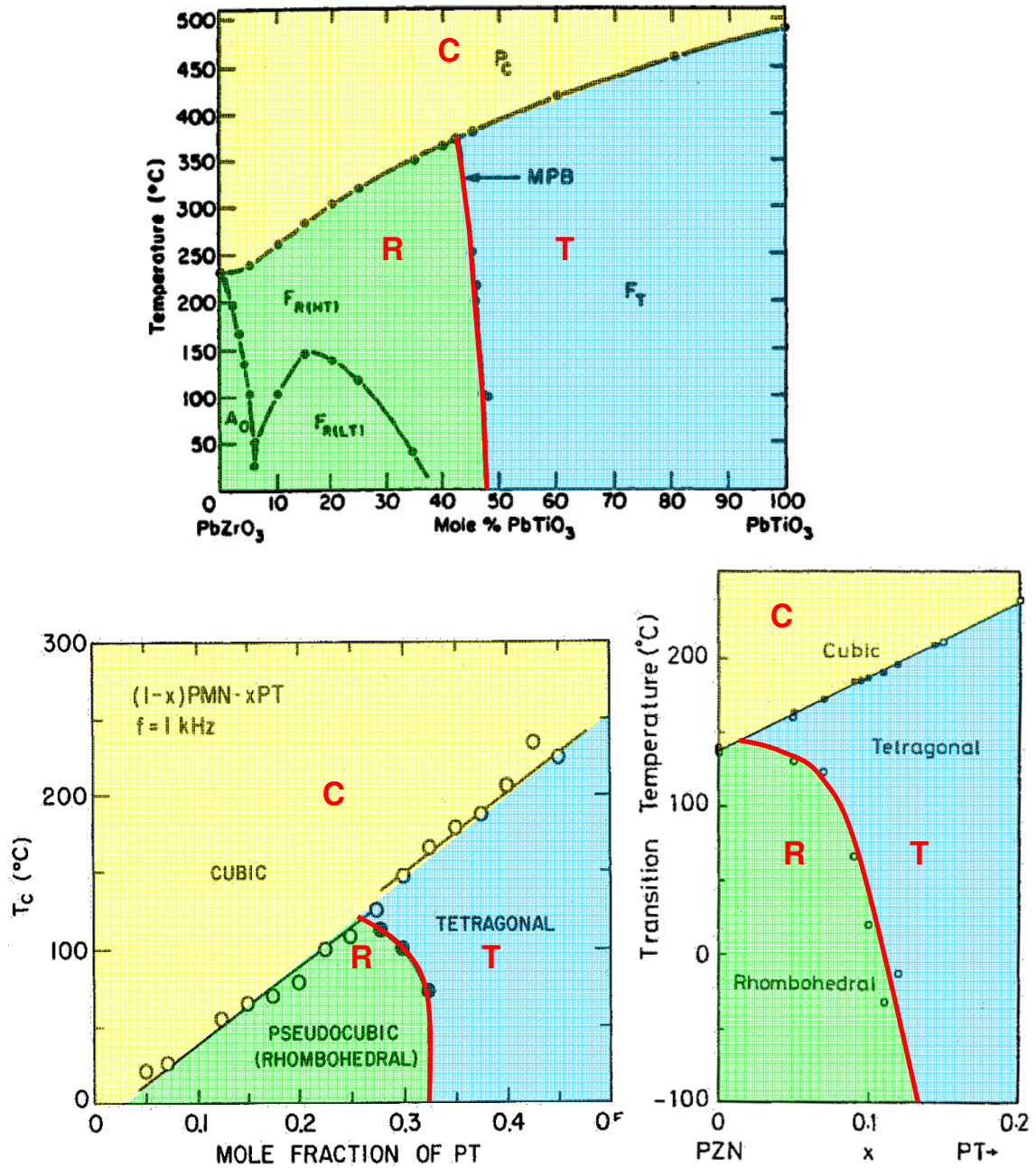


FIG. 1-2. Real phase diagrams for PZT (upper, after ref. 3.), PMN-PT (lower left, after ref. 4), and PZN-PT (lower right, after ref. 5), where the MPBs are highlighted in red.

It is noteworthy that monoclinic  $M_A$ ,  $M_B$ ,  $M_C$  phases have been reported based on high-resolution X-ray and neutron diffraction experiments on PZT, PMN-PT and PZN-

PT,<sup>12</sup> where the observed extraordinary peak patterns cannot be explained by the conventional diffraction theory of coarse-domained materials. These experimental findings<sup>16-21</sup> clarify the nanotwin nature of these monoclinic phases, demonstrate the coherent scattering and interference effects of nanodomain microstructures, and support the nanotwin diffraction theory.<sup>13</sup> Without taking into account the nanoscale domain microstructures, the diffraction data have been misinterpreted and led to identification of wrong phase. In order to correctly interpret diffraction data and identify the phases, it is crucial to know the nanodomain microstructures.

Meanwhile, because rhombohedral and tetragonal phase coexistence is commonly observed and expected from the Gibbs phase rule of equilibrium thermodynamics,<sup>22</sup> some investigators conceptually attributed the origin of the exceptional properties around MPBs to the phase coexistence. Insights have been gained from different perspectives, e.g., the range of phase coexistence was considered from the idea of the relative stability and metastability, or the overlapped existing ranges, of coexisting phases near MPB;<sup>23</sup> the coexisting phases (two end members) were shown to have the constant lattice parameters over the coexisting range, respectively, and the relative amounts could be calculated from defined edges of coexisting range through the lever rule,<sup>24</sup> the origin of the phase coexistence was suggested as a natural result of the compositional fluctuation during the processing;<sup>25</sup> the molar fractions of two coexisting phases were calculated by assuming that the statistical distribution functions are related to the effective solid angles (geometrical constraints) and the free energy difference (energy considerations) associated with these two phases;<sup>26</sup> the progression of the range of local structural order, from short-range to long-range and back to short-range structural order across the MPB,

was proposed to explain the adjacent phases and the associated MPB;<sup>27</sup> the equilibrium phase diagram satisfying Gibbs phase rule was predicted through the peritectoid reaction by treating the PZT system as a regular solution and combining the conventional Landau-Ginzburg-Devonshire (LGD) free energy function<sup>11</sup> with positive enthalpy of formation<sup>28</sup> and entropy of mixing;<sup>22</sup> the dramatic domain wall energy reduction and the nanodomain formation were expected by the inherent vanishing of the orientational anisotropy near MPB.<sup>29</sup>

While these studies together provide a broad aspect of MPB phase coexistence phenomenon, none of them considers the formation of ferroelectric and ferroelastic domain microstructures and its role in phase coexistence. These investigations are based on local free energy analyses within conventional Gibbsian thermodynamics, and do not consider the dependence of total system free energy on domain microstructures through long-range electrostatic and elastostatic interactions.

It is well known that the ferroelectric behaviors are profoundly affected by the heterogeneity of the polar domain microstructures and their evolutions, which are further complicated by the fact of the coexistence of two dissimilar phases (tetragonal and rhombohedral) in polycrystalline ferroelectrics around MPBs. For better understanding of the underlying mechanism of the piezoelectric responses of ferroelectric single crystals and polycrystals in service conditions, it is required to investigate the polar domain configurations and their evolution in absence and presence of externally applied fields. Given the difficulties in direct experimental observations and the complexity in theoretical treatments, it is thus highly desired to conduct computer modeling and simulation of MPB ferroelectrics.

A successful model capable of simulating phase transition should be able to treat microstructures, featured as domain size, shape and spatial arrangements. It should also be able to treat the microstructure evolution to reduce the total free energy, consisting of chemical free energy, interfacial energy, electrostatic energy and elastic strain energy.<sup>30</sup>

Some computer simulations that are based on constitutive laws and ad hoc switching criteria, e.g., finite element methods, are capable of studying the macroscopic hysteresis phenomena of ferroelectric materials, by explicitly treating the phase boundaries as sharp interfaces,<sup>30</sup> assuming each individual area is in single domain state,<sup>31</sup> or pre-determined (laminated) domain microstructures.<sup>32</sup> However, such approach will encounter serious difficulties when it formulates the interfacial movements as a time-dependent boundary problem, which makes it impractical in complicated phase transition simulation.<sup>30</sup> Since the domain microstructures can only evolve in the pre-decided ways, the constitutive approaches are thus not suitable for gaining insights on the mesoscale ferroelectric domain microstructures, which are even more complicated in the vicinity of MPBs, due to the presence of phase coexistence.

In comparison, the phase-field model can naturally describe the mesoscale morphological and microstructure evolution, without explicitly tracking the interface. Based on Ginzburg-Landau<sup>33, 34</sup> and Cahn-Hilliard<sup>35</sup> theories, the free energy functional of microstructures is constructed by a set of field variables crossing the interfacial regions. This approach circumvents the complication associated with moving interface and is thus easy for numerical implementation. With a simple and elegant description of evolving microstructures, it makes it possible to simulate various realistic physical processes, including solidification, solid-state structural phase transformations, grain

growth and coarsening, domain formations and evolutions, pattern formation on surfaces, dislocation microstructures, crack propagation, and electromigration.<sup>30</sup> It also has been shown that this method is one of the most suitable approaches to study the complex phase transitions/domain structures in ferroelectrics, see ref. 36 for a recent review on its applications on ferroelectric thin films.

The phase-field model is recently employed to investigate the domain microstructures of coexisting metastable and stable phases in single crystals of MPB-based ferroelectrics in inhomogeneous system involving configuration-dependent long-range elastostatic and electrostatic interactions.<sup>37-38</sup> The modeling and simulations on displacive phase transformation (diffusionless)<sup>37</sup> and coherent phase decomposition (diffusional)<sup>38</sup> show that the electrostatic and elastostatic interactions play significant roles in the phase coexistence around MPBs through the formation of coupled ferroelectric and ferroelastic domain microstructures. In particular, it shows that, due to the small bulk free energy gap between metastable and stable phases in the vicinity of MPBs, mosaic domain microstructures composed of coexisting phases spontaneously form in compositionally homogeneous system without compositional fluctuation, which effectively reduce the total free energy, including bulk free energy, domain wall energy, long-range electrostatic and elastostatic energies. It has been shown that the mosaic domain microstructures can be stabilized in polycrystalline ferroelectrics by the constraints imposed by grain boundaries, and is thus corresponding to an energy minimum state.<sup>39</sup> The mosaic domain microstructure subjected to an externally applied electric field is thus capable of returning to its original state upon the removal of external field, which provide a ferroelectric shape memory effect.<sup>40</sup> It is also revealed that, due to phase coexistence, large macroscopic

electromechanical response can be anisotropically produced in MPB-based ferroelectric polycrystals.<sup>40</sup> Similar phase coexistence phenomenon is also reported in the computer modeling and simulation studies of epitaxially strained ferroelectric thin films.<sup>41</sup>

## **I.2. Objectives and Arrangements**

The objectives of this dissertation are to develop a phase-field model for studying the MPB-based ferroelectrics, discuss issues when applying this model to quantitatively investigate the domain microstructures and the underlying mechanism for enhanced electromechanical properties around MPBs, present obtained results on single crystals and polycrystals, and outline the directions of further research. In particular, efforts will be placed on understanding the formation of multi-phase domain microstructures cooled with or without external electric fields, the evolutions of the obtained domain microstructures under the externally applied fields, and the resulted electromechanical properties in MPB-based single crystals and polycrystals. The possibility of optimizing and stabilizing the preferred domain microstructures in single crystals that give better electromechanical properties will be explored, as well as utilizing piezoelectric anisotropy in untextured polycrystalline ferroelectrics.

A general three dimensional phase field model for ferroelectric polycrystals will first be described in Chapter II. This model will then be applied to study the phase-coexisting domain microstructures of MPB-based ferroelectric single crystals and polycrystals in Chapter III, including the coherent phase decomposition (diffusional),<sup>38</sup> the displacive phase transformation (diffusionless),<sup>37</sup> and the grain size effects on the composition

width of phase coexistence range.<sup>39</sup> Chapter IV will be focused on investigating the best electromechanical properties of the MPB-based single crystals through domain engineering, in which a domain wall broadening mechanism for explaining the domain size effect<sup>42</sup> will be first presented, followed by controlling the domain configurations and sizes by applying external electric fields upon cooling,<sup>43</sup> and stabilizing the engineered domain microstructures through the aged short-range ordering of charged point defects.<sup>44</sup> The utilization of the best piezoelectric properties of MPB-based ferroelectric polycrystals will be discussed in Chapter V, where the poling-induced single-crystal-like piezoelectric anisotropy (under pure electric fields) will be reported,<sup>40</sup> and the effects of pure stress fields and the combination of both stress and electric fields on the hysteresis behaviors will also be explored. Conclusions and future work will be provided in the last chapter, Chapter VI. In order to make this dissertation self-contained, discussions on calculating the intrinsic piezoelectric properties of ferroelectric single crystals around MPB by currently available LGD polynomials<sup>45-51</sup> are provided in the appendix.

### I.3. References

1. J. Valasek. *Phys. Rev.* **17**, 475 (1921).
2. G.H. Haertling, *J. Am. Ceram. Soc.* **82**, 797-818 (1999).
3. B. Jaffe, W. R. Cook, and H. Jaffe, *Piezoelectric Ceramics* (Academic, London, 1971).
4. J. Kuwata, K. Uchino, and S. Nomura, *Ferroelectrics* **37**, 579 (1981).
5. S.W. Choi, T.R. Shrout, S.J. Jang, and A.S. Bhalla, *Ferroelectrics* **100**, 29 (1989).
6. J. Kuwata, K. Uchino, and S. Nomura, *Jpn. J. Appl. Phys.* **21**, 1298 (1982).



7. T.R. Shrout, Z.P. Chang, N. Kim, and S. Markgraf, *Ferroelectrics Lett.* **12**, 63 (1990).
8. S.E. Park and T.R. Shrout, *J. Appl. Phys.* **82**, 1804 (1997).
9. W. Cochran, *Phys. Rev. Lett.*, **3**, 412 (1959); *Adv. Phys.* **9**, 387 (1960).
10. P.V. Anderson, in "*Physics of Dielectric*" G.I. Skanavi Ed., (Moscow: Izd. Akad. Nauk SSSR, 1960).
11. A.F. Devonshire, *Philos. Mag.* **40**, 1040 (1949); *Phil. Mag.* **42**, 1065 (1951); *Adv. Phys.* **3**, 85 (1954).
12. For complete references to the new intermediate MPB phases, see recent review: B. Noheda and D.E. Cox, *Phase Transitions* **79**, 5 (2006).
13. Y.U. Wang, *Phys. Rev. B* **74**, 104109 (2006); *Phys. Rev. B* **76**, 024108 (2007).
14. Y.M. Jin, Y.U. Wang, A.G. Khachatryan, J.F. Li, and D. Viehland, *Phys. Rev. Lett.* **91**, 197601 (2003); *J. Appl. Phys.* **94**, 3629 (2003).
15. Y.U. Wang, *Phys. Rev. B* **73**, 014113 (2006).
16. H. Wang, J. Zhu, N. Lu, A. A. Bokov, Z. G. Ye, and X. W. Zhang, *Appl. Phys. Lett.* **89**, 042908 (2006).
17. H. Wang, J. Zhu, X.W. Zhang, Y. X. Tang, and H. S. Luo, *J. Am. Ceram. Soc.* **91**, 2382 (2008).
18. L.A. Schmitt, K.A. Schönau, R. Theissmann, H. Fuess, H. Kungl, and M. J. Hoffmann, *J. Appl. Phys.* **101**, 074107 (2007).
19. R. Theissmann, L.A. Schmitt, J. Kling, R. Schierholz, K. A. Schönau, H. Fuess, M. Knapp, H. Kungl, and M. J. Hoffmann, *J. Appl. Phys.* **102**, 024111 (2007).
20. K.A. Schönau, L.A. Schmitt, M. Knapp, H. Fuess, R. A. Eichel, H. Kungl, and M. J. Hoffmann, *Phys. Rev. B* **75**, 184117 (2007).
21. K.A. Schönau, M. Knapp, H. Kungl, M. J. Hoffmann, and H. Fuess, *Phys. Rev. B* **76**, 144112 (2007).
22. G.A. Rossetti, Jr., W. Zhang, and A.G. Khachatryan, *Appl. Phys. Lett.* **88**, 072912 (2006).
23. V.A. Isupov, *Sov. Phys. Solid State* **10**, 989 (1968) [*Fiz. Tverd. Tela* **10**, 1244 (1968)]; *Phys. Solid State* **43**, 2262 (2001) [*Fiz. Tverd. Tela* **43**, 2171 (2001)]; *Ferroelectrics* **266**, 91 (2002).

24. L. Benguigui, Solid State Commun. **11**, 825 (1972); P. Ari-Gur and L. Benguigui, Solid State Commun. **15**, 1077 (1974).
25. K. Kakegawa, J. Mohri, T. Takahashi, H. Yamamura, and S. Shirasaki, Solid State Commun. **24**, 769 (1977); K. Kakegawa, J. Mohri, S. Shirasaki, and K. Takahashi, J. Am. Ceram. Soc. **65**, 515 (1982).
26. W. Cao and L.E. Cross, Phys. Rev. B **47**, 4825 (1993).
27. A.M. Glazer, P.A. Thomas, K.Z. Baba-Kishi, G.K.H. Pang, and C.W. Tai, Phys. Rev. B **70**, 184123 (2004).
28. M.V. Rane, A. Navrotsky, and G.A. Rossetti, Jr., J. Solid State Chem. **161**, 402 (2001).
29. G.A. Rossetti, Jr. and A.G. Khachaturyan, Appl. Phys. Lett. **91**, 072909 (2007).
30. L.Q. Chen, Annu. Rev. Matter. Res. **32**, 113 (2002)
31. S.C. Hwang, J.E. Huber, R.M. McMeeking and N.A. Fleck, J. Appl. Phys. **84**, 1530 (1998); S.C. Hwang, and R.M. McMeeking, Int. J. Solids Struct., **36**, 1541(1999).
32. J. Rodel and W.S. Kreher, J. Eur. Ceram. Soc. **23**, 2297 (2003).
33. S. Semenovskaya and A. G. Khachaturyan, J. Appl. Phys. **83**, 5125 (1998).
34. Y. L. Li, S. Y. Hu, Z. K. Liu, and L. Q. Chen, Appl. Phys. Lett. **78**, 3878 (2001).
35. J. W. Cahn and J. E. Hilliard, J. Chem. Phys. **28**, 258 (1958).
36. L. Q. Chen, J. Am. Ceram. Soc. **91**, 1835 (2008).
37. W.F. Rao and Y.U. Wang, Appl. Phys. Lett. **90**, 182906 (2007).
38. W.F. Rao and Y.U. Wang, Appl. Phys. Lett. **91**, 052901 (2007).
39. W.F. Rao and Y.U. Wang, Appl. Phys. Lett. **92**, 102905 (2008).
40. W.F. Rao and Y.U. Wang, “*Poling-Induced Single-Crystal-Like Piezoelectric Anisotropy in Ferroelectric Polycrystalline Ceramics*” (to be published).
41. Y.L. Li, S. Choudhury, Z.K. Liu, and L.Q. Chen, Appl. Phys. Lett. **83**, 1608 (2003); Y.L. Li and L.Q. Chen, Appl. Phys. Lett. **88**, 072905 (2006); S. Choudhury, Y. Li, and L.Q. Chen, J. Am. Ceram. Soc. **88**, 1669 (2005).
42. W.F. Rao and Y.U. Wang, Appl. Phys. Lett. **90**, 041915 (2007).
43. W.F. Rao, K.W. Xiao, and Y.U. Wang, “*Control of Domain Configurations and Sizes in Crystallographically Engineered Ferroelectric Single Crystals: Phase Field Modeling and Simulation*” (to be published).

44. W.F. Rao, T.L. Cheng, and Y.U. Wang, “ *Aging-Stabilization of Ferroelectric Domains through Short-Range Ordering of Charged Point Defects: Phase Field Modeling and Clausius-Clapeyron Analysis* ” (to be published).
45. A. Amin, M.J. Haun, B. Badger, H. McKinstry, and L.E. Cross, *Ferroelectrics* **65**, 107 (1985).
46. M.J. Haun, E. Furman, S.J. Jang, and L.E. Cross, *Ferroelectrics* **99**, 13 (1989).
47. M.J. Haun, E. Furman, H.A. McKinstry, and L.E. Cross, *Ferroelectrics* **99**, 27 (1989).
48. M.J. Haun, Z.Q. Zhuang, E. Furman, S.J. Jang, and L.E. Cross, *Ferroelectrics* **99**, 45 (1989).
49. M.J. Haun, E. Furman, T.R. Halemane, and L.E. Cross, *Ferroelectrics* **99**, 55 (1989).
50. M.J. Haun, E. Furman, S.J. Jang, and L.E. Cross, *Ferroelectrics* **99**, 63 (1989).
51. M.J. Haun, Z.Q. Zhuang, E. Furman, S.J. Jang, and L.E. Cross, *J. Am. Ceram. Soc.* **72**, 1140 (1989).

# Chapter II

## Phase Field Model for Ferroelectric Materials

### II.1. Formulation

MPB-based ferroelectric material is a compositionally, structurally, and electrically heterogeneous system composed of multiphase and multidomain microstructures, which is determined by the competitions among several energy contributions:

$$F^{total} = F^{bulk} + F^{grad} + F^{elec} + F^{elas}, \quad (1)$$

where  $F^{total}$  is a sum of all energy contributions over the volume space,  $F^{bulk}$  is the local chemical free energy that defines the thermodynamic properties of ferroelectric phases in stress-free homogeneous states,  $F^{grad}$  is the non-local short-range gradient energy (interfacial energy), characterizing the local polarization variations across the domain walls and grain boundaries,  $F^{elec}$  is the long-range electrostatic energy, arising from the dipole-dipole interactions and the externally applied electric field, and  $F^{elas}$  is the long-

range elastostatic energy induced by the coherency lattice misfit strain and externally applied mechanical loadings.

According to Landau-Ginzburg-Devonshire (LGD) theory,<sup>8</sup> the nonequilibrium bulk free energy density of ferroelectric single crystal in stress-free homogeneous states can be described in its own crystallographic coordinate system by a six-order polynomial, as,

$$\begin{aligned}
f^{bulk}(\vec{P}, c, T) = & \alpha_1(c, T)(P_1^{g2} + P_2^{g2} + P_3^{g2}) + \alpha_{11}(c)(P_1^{g4} + P_2^{g4} + P_3^{g4}) \\
& + \alpha_{12}(c)(P_1^{g2}P_2^{g2} + P_2^{g2}P_3^{g2} + P_3^{g2}P_1^{g2}) \\
& + \alpha_{111}(c)(P_1^{g6} + P_2^{g6} + P_3^{g6}), \quad (2) \\
& + \alpha_{112}(c)[P_1^{g4}(P_2^{g2} + P_3^{g2}) + P_2^{g4}(P_3^{g2} + P_1^{g2}) + P_3^{g4}(P_1^{g2} + P_2^{g2})] \\
& + \alpha_{123}(c)P_1^{g2}P_2^{g2}P_3^{g2}
\end{aligned}$$

where  $\alpha_i$ ,  $\alpha_{ij}$  and  $\alpha_{ijk}$  are the dielectric stiffness and higher order stiffness coefficients for a specific material system, determined by fitting the theoretical predictions to experimental data,  $T$  is temperature,  $c$  is the mole fraction of one component in a binary solid solution, and  $P_i^g$  is the  $i$ -th component of the polarization vector in the local crystallographic coordinate system aligned with  $\langle 100 \rangle$  lattice axes of the parent cubic phase in a given grain. It is worth noting that, the positive enthalpy of formation and entropy of mixing can be added to Eq. (2) to automatically reproduce the incoherent equilibrium (diffusional) phase diagram of ferroelectric solid solution,<sup>9</sup> and this free energy formulation can be adopted in computer simulation to account for coherent phase decomposition processes that are expected by the limited dislocation activities and nanoscale decomposition microstructure.<sup>3</sup>

Because of the distribution of crystallographic orientation of each grain, a reference (global) coordinate system is introduced to relate the disorientated grains in a polycrystal. The local polarization vector is thus transformed from the global system through

$$P_i^g = R_{ij}(\mathbf{r})P_j, \quad (3)$$

where summation convention over repeated indices is implied,  $P_j$  is the  $j$ -th component of the polarization vector in the global coordinate system, and  $R_{ij}(\mathbf{r})$  is a transformation (rotation) matrix field that describes the geometry (size, shape, and location) and crystallographic orientation of individual grains in the polycrystal, as in the phase field models of martensitic,<sup>10</sup> ferromagnetic,<sup>11</sup> and ferroelectric<sup>12</sup> polycrystals.

With the rotation matrix field, the spontaneous lattice misfit strain from the electrostriction effect,  $\epsilon_{ij}^0$ , can be expressed as,

$$\epsilon_{ij}^0 = R_{mi}R_{nj}R_{pk}R_{ql}Q_{mnpq}P_kP_l, \quad (4)$$

where  $Q_{ijkl}$  is the electrostriction coefficient tensor, which is generally a function of both composition and temperature.

If under stress-control condition, the overall elastostatic energy is a sum of following two equations,

$$F_{Ex}^{elas} = -\int \sigma_{ij}^{Ex} \epsilon_{ij}^0 d^3\mathbf{r}, \quad (5a)$$

$$F_{ij}^{Cohelas} = \frac{1}{2} \int C_{ijkl} (\epsilon_{ij} - \epsilon_{ij}^0)(\epsilon_{kl} - \epsilon_{kl}^0) d^3\mathbf{r}, \quad (5b)$$

where,  $\sigma_{ij}^{Ex}$  is the externally applied stress,  $C_{ijkl}$  is the elastic modulus constant tensor,  $\epsilon_{ij}$  is the local strain. Eq. (5a) accounts for the energy associated with the externally applied stress, and Eq. (5b) is for the energy induced by the coherency lattice misfit strain.

We follow ref. 13 to solve the elastic energy, Eq.(5b). For completeness, this derivation is described here. The total strain is written as a sum of the spatial heterogeneous and homogeneous strains,

$$\boldsymbol{\varepsilon}_{ij} = e_{ij} + \bar{\boldsymbol{\varepsilon}}_{ij}, \quad (6)$$

where, the heterogeneous strain satisfies  $\int e_{ij} d^3\mathbf{r} = 0$ , and the homogenous strain, defined as a spatial average of the total strain,  $\bar{\boldsymbol{\varepsilon}}_{ij} = \frac{1}{V} \int \boldsymbol{\varepsilon}_{ij} d^3\mathbf{r}$ , determines the macroscopic deformation of a polycrystal.

Substituting Eq.(6) into Eq.(5b), and rearranging yields the coherency elastic energy,

$$\begin{aligned} F^{Cohelest} &= \frac{1}{2} \int C_{ijkl} (\bar{\boldsymbol{\varepsilon}}_{ij} \bar{\boldsymbol{\varepsilon}}_{kl} - 2\bar{\boldsymbol{\varepsilon}}_{ij} \boldsymbol{\varepsilon}_{kl}^0 + \boldsymbol{\varepsilon}_{ij}^0 \boldsymbol{\varepsilon}_{kl}^0) d^3\mathbf{r} \\ &+ \frac{1}{2} \int C_{ijkl} (e_{ij} e_{kl} - 2e_{ij} \boldsymbol{\varepsilon}_{kl}^0) d^3\mathbf{r} + \int C_{ijkl} \bar{\boldsymbol{\varepsilon}}_{ij} e_{kl} d^3\mathbf{r}, \end{aligned} \quad (7)$$

Since the third integral goes to zero, Eq.(7) can be separated into two parts as,

$$F_{Homo}^{Cohelest} = \frac{1}{2} \int C_{ijkl} (\bar{\boldsymbol{\varepsilon}}_{ij} \bar{\boldsymbol{\varepsilon}}_{kl} - 2\bar{\boldsymbol{\varepsilon}}_{ij} \boldsymbol{\varepsilon}_{kl}^0 + \boldsymbol{\varepsilon}_{ij}^0 \boldsymbol{\varepsilon}_{kl}^0) d^3\mathbf{r}, \quad (8a)$$

$$F_{Heter}^{Cohelest} = \frac{1}{2} \int C_{ijkl} (e_{ij} e_{kl} - 2e_{ij} \boldsymbol{\varepsilon}_{kl}^0) d^3\mathbf{r}, \quad (8b)$$

where Eq. (8a) accounts for the homogeneous elastostatic energy and Eq. (8b) is for the heterogeneous elastostatic energy.

At elastic equilibrium, the total elastostatic energy should be minimized. Thus, for homogeneous part, we have,

$$\frac{\partial F_{Homo}^{Cohelest}}{\partial \bar{\boldsymbol{\varepsilon}}_{ij}} = \int C_{ijkl} (\bar{\boldsymbol{\varepsilon}}_{kl} - \boldsymbol{\varepsilon}_{kl}^0) d^3\mathbf{r} = 0, \quad (9)$$

and it yields,

$$\bar{\boldsymbol{\varepsilon}}_{ij} = \frac{1}{V} \int \boldsymbol{\varepsilon}_{ij}^0 d^3 \mathbf{r} = \bar{\boldsymbol{\varepsilon}}_{ij}^0, \quad (10)$$

To minimize Eq. (8b), instead of strain, we use the displacement as the independent variable, and introduce,

$$e_{ij} = \frac{1}{2} (v_{i,j} + v_{j,i}), \quad (11)$$

where  $v_i$  is the  $i$ -th component of displacement vector in the global coordinate system, and  $v_{i,j} = \partial v_i / x_j$ .

Assuming the stress field is applied uniformly and substituting Eq. (11) into Eq. (8b), the minimization of the heterogeneous elastostatic energy gives,

$$\frac{\delta F_{Heter}^{Cohelas}}{\delta v_i} = -C_{ijkl} (v_{k,lj} - \boldsymbol{\varepsilon}_{kl,j}^0) = 0, \quad (12)$$

which can be shown to be equivalent to the equilibrium equation of elasticity,  $\sigma_{ij,j} = 0$ , where  $\sigma_{ij}$  is stress tensor.

In order to solve Eq. (12), Fourier transform technique is applied and the displacement field is solved in the reciprocal space,

$$\tilde{v}_i(\mathbf{k}) = -i G_{ij}(\mathbf{k}) C_{jklm} k_k \tilde{\boldsymbol{\varepsilon}}_{lm}^0(\mathbf{k}), \quad (13)$$

where  $\mathbf{k}$  is a directional vector in the reciprocal space, the tilde sign  $\sim$  indicates the Fourier transform of the corresponding function, for example,  $\tilde{v}_k(\mathbf{k}) = \int v_k(\mathbf{r}) e^{-i\mathbf{k}\cdot\mathbf{r}} d^3 \mathbf{r}$ , and  $\tilde{\boldsymbol{\varepsilon}}_{kl}^0(\mathbf{k}) = \int \boldsymbol{\varepsilon}_{kl}^0(\mathbf{r}) e^{-i\mathbf{k}\cdot\mathbf{r}} d^3 \mathbf{r}$ , and  $G_{ik}(\mathbf{k}) = (C_{ijkl} k_j k_l)^{-1}$  is the Green function tensor of elasticity.

The strain can thus be calculated by inverse Fourier transform,



$$v_{i,j} = \int \frac{d^3\mathbf{k}}{(2\pi)^3} G_{ik} C_{klmn} k_j k_l \tilde{\epsilon}_{mn}^0 e^{i\mathbf{k}\cdot\mathbf{r}}, \quad (14)$$

Hence, using Eq.(14), the heterogeneous contribution can be expressed as,

$$F_{Heter}^{Cohelas} = -\frac{1}{2} \int \frac{d^3\mathbf{k}}{(2\pi)^3} C_{ijmn} n_m \Omega_{np} n_q C_{klpq} \tilde{\epsilon}_{ij}^0 \tilde{\epsilon}_{kl}^{0*}, \quad (15)$$

where superscript asterisk \* indicates the complex conjugate,

$\Omega_{ij}(\mathbf{n}) = \mathbf{k}^2 G_{ij}(\mathbf{k}) = (C_{ikjl} n_k n_l)^{-1}$ , and  $\mathbf{n} = \mathbf{k}/k$  is a unit directional vector in the reciprocal space.

Also, using Eq.(10), the homogeneous elastostatic energy can be calculated in the reciprocal space as,

$$F_{Homo}^{Cohelas} = \frac{1}{2} \int \frac{d^3\mathbf{k}}{(2\pi)^3} C_{ijkl} \tilde{\epsilon}_{ij}^0 \tilde{\epsilon}_{kl}^{0*} - \frac{1}{2} \int C_{ijkl} \bar{\epsilon}_{ij}^0 \bar{\epsilon}_{kl}^0 d^3\mathbf{r}, \quad (16)$$

The electric state of a ferroelectric polycrystal is described by the distribution of polarization field,  $\mathbf{P}(\mathbf{r})$ , and the divergence of polarization field gives the density of volume charge at each spatial position. Considering the Coulomb's law, the total dipole-dipole interaction electrostatic energy is given by a double integral of the potential energy of interacting local charges at positions  $\mathbf{r}$  and  $\mathbf{r}'$ ,

$$F_{inter}^{elec} = \frac{1}{2} \frac{1}{4\pi\epsilon_0} \iint \left( \frac{\nabla \cdot \mathbf{P}(\mathbf{r}) \cdot \nabla' \cdot \mathbf{P}(\mathbf{r}')}{|\mathbf{r} - \mathbf{r}'|} \right) d^3\mathbf{r} d^3\mathbf{r}', \quad (17)$$

where  $\epsilon_0$  is the permittivity constant of vacuum. Using the Fourier transform technique, this integration can be efficiently calculated in the reciprocal space,

$$F_{inter}^{elec} = \frac{1}{2} \int \frac{d^3k}{(2\pi)^3} \frac{n_i n_j}{\epsilon_0} \tilde{P}_i(\mathbf{k}) \tilde{P}_j^*(\mathbf{k}), \quad (18)$$

If an electric field is applied, the polarization is likely to be rotated or poled into the same direction of the applied field. The interaction of local polarization with the externally applied electric field can be described by

$$F_{Ex}^{elec} = -\int \mathbf{E}_{Ex} \cdot \mathbf{P}(\mathbf{r}) d^3\mathbf{r}, \quad (19)$$

where  $\mathbf{E}_{Ex}$  is the externally applied electric field. Thus, the sum of Eq.(18) and Eq. (19) gives the total electrostatic energy of a ferroelectric polycrystal.

The inhomogeneity of polarization distribution, for example, due to polarization crossing the domain walls and grain boundaries, gives rise to an extra contribution to the total free energy. When the diffusion process is considered, the inhomogeneous composition distribution also causes the total energy increasing. These terms are usually called the gradient energies, and are described by the gradient of polarization field and composition field as,

$$F_{polar}^{grad} = \int \frac{1}{2} \beta_{ijkl}^p \frac{\partial P_i(\mathbf{r})}{\partial r_j} \frac{\partial P_k(\mathbf{r})}{\partial r_l} d^3\mathbf{r}, \quad (20a)$$

$$F_{comp}^{grad} = \int \frac{1}{2} \beta_{ij}^c \frac{\partial c(\mathbf{r})}{\partial r_i} \frac{\partial c(\mathbf{r})}{\partial r_j} d^3\mathbf{r}, \quad (20b)$$

where the tensors  $\beta_{ijkl}^p$  and  $\beta_{ij}^c$  are the positive gradient coefficients of polarization field and composition field, respectively.

Hitherto, all energy contributions have been explicitly expressed as functionals of composition field and global polarization field. Adding up the integral of Eq. (2) over the volume space, Eq. (5a), (15), (16) and (18-20) gives the total energy.

The temporal evolution of the microstructures is completely characterized by the evolution of the composition and polarization fields, which are driven by a reduction of

the total system free energy through diffusion and structural relaxation. The phase decomposition process and the evolution of polarization and domain microstructures are governed by two phenomenological equations, namely, the time-dependent Ginzburg-Landau<sup>14,15</sup> equations for nonconserved polarization fields and the Cahn-Hilliard<sup>16</sup> nonlinear diffusion equation for conserved composition field, respectively,

$$\frac{\partial P_i(\mathbf{r}, t)}{\partial t} = -L_{ij} \frac{\delta F^{total}}{\delta P_j(\mathbf{r}, t)} + \xi_i^P(\mathbf{r}, t), \quad (21a)$$

$$\frac{\partial c(\mathbf{r}, t)}{\partial t} = \nabla \cdot D \nabla \frac{\delta F^{total}}{\delta c(\mathbf{r}, t)} + \xi^c(\mathbf{r}, t), \quad (21b)$$

where  $t$  is time,  $L_{ij}$  is the kinetic coefficient of polarization relaxation,  $D$  is the chemical mobility of diffusion,  $\nabla$  is the gradient operator,  $\xi_i^P(\mathbf{r}, t)$  and  $\xi^c(\mathbf{r}, t)$  are Gaussian-distributed Langevin noise terms to account for the effect of thermal fluctuation.

## II.2. Numerical simulations

The above formulation is generally applicable to three-dimensional ferroelectric polycrystals. However, due to the limitations of the computation capability, two-dimensional simulations will be performed to study polarization rotations and domain microstructure formations and evolutions.

For calculating the total energy, Eq.(2), the sample is assumed to be elastically homogeneous and isotropic, thus,

$$C_{ijkl} = 2\mu\nu\delta_{ij}\delta_{kl} / (1 - 2\nu) + \mu(\delta_{ik}\delta_{jl} + \delta_{il}\delta_{jk}), \quad (22)$$

where  $\delta_{ij}$  is Kronecker delta,  $\mu$  and  $\nu$  are shear modulus and Poisson's ratio. Therefore, we have,

$$G_{ij} = \delta_{ij} / \nu k^2 - k_i k_j / 2\mu(1-\nu)k^4, \quad (23a)$$

$$\Omega_{ij} = \delta_{ij} / \mu - n_i n_j / 2\mu(1-\nu), \quad (23b)$$

The gradient and kinetic coefficients are assumed to be orientation independent, as,

$$\beta_{ijkl}^p = \beta^p \delta_{ik} \delta_{jl}, \quad (24a)$$

$$\beta_{ij}^c = \beta^c \delta_{ij}, \quad (24b)$$

$$L_{ij} = L \delta_{ij}. \quad (24c)$$

The periodic boundary conditions are assumed in the phase field model. It is worthy to note that, while some functionals of energetic contributions, for example, the bulk chemical and gradient energies, can be described either in real space or in reciprocal space, it is a real challenge to explicitly solve the heterogeneous parts of elastostatic and electrostatic energies in real space. Thus, Fast Fourier Transform (FFT) techniques are employed to calculate all energy terms in reciprocal space. As a consequence, the periodic boundary condition is implemented in simulations.

To better understand the simulation results, it is necessary to discuss the currently available LGD polynomials and the intrinsic electrostrictive and piezoelectric properties of ferroelectrics, which is provided in the appendix of this dissertation.

## II.3. References

1. W.F. Rao and Y.U. Wang, Appl. Phys. Lett. **90**, 041915 (2007).
2. W.F. Rao and Y.U. Wang, Appl. Phys. Lett. **90**, 182906 (2007).
3. W.F. Rao and Y.U. Wang, Appl. Phys. Lett. **91**, 052901 (2007).
4. W.F. Rao and Y.U. Wang, Appl. Phys. Lett. **92**, 102905 (2008).
5. W.F. Rao and Y.U. Wang, “*Poling-Induced Single-Crystal-Like Piezoelectric*

- Anisotropy in Ferroelectric Polycrystalline Ceramics*” (to be published).
6. W.F. Rao, K.W. Xiao, and Y.U. Wang, “*Control of Domain Configurations and Sizes in Crystallographically Engineered Ferroelectric Single Crystals: Phase Field Modeling and Simulation*” (to be published).
  7. W.F. Rao, T.L. Cheng, and Y.U. Wang, “*Aging-Stabilization of Ferroelectric Domains through Short-Range Ordering of Charged Point Defects: Phase Field Modeling and Clausius-Clapeyron Analysis*” (to be published).
  8. A.F. Devonshire, *Philos. Mag.* **40**, 1040 (1949).
  9. G.A. Rossetti, Jr., W. Zhang, and A.G. Khachaturyan, *Appl. Phys. Lett.* **88**, 072912 (2006).
  10. Y.M. Jin, A. Artemev, and A.G. Khachaturyan, *Acta Mater.* **49**, 2309 (2001); Y.U. Wang, Y.M. Jin, and A.G. Khachaturyan, *Acta Mater.* **52**, 1039 (2004).
  11. Y.M. Jin, Y.U. Wang, A. Kazaryan, Y. Wang, D.E. Laughlin, and A.G. Khachaturyan, *J. Appl. Phys.* **92**, 6172 (2002).
  12. S. Choudhury, Y.L. Li, C.E. Krill III, and L.Q. Chen, *Acta Mater.* **53**, 5313 (2005); S. Choudhury, Y.L. Li, C.E. Krill III, and L.Q. Chen, *Acta Mater.* **55**, 1415 (2007).
  13. Y.M. Jin, Ph.D. dissertation, “*Theory, Modeling, and Simulation of Structural and Functional Materials: Micromechanics, Microstructures, and Properties,*” Rutgers, The State University of New Jersey, New Brunswick, New Jersey, 2003.
  14. S. Semenovskaya and A. G. Khachaturyan, *J. Appl. Phys.* **83**, 5125 (1998).
  15. Y. L. Li, S. Y. Hu, Z. K. Liu, and L. Q. Chen, *Appl. Phys. Lett.* **78**, 3878 (2001).
  16. J. W. Cahn and J. E. Hilliard, *J. Chem. Phys.* **28**, 258 (1958).

# Chapter III

## Phase-Coexisting Domain Microstructure

### III.1. Introduction

Phase coexistence is commonly observed around the morphotropic phase boundaries (MPBs) of ferroelectric solid solutions. In the temperature-composition phase diagrams of lead-based perovskite-type systems, such as PZT,<sup>4</sup> PZN-PT,<sup>5</sup> and PMN-PT,<sup>6</sup> the MPB is a nearly vertical phase boundary separating two ferroelectric phases, namely, rhombohedral and tetragonal phases at low and high Ti contents, respectively. The presence of MPB as a sharp-line phase boundary has raised great scientific curiosity, because it violates Gibbs phase rule for thermodynamically equilibrium temperature-composition phase diagram,<sup>7</sup> and the mechanism of phase transition between ferroelectric rhombohedral and tetragonal phases across MPB is an interesting question.<sup>8</sup> It has been long-recognized that a two-phase zone is required around MPB, and the MPB is considered as located at the composition where the two phases coexist in equal quantity.<sup>4</sup>

Because the best piezoelectric properties of these materials are obtained at compositions in the vicinity of their MPBs,<sup>4,9-11</sup> the effect of MPB phase coexistence on the piezoelectric properties is a question of both scientific and technological importance.

Recently, new intermediate MPB phases were observed by high-resolution X-ray and neutron diffractions,<sup>12</sup> which renews the interest in the phase diagrams of these ferroelectric solid solutions. Some investigators thus associate the origin with the presence of new intermediate MPB phases.<sup>12</sup> However, there are new findings that questioned those lower-symmetry phases, from both theoretical<sup>13-15</sup> and experimental<sup>16-21</sup> aspects. Those investigations reveal nanodomain aspects of the MPB structures and coherent scattering and interference effects in nanodomain diffractions, underscoring the importance of domain microstructures and mechanisms in the vicinity of MPBs.

As the current material of choice for a wide variety of high-performance electromechanical devices, PZT has been best studied over decades. In order to explain the origin of the exceptional properties found around MPB, insights have been gained from different perspectives, e.g., stability and metastability of coexisting phases,<sup>22</sup> solubility gap,<sup>23</sup> compositional fluctuation,<sup>24</sup> statistical distribution of accessible polar states,<sup>25</sup> progression of local structural order,<sup>8</sup> equilibrium phase diagram satisfying Gibbs phase rule,<sup>7</sup> and inherent nanoscale structural instability associated with vanishing electrocrystalline anisotropy near MPB.<sup>26</sup> These studies have significantly improved our understandings on the nature of MPB-based ferroelectrics. However, none of them considers the formation of ferroelectric and ferroelastic domain microstructures and its role in phase coexistence. These investigations are based on local free energy analyses within conventional Gibbsian thermodynamics, and do not consider the dependence of

total system free energy on domain microstructures through long-range electrostatic and elastostatic interactions.

It is known that spontaneous domain formation is an essential feature of ferroelectrics, where the spontaneous polarization self-arranges into head-to-tail patterns to minimize the long-range electrostatic interaction energy, and the accompanying ferroelastic lattice distortion is self-accommodated through formation of structural twins to minimize the long-range elastostatic interaction energy. While twin formation is a well-known lattice misfit-accommodating mechanism among multiple structural orientation variants of single phase (rhombohedral or tetragonal), the strain-accommodating mechanism for the crystal lattice misfit between different phases is less well understood. As a matter of fact, adjoining rhombohedral and tetragonal domains across a coherent interface does not accommodate the lattice misfit between them, thus a stress-free state cannot be achieved. Moreover, the polarization distribution in the inter-phase interface region also needs to be better investigated. Clearly, the electrostatic and elastostatic interactions have significant effects on the formation of coupled ferroelectric and ferroelastic domain microstructures and on the phase coexistence around MPBs.

In this chapter we employ computer modeling and simulation to quantitatively study the interplays among various energetic contributions, including electrostatic energy of polarization distribution, elastostatic energy of lattice misfit, gradient energy of polarization change across domain walls, and bulk energy gap between metastable and stable phases. In particular, we investigate the domain microstructures and mechanisms for phase coexistence and piezoelectricity enhancement around MPBs.



## III.2. Coherent Phase Decomposition

In this section, coherent microstructures of phase decomposition near morphotropic phase boundary in lead zirconate titanate are investigated by using computer modeling and simulation. The model is based on the recently proposed incoherent equilibrium phase diagram [G.A. Rossetti, Jr. et al., Appl. Phys. Lett. **88**, 072912 (2006)] and takes into account the coherency strain energy and electrostatic energy. It reveals characteristic multi-domain microstructures, where nanoscale lamellar domains of tetragonal and rhombohedral phases coexist with well-defined crystallographic orientation relationships. The phase-coexisting nanodomain microstructures play a significant role in interpretation of X-ray and neutron diffraction data and identification of phases near morphotropic phase boundary.

Recently, an extended thermodynamic theory of PZT solid solution was formulated,<sup>7</sup> which treats PZT system as a regular solution and combines the conventional LGD free energy function<sup>27</sup> with positive enthalpy of formation<sup>28</sup> and entropy of mixing, as,

$$\begin{aligned}
 f(x, \mathbf{P}) = & \frac{a_2(x)}{2} [T - T_C(x)] (P_1^2 + P_2^2 + P_3^2) + \frac{a_4}{4} (x - x_m) (P_1^2 + P_2^2 + P_3^2)^2 \\
 & + \frac{a'_4}{4} (x - x_m) (P_1^4 + P_2^4 + P_3^4) + \frac{a_6}{6} (P_1^2 + P_2^2 + P_3^2)^3, \quad (25) \\
 & + \frac{w}{2} x(1-x) + \frac{k_B T}{\Omega} [x \ln x + (1-x) \ln (1-x)]
 \end{aligned}$$

where  $T$  is temperature,  $T_C$  is Curie-Weiss temperature of PZT,  $x$  is the mole fraction of PT in PZT,  $x_m$  is the MPB composition,  $w$  is the atomic exchange interaction parameter characterizing enthalpy of mixing,  $k_B$  is Boltzmann's constant,  $\Omega$  is the unit cell volume

of  $\text{PbTiO}_3$ , and  $a$ 's are the polynomial coefficients of LGD expansion of the polarization-dependent part of the bulk free energy.

The new free energy formulation automatically predicts equilibrium (diffusional) PZT phase diagram with two-phase region replacing the linear MPB and satisfying the Gibbs phase rule.<sup>7</sup> As shown in Fig. 3-1, the phase diagram predicts phase decomposition through peritectoid reaction, where diffusion rate is estimated to be sufficiently fast during normal material processing.<sup>7</sup>

It is worth noting, while providing valuable insight into the phase coexistence phenomenon, the predicted phase diagram is for *incoherent phases*, i.e., coherency strain energy is not considered. In real PZT samples, *coherent phases* are expected because of the limited dislocation activities and nanoscale decomposition microstructures.

The purpose of this section is to report characteristic two-phase multidomain microstructures that are formed by phase decomposition near MPB, gain insight into nanodomain effects on diffraction, and better understand the phase behavior and phase diagram of PZT. In this section, We adopt the recently proposed free energy formulation,<sup>7</sup> Eq. (25), and employ computer modeling and simulation to study the effects of coherency strain energy (and electrostatic energy and polarization gradient energy as well) on domain microstructure evolution during phase decomposition near the MPB in PZT. A value of  $w=0.5k_B T_C/\Omega$  is used in the computer simulation for the positive enthalpy of mixing.<sup>7,28</sup> The simulation is performed with 512x512 computational cell with grid size of ~2 nm.

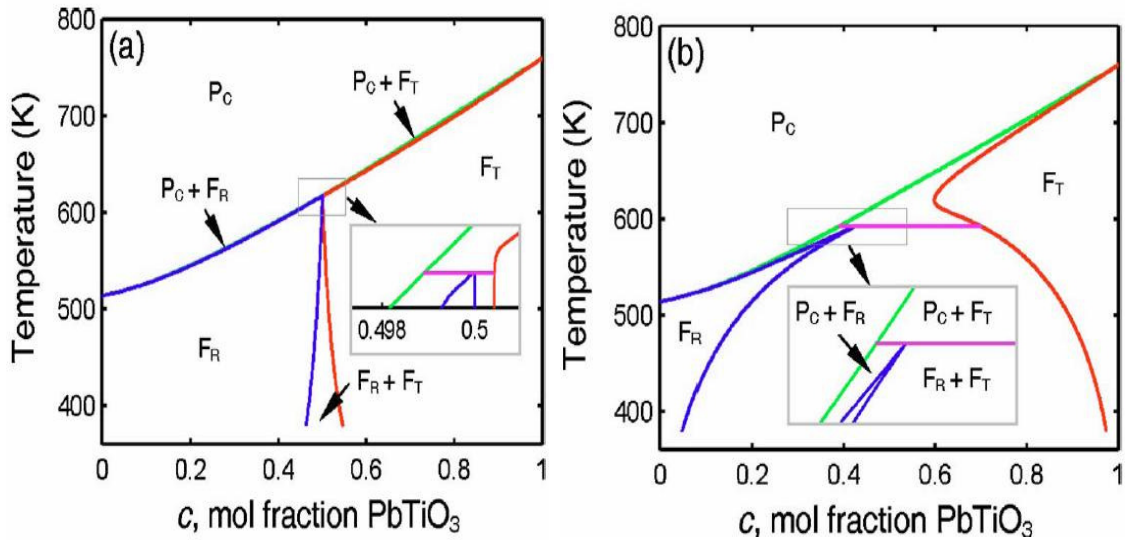


FIG. 3-1. (After ref. 7). Computed equilibrium phase diagrams for PZT solid solutions exhibiting ideal behavior with atomic exchange mixing parameter  $w=0$  (a); exhibiting nonideal behavior with  $w=2.75$  (b). Both are peritectoid diagrams with invariant lines located at 617 K in (a) and 592 K in (b).

Our simulation reveals characteristic multi-domain microstructures, where lamellar domains of tetragonal and rhombohedral phases coherently coexist with well-defined crystallographic orientation relationships, as shown in Fig. 3-2. We consider PZT system at room temperature with nominal MPB composition,  $x=x_m=0.5$  defined in Eq. (25). Fig. 3-2(a)-(e) show the simulated two-phase microstructures from the early-stage to coarsened decomposition, respectively, where tetragonal (red) and rhombohedral (blue) phases are visualized according to their compositions. These representative stages of coherent phase decomposition exhibit essentially the same morphological characteristics, despite that the composition has not reached equilibrium values in Fig. 3-2(a) and the microstructural sizes grow with increasing simulation time in Fig. 3-2(e).

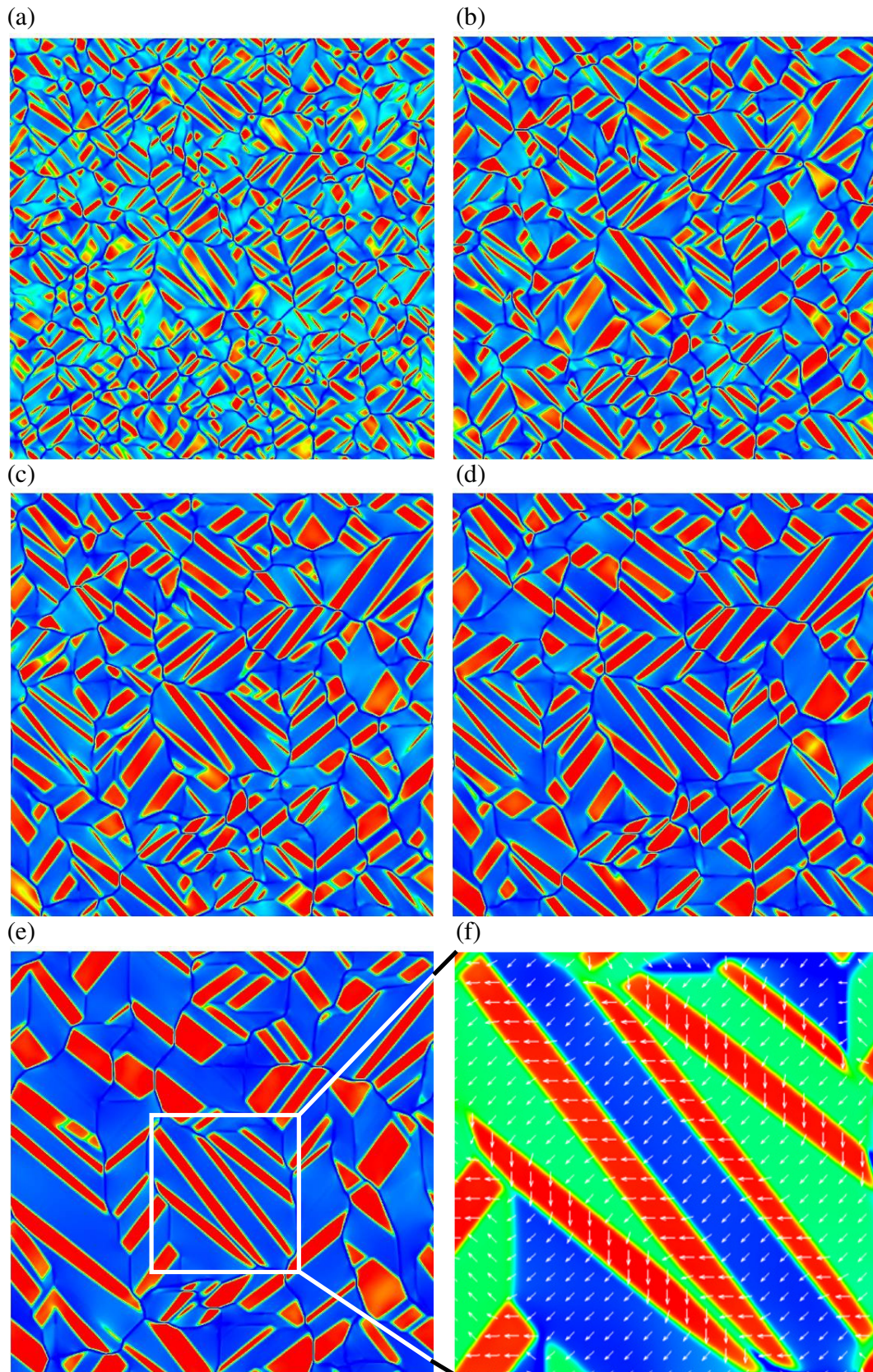


FIG. 3-2. (After ref. 1). Computer simulation of coherent microstructures of phase decomposition in PZT near MPB at room temperature. (a)-(e) Two-phase morphology at different stages of decomposition (from early to coarsened stages, corresponding to simulation time  $t=1, 3, 5, 10, 30$ , respectively), where color scale shows the composition profile: tetragonal phase in red ( $x\approx 0.77$ ) and rhombohedral phase in blue ( $x\approx 0.38$ ). (f) Close-up visualization of a portion of the phase-coexisting multi-domain microstructure shown in (e), where arrows represent the in-plane components ( $P_x, P_y$ ) of polarization vector and the out-of-plane component ( $P_z$ ) is represented by color: red domains ( $P_z=0$ ) are tetragonal phase, green ( $P_z>0$ ) and blue ( $P_z<0$ ) domains are rhombohedral phase.

This coarsening phenomenon is driven by a reduction in the interfacial energy, as observed in conventional decomposition phase transformations. Nevertheless, compared with conventional phase decompositions, the ferroelectric phase decomposition shows some peculiar microstructural features from its very early stage, which result from the coherency strain and, in particular, the electrostatics of polarization. As shown in Fig. 3-2, the interfaces of lamellar compositional domains of tetragonal (red) phase (i.e., the habit planes of the lamellas) exhibit well-defined orientations, which are close to  $\{340\}$  in two-dimensional simulation. Analysis shows that such habit planes minimize the interfacial charge density by satisfying  $(\mathbf{P}^R - \mathbf{P}^T) \cdot \mathbf{n} \approx 0$ , where  $\mathbf{n}$  is the interface normal vector, and  $\mathbf{P}^R$  and  $\mathbf{P}^T$  are the polarization vectors of the decomposed rhombohedral and tetragonal phases, respectively.

Fig. 3-2(f) shows a close-up view of the phase-coexisting multi-domain microstructure, which is visualized according to the components of the polarization. The  $\{340\}$  interfaces are  $55^\circ$  domain walls between rhombohedral and tetragonal phases. The domains of tetragonal (red) phase mutually form twins of  $\{110\}$  twin boundaries, which are  $90^\circ$  ferroelectric domain walls; the domains of rhombohedral (green and blue) phase

form twins of either {100} or {110} twin boundaries, which are 109° and 71° domain walls, respectively. These twins are in agreement with the crystallographic analysis of domain microstructures.

It is worth noting another peculiar behavior of the ferroelectric phase decomposition as revealed by the computer simulation. The ferroelectric domain walls possess a lower Ti content, i.e., composition  $x$  is a little lower along domain walls than inside domains. Such domain wall depletion zones are visible as deep blue narrow regions running along tetragonal-rhombohedral interfaces and inside rhombohedral (blue) phase in Fig. 3-2(b)–(e). The domain wall Ti depletion results from the modification of diffusional decomposition by elastostatic and electrostatic interactions between different ferroelastic-ferroelectric domains, in particular, the local stress and electric fields in domain wall regions.

The computer simulation shows that coherent phase decomposition in PZT produces nanoscale multi-domain microstructures. Experimental investigation<sup>24</sup> and theoretical estimation<sup>7</sup> show that the diffusion rate in PZT produces composition heterogeneities with a typical wavelength of the order of 10 nm. This domain size is significantly below the coherence length of diffraction radiations used to characterize PZT phases. Therefore, the phase-coexisting nanodomain microstructures play a significant role in interpretation of X-ray and neutron diffraction data and identification of phases near MPB. Nanotwin diffraction analysis has shown that, with domain sizes reduced to nanoscale, adaptive Bragg reflection peaks appear between the conventional twin peaks of coarse domains, the positions of the new peaks are determined by the relative thicknesses of nanotwin variants, and the peak intensities depend on the nanodomain size and volume fraction.<sup>13</sup>

These adaptive Bragg peaks correspond to monoclinic phases, whose lattice parameters are intrinsically related to that of the conventional phases forming the nanotwins.<sup>14-15</sup> Such extraordinary diffraction peaks cannot be explained by conventional diffraction theory of coarse domains, and an introduction of monoclinic phase is found to improve the Rietveld refinement of diffraction data, which leads to the report of new monoclinic phase.<sup>12</sup> It is noteworthy that such an adaptive diffraction phenomenon from nanodomain microstructures has been directly observed in PZT near MPB by complementary X-ray powder diffraction and transmission electron microscopy experiments,<sup>20</sup> where the appearance of a new peak between conventional twin peaks is correlated to the formation of nanodomains and Rietveld refinement leads to monoclinic phase. Clearly, without taking into account the nanoscale domain microstructures, the diffraction data could be easily misinterpreted and assigned to wrong phase such as monoclinic.

It is worth noting that the monoclinic lattice corresponds to the average symmetry of the nanotwins and exhibits intrinsic lattice parameter relationships,<sup>14,15</sup> as predicted by both diffraction analysis<sup>13</sup> and crystallographic analysis through nanodomain averaging.<sup>14,15</sup> Following nanodomain averaging, the phase-coexisting multi-domain microstructure shown in Fig. 3-2 exhibits, in general, an averaged crystal structure of pseudo-orthorhombic symmetry with small triclinic shear distortions. In particular, when lamellar domains of one tetragonal orientation variant is dominant in a local volume of coherent diffraction, the average lattice has a pseudo-tetragonal symmetry with lattice parameters  $c = \omega c_t + (1 - \omega) a_r$  and  $a = \omega a_t + (1 - \omega) a_r$ , where  $c_t$ ,  $a_t$  and  $a_r$  are the lattice parameters of tetragonal and rhombohedral phases, respectively, and  $\omega$  is the volume fraction of tetragonal phase. One important implication of these relations is that the

measured lattice parameters  $c$  and  $a$ , as assigned to tetragonal phase, are strongly dependent on the volume fraction  $\omega$  of tetragonal phase.

With the nominal composition  $x$  of PZT samples decreasing from tetragonal to rhombohedral phase fields across the MPB,  $\omega$  rapidly drops from 1 to 0 over a narrow composition range, whose width depends on both the positive enthalpy of mixing and diffusion rate. Accompanying  $\omega$  change, the measured tetragonal lattice parameters  $c$  and  $a$  rapidly converge towards  $a_r$  with tetragonality ratio  $c/a$  rapidly decreasing to 1. Such predictions are, in fact, consistent with the Rietveld refinement-measured PZT lattice parameters, where  $c$  and  $a$  change smoothly with composition before rapidly converging towards  $a_r$  within a narrow composition range of MPB phase-coexistence.<sup>29</sup> It, thus, raises the question whether such a rapid lattice parameter variation near MPB is an intrinsic behavior or instead a result of coherence diffraction effect due to the phase-coexisting nanodomain microstructure. Answers to this question will help better understand the nature of MPB, phase coexistence, PZT phase diagram, and enhanced piezoelectricity near MPB.



### III.3. Bridging Domain Mechanism

In this section, a bridging domain mechanism is revealed to explain the phase coexistence commonly observed around the morphotropic phase boundaries of ferroelectric solid solutions. The simulation takes into account the important role of coupled ferroelectric and ferroelastic domain microstructures in phase coexistence phenomenon. It shows that minor domains of metastable phase spontaneously coexist with and bridge major domains of stable phase to reduce total system free energy, including bulk free energy, domain wall energy, long-range electrostatic and elastostatic energies. It also shows that the existence of bridging domains enhances the piezoelectric response in the vicinity of morphotropic phase boundaries.

Spontaneous domain formation is an essential feature of ferroelectrics, where the spontaneous polarization self-arranges into head-to-tail patterns to minimize the long-range electrostatic interaction energy, and the accompanying ferroelastic lattice distortion is self-accommodated through formation of structural twins to minimize the long-range elastostatic interaction energy. In particular, phase-coexisting ferroelectrics around MPBs are spatially more heterogeneous systems with multi-phase and multi-domain microstructures. The heterogeneity can originate from two physically distinct processes, i.e., diffusional and diffusionless. Diffusional process leads to compositional fluctuation<sup>24</sup> or decomposition into two-phase equilibrium.<sup>7</sup> In computer simulations,  $\mathbf{P}(\mathbf{r},t)$  and  $c(\mathbf{r},t)$  are simultaneously evolved with different speeds, characterized by the kinetic coefficient  $L_{ij}$  in Eq. (21a) and diffusivity  $D$  in Eq. (21b), respectively. Depending on the

different combinations of  $L$  and  $D$ , the kinetic pathway of evolution can be quite different, as schematically shown in Fig. 3-3.

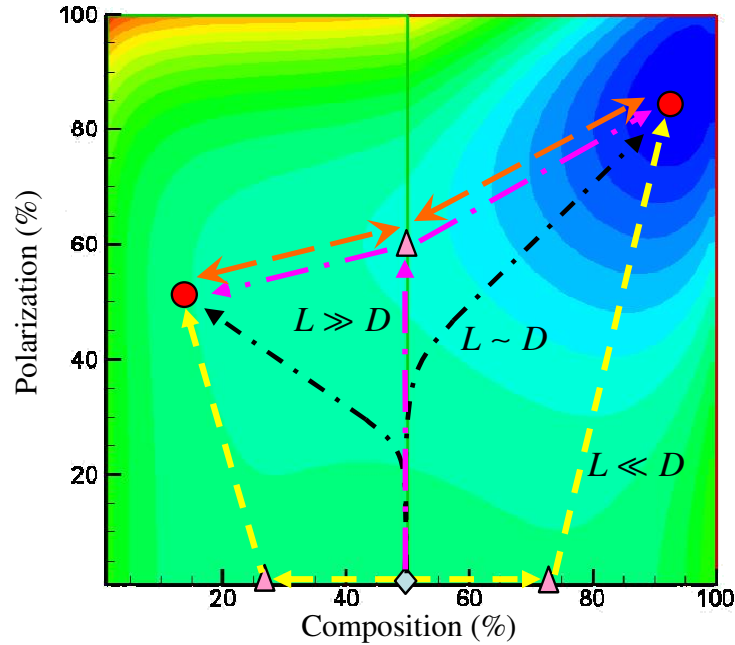


FIG. 3-3. Kinetic pathways of phase decomposition in PZT. The color on this map shows contour of free energies of two coexisting phases, e.g., tetragonal phase on the right and rhombohedral phase on the left, the location of MPB is indicated by the green line, two red dots represent the equilibrium states of two coexisting phases. Three different paths are schematically drawn out by yellow, black, and purple vectors, for the cases of  $L \ll D$ ,  $L \sim D$ , and  $L \gg D$ , respectively; the transition path between two equilibrium phases is shown by orange double vectors.

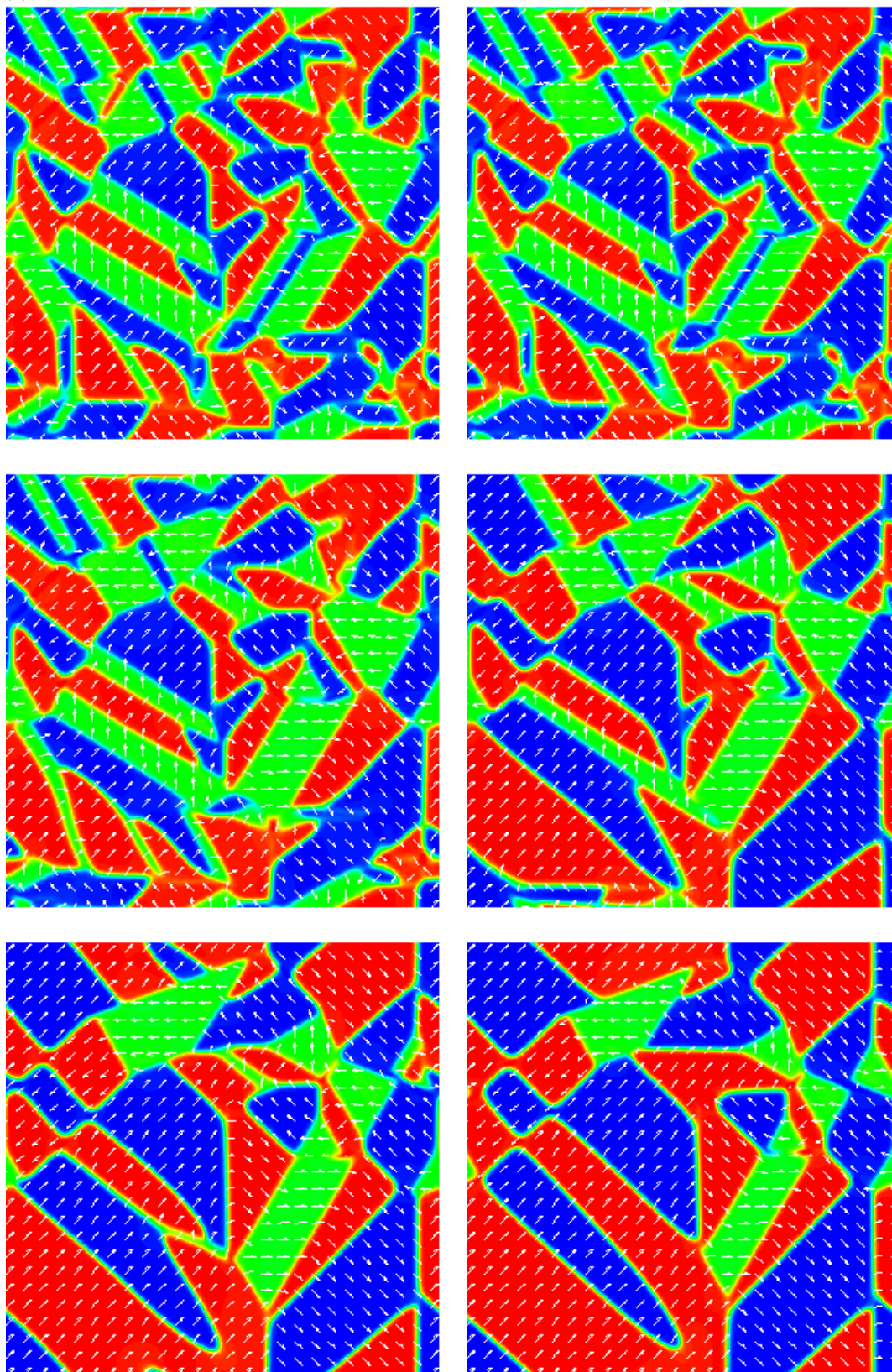
Since the kinetic pathway profoundly affects microstructures and the microstructures determine the material properties, it is desirable to experimentally control the  $L$ - $D$  ratio and investigate the microstructure evolution under achievable conditions. However, quantitative observation is not available at present. Since diffusion kinetics in the complex oxide solid solutions is slow at room temperature, diffusional process is expected to play an important role only at elevated temperature or over long time period.

In the following work, we focus on the diffusionless mechanism, i.e., the displacive evolution of spontaneous polarization leading to the formation of domain microstructure without local composition change.

In this section, the experimentally determined LGD polynomial coefficients,<sup>30</sup> ultrasonically-measured elastic constants,<sup>31</sup> and Rietveld refinement-derived electrostriction coefficients<sup>29</sup> for PZT system at room temperature within MPB composition range are employed. It shows that, even without compositional heterogeneity, stable and metastable phases spontaneously coexist around MPB to reduce the domain microstructure-dependent total system free energy.

The computer simulation reveals a bridging domain mechanism for formation of mosaic domain microstructures that explains the phase coexistence phenomenon and enhanced piezoelectricity around MPBs, as shown in Fig. 3-4. We consider PZT system at room temperature with near MPB compositions. Fig. 3-4(a) shows the simulated domain microstructure in PZT of composition  $x=0.49$ . The in-plane components of polarization vector are represented by arrows, and the out-of-plane component is represented by color. The simulation shows that minor domains of tetragonal phase (green) spontaneously coexist with and bridge major domains of rhombohedral phase (red and blue), and together form mosaic domain microstructure. Fig. 3-4(b) shows the simulated domain microstructure in PZT of composition  $x=0.50$ . In contrast to the case of  $x=0.49$ , the rhombohedral phase (red and blue) forms minor domains that coexist with and bridge the major domains of tetragonal phase (green). Such phase-coexisting mosaic domain microstructures effectively reduce the total system free energy, including bulk free energy, domain wall energy, and long-range electrostatic and elastostatic energies.

(a)  $x=0.49$



(b)  $x=0.50$

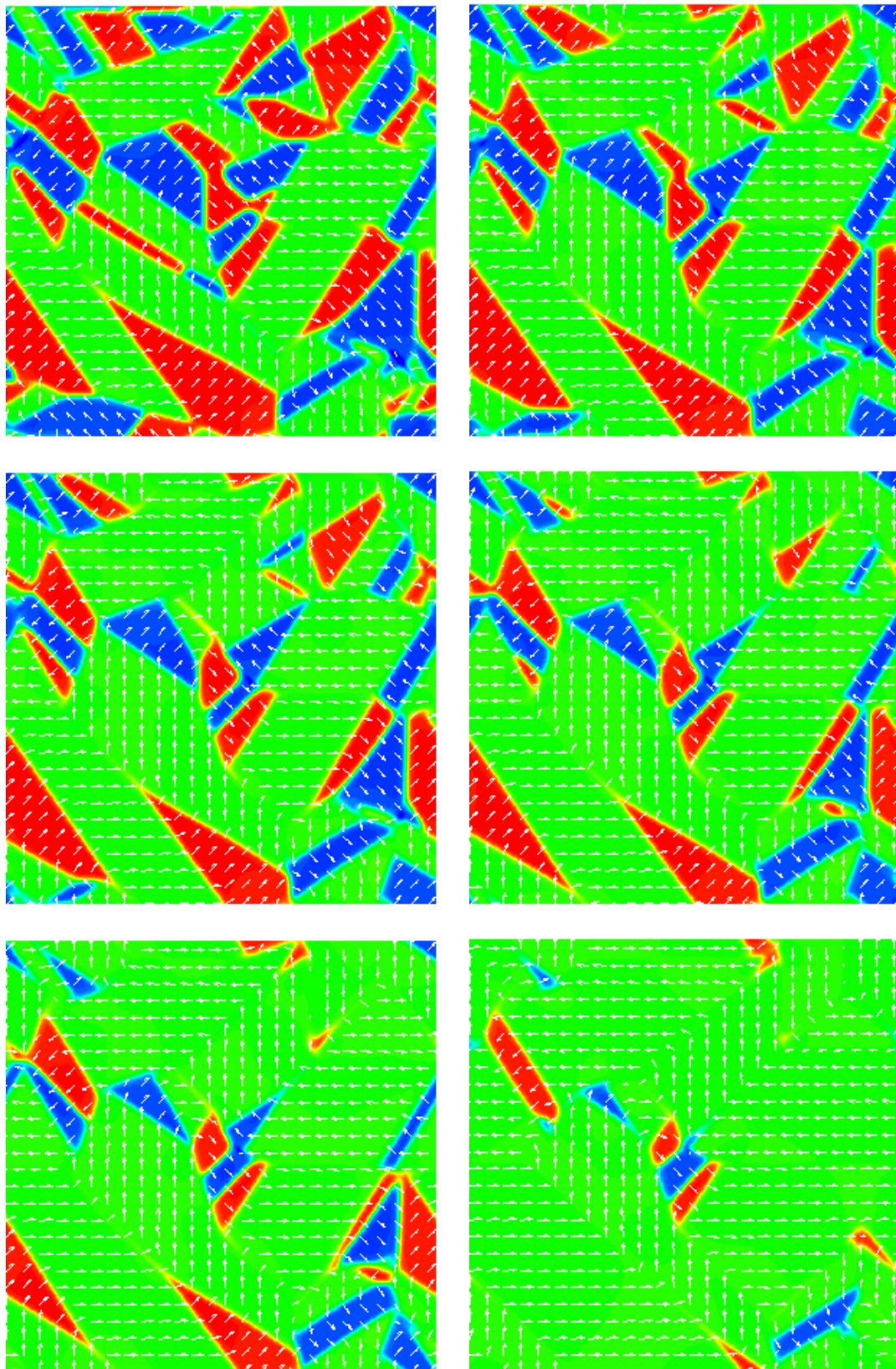


FIG. 3-4. (After ref. 2). Computer simulation of bridging domains and mosaic domain microstructures of coexisting phases in PZT system at room temperature with near MPB compositions: (a)  $x=0.49$  and (b)  $x=0.50$ . Arrows represent the in-plane components of polarization vector, and the out-of-plane component is represented by color, where green domains are tetragonal phase, red and blue domains are rhombohedral phase. Minor domains of metastable phase spontaneously coexist with and bridge major domains of stable phase and together form mosaic domain microstructures to reduce total system free energy. The coupled ferroelectric and ferroelastic domain microstructures lead to spontaneous phase coexistence in compositionally homogeneous system around MPB.

In the simulated phase-coexisting mosaic domain microstructures (Fig. 3-4), the domains of tetragonal phase form structural (ferroelastic) twins of  $\{110\}$  twin planes, where the twin boundaries are also  $90^\circ$  ferroelectric domain walls; the domains of rhombohedral phase form twins of either  $\{100\}$  or  $\{110\}$  twin planes, where the twin boundaries are  $109^\circ$  and  $71^\circ$  ferroelectric domain walls, respectively. This observation is in agreement with the crystallographic analysis of domain microstructures simultaneously minimizing elastostatic and electrostatic energies. The more interesting observation, however, is the spontaneous coexistence of minor phase that bridges the domains of major phase. The existence of minor phase as bridging domains reduces both elastostatic energy, electrostatic energy and polarization gradient energy in complex domain microstructures, which arise from the frustrations caused by the crystal lattice misfit among multiple structural orientation variants and the polarization distribution among multiple polar axes.

It is worth noting that the transformation twinning mechanism can completely self-accommodate the lattice misfit only within one set of twin-related lamellar domains composed of two structural variants with same twin plane orientation, i.e., polytwin.<sup>32</sup> A

coherent domain microstructure consisting of multiple structural variants inevitably generates disclination-like and/or dislocation-like internal stresses, even in single-phase single crystals with each pair of neighboring domains forming twins.<sup>32</sup> It is the relaxation of elastostatic energy associated with such internal stresses that drives the formation of bridging domains of minor phase, and leads to phase coexistence. In particular, the disclinations caused by the rigid-body rotations of multiple twin-forming structural variants stabilize the bridging domains of minor phase. As shown in Fig. 3-4, the inter-phase interfaces exhibit preferred orientations, which are close to either {350} or {250}. Analysis shows that such interface orientations minimize the interfacial charge density associated with polarization gradient across the inter-phase interfaces, i.e.,  $(\mathbf{P}^R - \mathbf{P}^T) \cdot \mathbf{n} \approx 0$ , where  $\mathbf{n}$  is the interface normal vector, and  $\mathbf{P}^R$  and  $\mathbf{P}^T$  are the polarization vectors in the neighboring rhombohedral and tetragonal domains, respectively. In particular, {350} and {250} inter-phase interfaces are respectively 55° and 125° domain walls between rhombohedral and tetragonal phases, and {350} is favored over {250} because of its lower polarization gradient energy, as confirmed by our simulations shown in Fig. 3-4, i.e., the characteristic triangular bridging domains have two {350} and one {250} interfaces. Three-dimensional simulation is underway to investigate the polyhedral shapes and interface orientations of the bridging domains.

Bridging domain also provides a low-energy pathway for polarization transition among different polar axes of the major phase, as shown in Fig. 3-5. It is shown that, to rotate the polarization from one stable variant to other energy equivalent stable variants, the best paths that increase minimum amount of energy are through the metastable

variants, i.e., one tetragonal to other tetragonal variants through rhombohedral variants, and one rhombohedral to other rhombohedral variants through tetragonal variants.

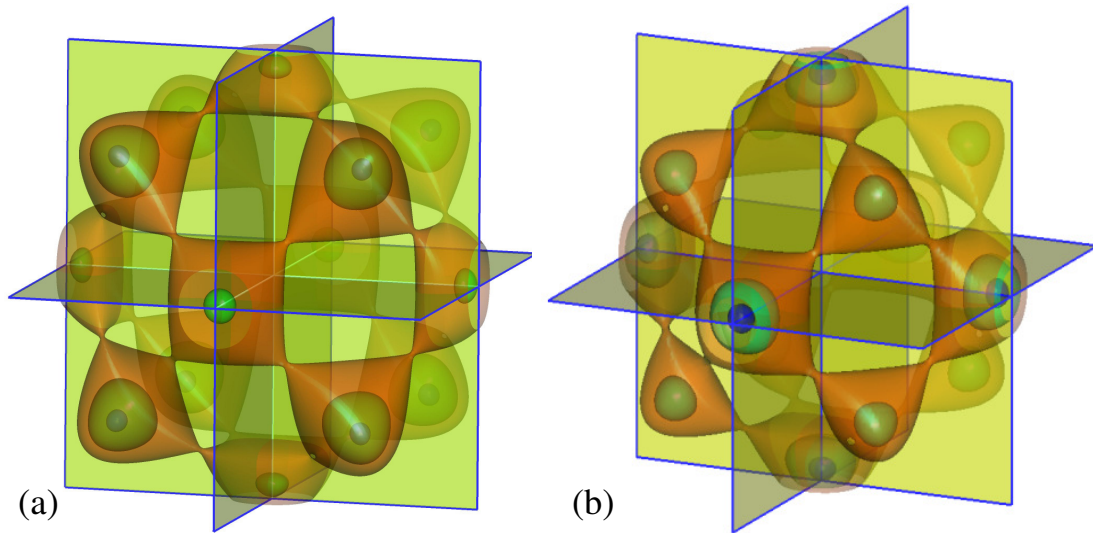


FIG. 3-5. Free energies of ferroelectrics around MPB in the polarization space (calculated from ref. 30) on (a) the rhombohedral side, and (b) tetragonal side. The energy space is defined by three components of the polarization vector in the crystallographic coordinate system aligned with  $\langle 100 \rangle$  lattice axes of the parent cubic phase, where  $\{100\}$  planes intersected at the origin are shown as transparent films. Free energy associated with each polarization state, i.e., every combination of  $(P_x, P_y, P_z)$ , is calculated for the whole space, but only iso-surfaces are drawn out to show positions of equal energy states through the space. Energy states inside the blue spheres are lower than those enclosed by the green shapes, inside the green are lower than inside the orange, and outside are higher than all insides. Thus, the lowest energy states are confined along  $\langle 111 \rangle$  and  $\langle 100 \rangle$  directions on (a) rhombohedral side and (b) tetragonal side, respectively, and those states are connected by the metastable states along  $\langle 100 \rangle$  and  $\langle 111 \rangle$  directions on (a) rhombohedral side and (b) tetragonal side, respectively.

Formation of bridging domains of minor phase increases the bulk free energy of the ferroelectric system. In the vicinity of MPB, the bulk energy gap between rhombohedral and tetragonal phases is small, thus the bulk free energy increase is over-counterbalanced



by the elastostatic energy relaxation, leading to decrease in total system free energy. With compositions increasingly deviated from the MPB, the bulk energy gap becomes increasingly large, resulting in prohibitively high energy cost for minor phase formation. Our simulations with compositions  $x=0.48$  and  $x=0.51$  show diminishing amount of minor phase and bridging domains. Therefore, bridging domain mechanism can operate only in the vicinity of MPB, and lead to phase coexistence around MPB. Taking MPB as located at the composition where the two phases coexist in equal quantity,<sup>4</sup> the simulations indicates that the MPB is located at composition between  $x=0.49$  and  $0.50$ .

Phase coexistence due to bridging domain mechanism is expected for a wider composition range around MPB in polycrystalline ceramics than in single crystals. This is because grain boundary constraints generate larger internal stresses in polycrystal grains, as has been investigated in ferroelastic (martensitic) systems.<sup>33,34</sup> The larger internal stresses tend to stabilize the bridging domains of minor phases over a wider composition range around MPB. Phase coexistence in ferroelectric ceramics will be presented in the next section.

It is worth noting that the MPB location between  $x=0.49$  and  $0.50$  determined by the domain microstructure simulations according to equal volume fraction of coexisting phases (i.e., domain criterion) is about 0.01 higher than the composition  $x\approx 0.483$  from the experimentally fitted LGD polynomial.<sup>30</sup> In LGD theory, MPB is defined as the composition where the rhombohedral and tetragonal phases have equal bulk free energy under stress-free condition (i.e., energy criterion), which is one of the fitting criteria.<sup>30</sup> LGD theory assumes a stress-free homogeneous state (i.e., single-phase single-domain single crystal), while experimental data around MPB are obtained from internally stressed

heterogeneous state (i.e., multi-phase multi-domain polycrystal). Therefore, the experimentally determined LGD polynomial inherently incorporates the inhomogeneity effects, thus deviating from the free energy function of a stress-free homogeneous ferroelectric state (the latter is required for domain simulations). As a result of the inconsistency between domain and energy criteria, when the domain microstructure-dependent long-range interaction energies are taken into account, MPB determined by domain criterion deviates from that determined by energy criterion based on such an experimentally fitted LGD polynomial, which will be shown in the next section. Investigation is underway to improve LGD polynomial by taking into account the multi-domain and/or multi-phase effects, which would better describe the intrinsic thermodynamic properties of a ferroelectric system.

The spontaneously formed phase-coexisting mosaic domain microstructure corresponds to an energy-minimizing state. An externally applied electric field can induce a configurational change in the domain microstructure, deviating from the local minimum-energy state. The field-induced microstructure will automatically return to its original minimum-energy state upon removal of external field, leading to a ferroelectric shape memory effect. The configurational change is achieved through domain wall motion and inter-ferroelectric phase transition. The ferroelectric shape memory effect associated with the phase-coexisting mosaic domain microstructure in the vicinity of MPB produces large macroscopic electromechanical response, which explains the enhanced piezoelectricity around MPB. Detailed simulation studies of ferroelectric shape memory effect will be reported in chapter IV.

## III.4. Grain Size effect

In this section, computer modeling and simulation reveals a grain size- and composition-dependent behavior of phase coexistence around the morphotropic phase boundaries in polycrystals of ferroelectric solid solutions. It shows that domain microstructures and mechanisms play important roles in phase coexistence phenomenon, where minor domains of metastable phase coexist with and bridge major domains of stable phase to effectively reduce elastostatic, electrostatic and domain wall energies. It also shows that grain boundaries impose internal mechanical and electric boundary conditions, which affect the phase-coexisting domain microstructures in the grains and give rise to the grain size dependence of phase coexistence composition range.

Our previous computer modeling and simulation studies of polar domain microstructures in single crystals of MPB-based ferroelectric solid solutions showed that electrostatic and elastostatic interactions play important roles in the MPB phase coexistence phenomenon through the formation of coupled ferroelectric and ferroelastic domain microstructures which are produced by either displacive phase transformation (diffusionless)<sup>2</sup> or coherent phase decomposition (diffusional).<sup>1</sup> The phase-coexisting domain microstructures effectively reduces the system's total free energy, including bulk free energy, domain wall energy, and long-range electrostatic and elastostatic energies. Similar phase coexistence phenomenon is also reported in the computer simulation of epitaxially strained ferroelectric thin films.<sup>36</sup> In this section, we study ferroelectric polycrystalline ceramics. The purpose is to report grain size-dependent behavior and underlying mechanism of phase coexistence in polycrystals, where the width of phase

coexistence composition range increases with decreasing grain sizes. In particular, we investigate the effects of internal mechanical and electric boundary conditions imposed by grain boundaries, which affect the phase-coexisting domain microstructures in the grains.

Grain size effect of phase coexistence is a particularly important issue in PZT systems. PZT is the current material of choice for a wide variety of high-performance electromechanical devices. Since PZT is intractable for single crystal growth, polycrystalline ceramics is the material form for practical applications. In this work, we use the material parameters experimentally determined for PZT<sup>29-31</sup> in our modeling and simulation to investigate the effects of grain boundaries and grain sizes.

The computer simulations reveal a grain size effect of phase coexistence around the MPB in ferroelectric polycrystals, as shown in Figs.3-6 and 3-7. Two-dimensional polycrystalline structure of 16 grains is generated by using Voronoi tessellation,<sup>33-35</sup> with grain orientation distributed within  $\pm 45^\circ$ . In order to separate grain size effect from other effects, the same polycrystalline grain structure (i.e., grain shape, location and orientation) is used in all simulations. Different grain sizes are simulated by using different numbers of discrete computational grids  $N \times N$ , with  $N=128, 256, \text{ and } 512$ , respectively. A range of compositions around MPB (i.e., mole fraction of PT  $0.40 \leq x \leq 0.56$ ) are simulated. For better comparison with experimental results, statistical average is performed among 10 phase fraction values individually simulated with different random initial conditions for same specific composition and grain size. This procedure is necessary because the simulation volume only represents a small portion of polycrystalline ceramic or powder samples used in diffraction experiments (a

conventional technique for phase characterization), where different parts of the samples develop different domain microstructures and diffraction experiments measure the average phase fractions. The individual and averaged volume fraction values of tetragonal phase are shown as open and filled symbols, respectively, in Fig. 3-6. Some representative phase-coexisting domain microstructures from individual simulations for different compositions and grain sizes are shown in Fig. 3-7.

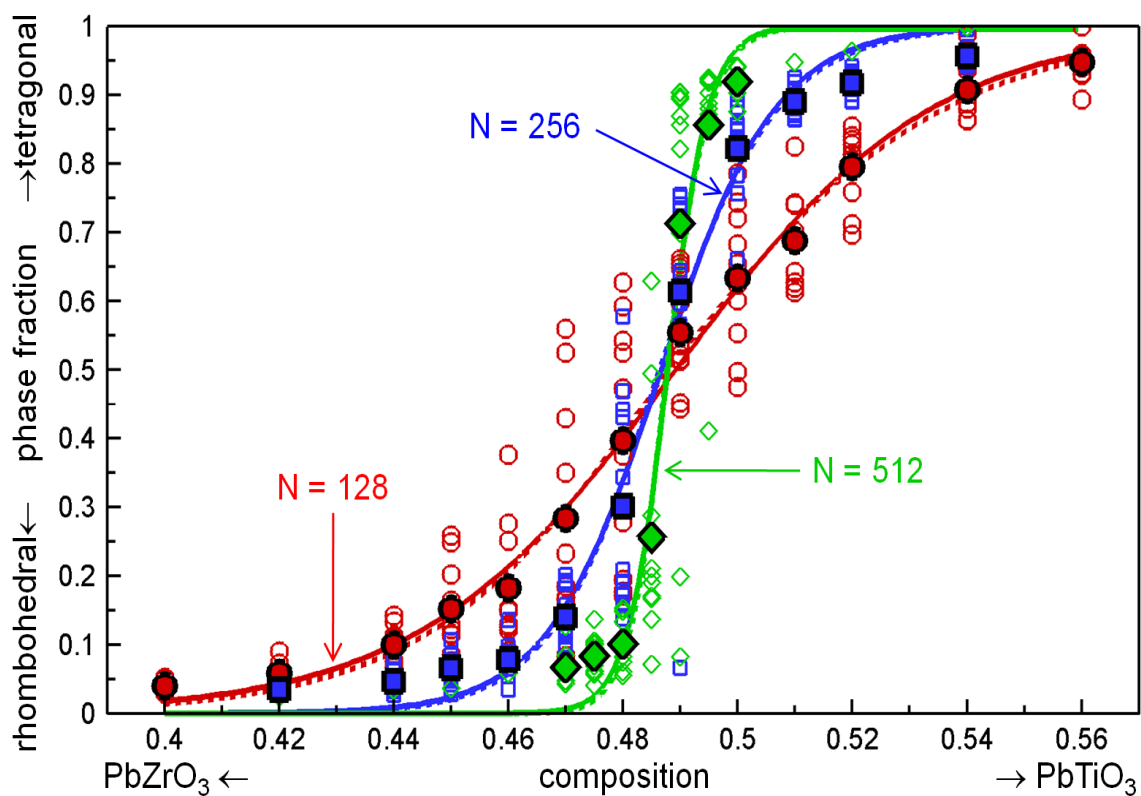


FIG. 3-6. (After ref. 3). Computer simulation of grain size-dependent phase coexistence phenomenon around MPB in ferroelectric polycrystals. The volume fraction of tetragonal phase is plotted versus the mole fraction of PT for various grain sizes. The width of phase coexistence composition range decreases with increasing grain size (simulation system size  $N$ ). The open symbols represent individual simulation results from random initial conditions. Each of the filled symbols represents the average of 10 simulation results for same specific composition and grain size. The solid and dashed lines are the fitting curves by using symmetric and asymmetric functions, respectively.

Fig. 3-6 plots the volume fraction of tetragonal phase versus the mole fraction of PT for different grain sizes. It shows that the tetragonal phase fraction smoothly increases across the MPB from rhombohedral side to tetragonal side. Thus, there is a composition range of phase coexistence around the MPB. The simulated data are widely scattered for near-MPB compositions and become narrowly distributed for compositions away from the MPB. The average data points well follow the analytical functions:

$$f_{\text{sym}}(x) = \frac{e^{\frac{x-x_0}{\tau}}}{1 + e^{\frac{x-x_0}{\tau}}}, \quad (26a)$$

$$f_{\text{asym}}(x) = \left[ 1 - h(x - x_0) \right] \frac{e^{\frac{x-x_0}{\tau_1}}}{1 + e^{\frac{x-x_0}{\tau_1}}} + h(x - x_0) \frac{e^{\frac{x-x_0}{\tau_2}}}{1 + e^{\frac{x-x_0}{\tau_2}}}, \quad (26b)$$

where  $h(x)$  is the Heaviside step function, and the parameters are obtained by data fitting and listed in Table 1. In particular, the value  $\tau$  is a measure of the width of phase coexistence composition range. The difference between symmetric (solid line in Fig. 3-6) and asymmetric (dashed line in Fig. 3-6) fitting functions, i.e.,  $\tau_1 < \tau < \tau_2$ , is consistent with the fact that the energy gap between stable and metastable phases increases slightly faster with composition deviation from MPB on rhombohedral side than on tetragonal side, according to the LGD polynomial<sup>30</sup> used in our simulations. Most importantly, Fig. 3-6 reveals a grain size effect of phase coexistence around the MPB in ferroelectric polycrystals: the width of phase coexistence composition range increases with decreasing grain size, as quantified by the values of  $\tau$  in Table 1. The underlying mechanisms are revealed in Fig. 3-7.

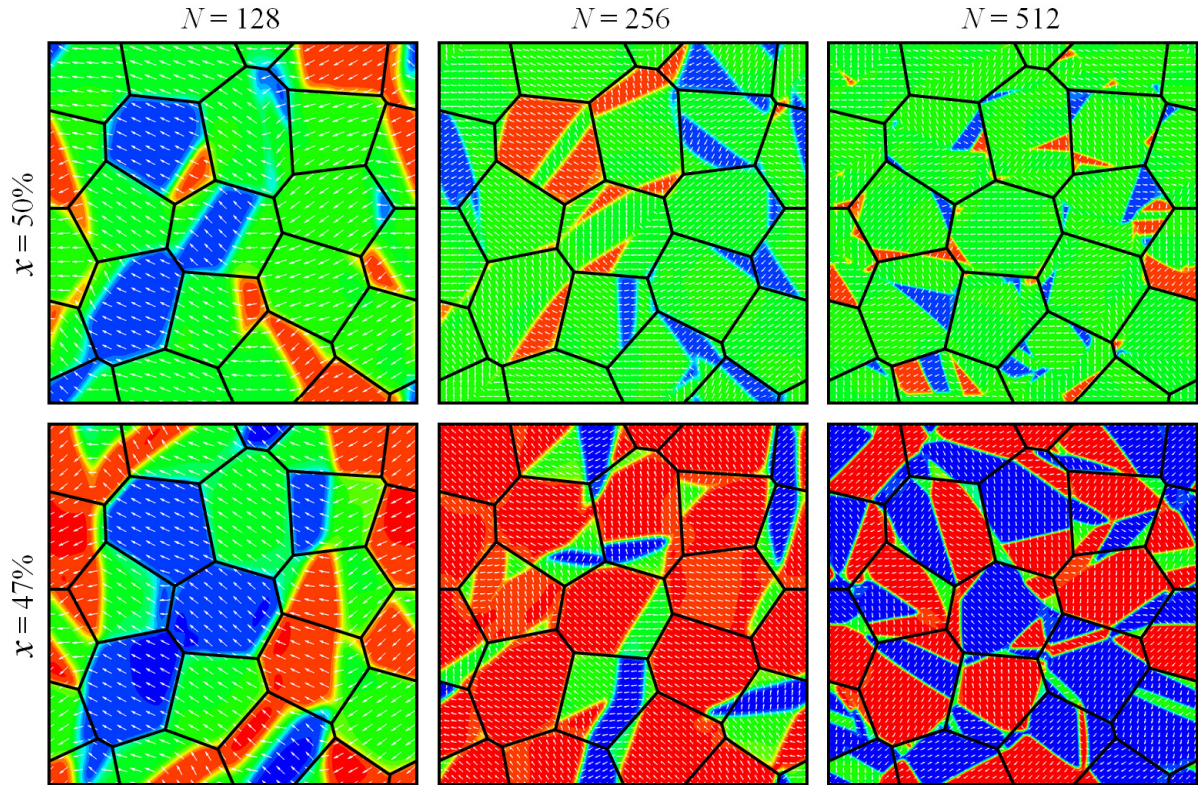


FIG. 3-7. (After ref. 3). Computer simulation of grain size- and composition-dependent phase-coexisting domain microstructures around MPB in ferroelectric polycrystals. Same polycrystalline grain structures with different grain sizes (simulation system size  $N$ ) and compositions (mole fraction  $x$ ) are simulated. Arrows represent the in-plane components of polarization vector, and the out-of-plane component is represented by color, where green domains are tetragonal phase, red and blue domains are rhombohedral phase.

Fig. 3-7 shows representative phase-coexisting domain microstructures in polycrystals from individual simulations for different compositions and grain sizes. As in the case of single crystals,<sup>2</sup> due to the small bulk free energy gap between metastable and stable phases in the vicinity of MPBs, minor domains of metastable phase spontaneously coexist with and bridge major domains of stable phase and together form mosaic domain microstructures. The existence of minor phase as bridging domains reduces elastostatic, electrostatic and polarization gradient (domain wall) energies of complex domain

microstructures, which arise from the frustrations caused by both the crystal lattice misfit and the polarization distribution among multiple polar domain variants. With compositions deviated from the MPB, the bulk energy gap becomes large, thus the energy cost of minor phase formation is high and the volume fraction of metastable phase decreases. This bridging domain mechanism gives rise to the composition-dependent phase coexistence behavior, as described by Eq. (26). In polycrystals, the grain boundaries impose internal mechanical and electric boundary conditions, which affect the phase-coexisting domain microstructures in the grains. High internal stresses usually develop around grain boundaries and especially their junctions, where electric charges also accumulate because of grain misorientation. As a result, minor domains of metastable phase preferably form near grain boundaries and their junctions, as shown in Fig. 3-7. Fig. 3-7 also shows that the effects of grain boundaries are more significant for smaller grains. This mechanism explains the grain size-dependent phase coexistence behavior: phases coexist over a wider composition range around MPB in polycrystals of smaller grains, where the larger internal stresses and charge accumulation tend to stabilize the bridging domains of minor phases.

Table 1. Parameter values of the functions in Eq. (26) obtained by fitting to the simulation data. (After Ref. 3).

$N$	$x_0$	$\tau$	$x_0$	$\tau_1$	$\tau_2$
128	0.4891	0.0223	0.4878	0.0207	0.0242
256	0.4867	0.0099	0.4863	0.0094	0.0103
512	0.4878	0.0035	0.4876	0.0032	0.0038

The simulation results presented in Figs. 3-6 and 3-7 show that the domain microstructures and phase volume fractions vary widely from grain to grain. Thus,



experimental observations based on imaging of local domain microstructures may not provide a reliable measurement of the volume fractions of coexisting phases in the whole polycrystalline sample. The conventionally used diffraction method is the appropriate technique to characterize phase coexistence and measure the average amount of each phase. The findings also suggest that MPB phase coexistence could be engineered through control of grain sizes, i.e., phase coexistence can be stabilized in fine-grained polycrystalline ceramics, while suppressed in coarse-grained materials.

It is worth noting that the presence of MPB as a sharp line phase boundary violates the Gibbs phase rule of equilibrium thermodynamics,<sup>7</sup> indicating that the MPB-based phase diagram is a nonequilibrium (or diffusionless) one due to limited diffusion kinetics in complex oxide solid solution. It has been long-recognized that a two-phase zone is required for PZT around MPB, and the MPB is experimentally considered as located at the composition where the rhombohedral and tetragonal phases coexist in equal quantity<sup>4</sup> (we call this definition of MPB *experimental criterion*). In the developed LGD theory, the position of MPB corresponds to the composition where the rhombohedral and tetragonal phases have equal free energy density under stress-free condition without external electric field (*theoretical criterion*).<sup>30,37-42</sup> As one fitting requirement, the fitted LGD free energy function reproduces the MPB at experimentally observed composition.<sup>30,37-42</sup> It is worth noting that the *theoretical* and *experimental* criteria address different material states: LGD theory assumes an equilibrium, homogeneous state (i.e., single-phase, single-domain, single-crystal, stress-free, no external electric field), while in experiments the PZT samples are highly heterogeneous, nonequilibrium systems (i.e., polycrystalline ceramics consisting of multiple domains and coexisting phases and

under nonuniform internal stress and electric field), in particular around MPB. In such a complex heterogeneous ferroelectric system, long-range electrostatic and elastostatic interactions play important roles in domain formation and phase coexistence, as has been demonstrated early. Therefore, as pointed out in the previous section, the two criteria in defining MPB are not equivalent, that is, the equal quantity of coexisting phases (*experimental criterion*) does not necessarily imply the equality of free energy density of the two phases (*theoretical criterion*), due to the domain microstructure-dependent electrostatic and elastostatic interaction energies, which again raises the same concern about whether or not the developed LGD theory<sup>30,37-42</sup> mainly based on polycrystalline ceramics data can be reliably applied to single-phase and single-domain single crystals to investigate the intrinsic electrostrictive and piezoelectric properties.

For demonstrating the difference between these criteria, we apply the same grain structure with  $N = 256$  to simulate the domain microstructures by using two fitted LGD polynomials and the corresponding electrostrictive coefficients,<sup>30,37-42</sup> and plot the volume fraction of tetragonal phase versus the mole fraction of PT again in Fig. 3-8. It is clearly shown that, although the fitted free energy function predicts the position of MPB in homogeneous state very well, directly applying them in heterogeneous and nonequilibrium systems does not give the correct location of MPB. It is worthy to note that even the structural twins between two adjacent rhombohedral domains, which are required by crystallographic analysis of domain microstructures simultaneously minimizing elastostatic and electrostatic energies, can not be correctly reproduced by directly applying the fitted function.

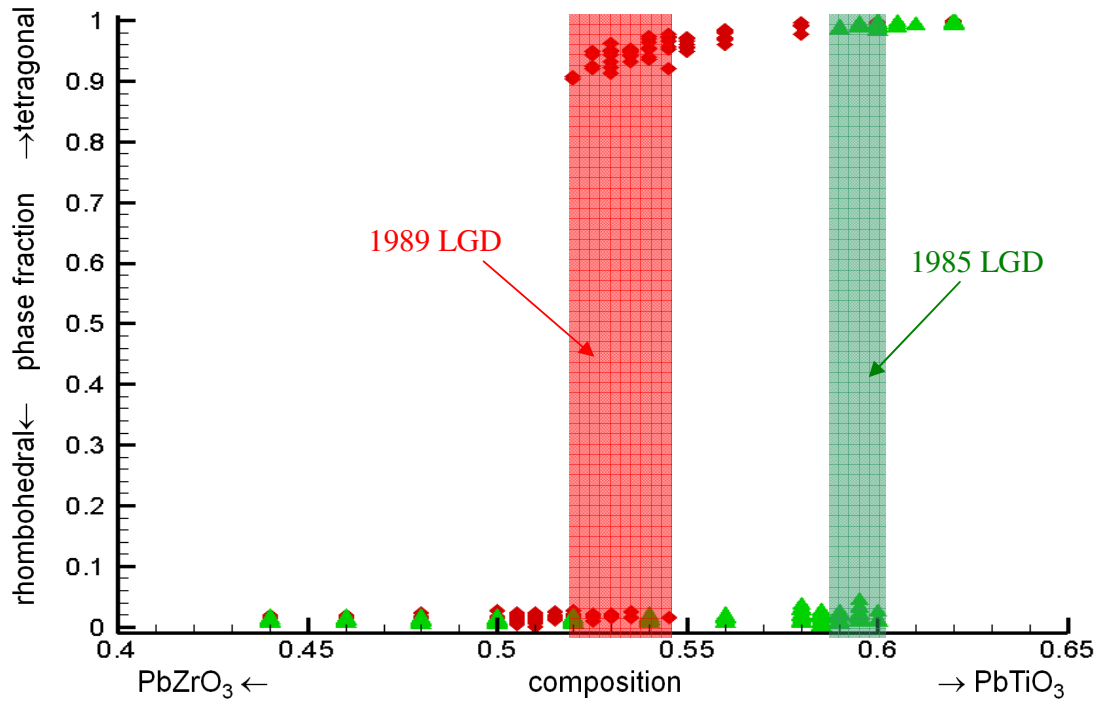


FIG. 3-8. Volume fraction of tetragonal phase versus the mole fraction of PT for  $N=256$ . The ranges of phase coexistence composition are shaded with different colors for two sets of LGD polynomials. The symbols (red diamonds and green triangles are for LGD 1989<sup>37-42</sup> and LGD 1985,<sup>30</sup> respectively) represent individual simulation results from random initials.

### III.5. References

1. W.F. Rao and Y.U. Wang, Appl. Phys. Lett. **91**, 052901 (2007).
2. W.F. Rao and Y.U. Wang, Appl. Phys. Lett. **90**, 182906 (2007).
3. W.F. Rao and Y.U. Wang, Appl. Phys. Lett. **92**, 102905 (2008).
4. B. Jaffe, W.R. Cook, and H. Jaffe, Piezoelectric Ceramics (Academic Press, London, 1971).
5. J. Kuwata, K. Uchino, and S. Nomura, Ferroelectrics **37**, 579 (1981).
6. S.W. Choi, T.R. Shrout, S.J. Jang, and A.S. Bhalla, Ferroelectrics **100**, 29 (1989).
7. G.A. Rossetti, Jr., W. Zhang, and A.G. Khachaturyan, Appl. Phys. Lett. **88**, 072912

- (2006).
8. A.M. Glazer, P.A. Thomas, K.Z. Baba-Kishi, G.K.H. Pang, and C.W. Tai, *Phys. Rev. B* **70**, 184123 (2004).
  9. J. Kuwata, K. Uchino, and S. Nomura, *Jpn. J. Appl. Phys.* **21**, 1298 (1982).
  10. T.R. Shrout, Z.P. Chang, N. Kim, and S. Markgraf, *Ferroelectrics Lett.* **12**, 63 (1990).
  11. S.E. Park and T.R. Shrout, *J. Appl. Phys.* **82**, 1804 (1997).
  12. For complete references to the new intermediate MPB phases, see recent review: B. Noheda and D.E. Cox, *Phase Transitions* **79**, 5 (2006).
  13. Y.U. Wang, *Phys. Rev. B* **74**, 104109 (2006); *Phys. Rev. B* **76**, 024108 (2007).
  14. Y.M. Jin, Y.U. Wang, A.G. Khachatryan, J.F. Li, and D. Viehland, *Phys. Rev. Lett.* **91**, 197601 (2003); *J. Appl. Phys.* **94**, 3629 (2003).
  15. Y.U. Wang, *Phys. Rev. B* **73**, 014113 (2006).
  16. H. Wang, J. Zhu, N. Lu, A. A. Bokov, Z. G. Ye, and X. W. Zhang, *Appl. Phys. Lett.* **89**, 042908 (2006).
  17. H. Wang, J. Zhu, X.W. Zhang, Y. X. Tang, and H. S. Luo, *J. Am. Ceram. Soc.* **91**, 2382 (2008).
  18. L.A. Schmitt, K.A. Schönau, R. Theissmann, H. Fuess, H. Kungl, and M. J. Hoffmann, *J. Appl. Phys.* **101**, 074107 (2007).
  19. R. Theissmann, L.A. Schmitt, J. Kling, R. Schierholz, K. A. Schönau, H. Fuess, M. Knapp, H. Kungl, and M. J. Hoffmann, *J. Appl. Phys.* **102**, 024111 (2007).
  20. K.A. Schönau, L.A. Schmitt, M. Knapp, H. Fuess, R. A. Eichel, H. Kungl, and M. J. Hoffmann, *Phys. Rev. B* **75**, 184117 (2007).
  21. K.A. Schönau, M. Knapp, H. Kungl, M. J. Hoffmann, and H. Fuess, *Phys. Rev. B* **76**, 144112 (2007).
  22. V.A. Isupov, *Sov. Phys. Solid State* **10**, 989 (1968) [*Fiz. Tverd. Tela* **10**, 1244 (1968)]; *Phys. Solid State* **43**, 2262 (2001) [*Fiz. Tverd. Tela* **43**, 2171 (2001)]; *Ferroelectrics* **266**, 91 (2002).
  23. L. Benguigui, *Solid State Commun.* **11**, 825 (1972); P. Ari-Gur and L. Benguigui, , *Solid State Commun.* **15**, 1077 (1974).
  24. K. Kakegawa, J. Mohri, T. Takahashi, H. Yamamura, and S. Shirasaki, *Solid State*

- Commun. **24**, 769 (1977); K. Kakegawa, J. Mohri, S. Shirasaki, and K. Takahashi, J. Am. Ceram. Soc. **65**, 515 (1982).
25. W. Cao and L.E. Cross, Phys. Rev. B **47**, 4825 (1993).
  26. G.A. Rossetti, Jr. and A.G. Khachaturyan, Appl. Phys. Lett. **91**, 072909 (2007).
  27. A.F. Devonshire, Philos. Mag. **40**, 1040 (1949).
  28. M.V. Rane, A. Navrotsky, and G.A. Rossetti, Jr., J. Solid State Chem. **161**, 402 (2001).
  29. W.F. Rao and Y.U. Wang, “*Intrinsic Electrostrictive and Piezoelectric Properties of Lead Zirconate Titanate (PZT): Analysis of Diffraction Data*” (to be published).
  30. A. Amin, M. J. Haun, B. Badger, H. McKinstry, and L. E. Cross, Ferroelectrics **65**, 107 (1985).
  31. T. Fett and D. Munz, J. Test. Eval. **28**, 27 (2000).
  32. L. A. Bendersky, A. Roytburd, and W. J. Boettinger, Acta Metall. Mater. **42**, 2323 (1994).
  33. Y. M. Jin, A. Artemev, and A. G. Khachaturyan, Acta Mater. **49**, 2309 (2001).
  34. Y. U. Wang, Y. M. Jin, and A. G. Khachaturyan, Acta Mater. **52**, 1039 (2004).
  35. Y. M. Jin, Y. U. Wang, A. Kazaryan, Y. Wang, D. E. Laughlin, and A. G. Khachaturyan, J. Appl. Phys. **92**, 6172 (2002).
  36. Y.L. Li, S. Choudhury, Z.K. Liu, and L.Q. Chen, Appl. Phys. Lett. **83**, 1608 (2003); Y.L. Li and L.Q. Chen, *ibid.* **88**, 072905 (2006); S. Choudhury, Y. Li, and L.Q. Chen, J. Am. Ceram. Soc. **88**, 1669 (2005).
  37. M.J. Haun, E. Furman, S.J. Jang, and L.E. Cross, Ferroelectrics **99**, 13 (1989).
  38. M.J. Haun, E. Furman, H.A. McKinstry, and L.E. Cross, Ferroelectrics **99**, 27 (1989).
  39. M.J. Haun, Z.Q. Zhuang, E. Furman, S.J. Jang, and L.E. Cross, Ferroelectrics **99**, 45 (1989).
  40. M.J. Haun, E. Furman, T.R. Halemane, and L.E. Cross, Ferroelectrics **99**, 55 (1989).
  41. M.J. Haun, E. Furman, S.J. Jang, and L.E. Cross, Ferroelectrics **99**, 63 (1989).
  42. M.J. Haun, Z.Q. Zhuang, E. Furman, S.J. Jang, and L.E. Cross, J. Am. Ceram. Soc. **72**, 1140 (1989).

# Chapter IV

## Crystallographic Domain Engineering

### IV.1. Introduction

High-performance piezoelectrics for sensors, actuators and transducers are expected to exhibit large reversible strain free from hysteresis under electric field. However, the conventional strain mechanisms, such as electric field-induced domain wall motion and phase transition, though provide large spontaneous strain, are accompanied by large hysteresis and/or irreversibility. On the other hand, while the intrinsic response of single-phase single-domain ferroelectrics is hysteresis free, the strain induced is small. Recently, an important advance in piezoelectrics research is the development of crystallographic domain engineering technique for ferroelectric single crystals.<sup>4,5</sup> Single crystal with engineered domain configuration shows drastically enhanced, hysteresis-free strain versus electric field ( $\epsilon$ - $E$ ) behavior along the non-polar axis rather than the conventional polar axis.<sup>4,5</sup>

The minimization of  $\varepsilon$ - $E$  hysteresis in crystallographically engineered single crystal is achieved through the inhibition of electric field-induced domain wall motion.<sup>4-7</sup> For engineered domain configuration, electric field is applied along the non-polar axis of the single crystal, which forms equal angle to the polarization vectors of individual domains. All the domains are energetically and crystallographically equivalent with respect to the electric field in non-polar direction, thus there is no driving force to domain wall motion, and electric field-induced intrinsic responses of these domains do not break such equivalency. As a result, tilted polarization remains in perfect head-to-tail patterns, and domain walls between intrinsically distorted domains are still charge-free crystallographic twin boundaries. Therefore, the piezoelectric properties of crystallographically engineered multi-domain single crystal can be predicted from the properties of a single-domain single crystal along its non-polar axis. Such single-domain intrinsic properties have been calculated and do exhibit piezoelectric anisotropy and enhanced response along non-polar axis.<sup>8-10</sup> However, they are very sensitive to the coefficients used in the calculations,<sup>11</sup> and the calculated anisotropy only accounts for a small part of the experimentally measured property enhancement.<sup>6,7</sup> Moreover, the calculation does not explain the domain size effect recently observed in the crystallographically engineered crystals,<sup>6,7</sup> where the piezoelectric properties significantly increase with decreasing domain size. Thus, further investigation of the mechanism for crystallographic domain engineering is required. In this chapter, we first report a domain wall broadening mechanism that explains the enhanced piezoelectricity and domain size effect.

The crystallographic domain engineering technique and domain size effect promise to further improve the electromechanical properties by engineering sub-micron and nanometer-sized domains and develop high-performance, environment-friendly, lead-free piezoelectrics for sensors, actuators and transducers. In order to fully exploit this technique, we need to better understand the mechanisms of crystallographic domain engineering and find optimal processing condition to control the domain microstructures and domain sizes. In the second section of this chapter, we report the control mechanisms of domain configurations and sizes in crystallographically engineered ferroelectric single crystals.

For practical application, there is another issue that must be resolved: the engineered domain microstructures are sensitive to external electric, mechanical and thermal conditions, thus method is required to stabilize the domains so that they do not change or disappear during service. Recent experimental studies<sup>12,13</sup> of ferroelectric aging phenomenon and stabilization effect in ferroelectrics provide a promising way to stabilize the engineered domain microstructures. The mechanism of aging and domain stabilization is attributed to short-range ordering of charged point defects in ferroelectric materials,<sup>12</sup> which provides a restoring force to the domains if deviated from the original domain configurations in response to external stimuli. In the last section of this chapter, we report our simulation results on the aging-stabilization of ferroelectric domains through short-range ordering of charged point defects.



## IV.2. Domain Wall Broadening Mechanism

In this section, computer modeling and simulation reveals a domain wall broadening mechanism that explains the domain size effect of enhanced piezoelectric properties recently observed in domain engineered ferroelectric single crystals. The simulation shows that, under electric field applied along the non-polar axis of single crystal which does not induce domain wall motion, the domain wall broadens and serves as embryo of field-induced new phase, producing large reversible strain free from hysteresis. This mechanism plays a significant role in the vicinity of inter-ferroelectric transition temperature and morphotropic phase boundary, where the energy difference between stable and metastable phases is small. Engineered domain configuration fully exploits this domain wall broadening mechanism.

Large reversible strain free from hysteresis under electric field is expected for high-performance piezoelectrics for sensors, actuators and transducers. Recent experiments<sup>4,5</sup> suggested that single crystal with engineered domain configuration shows drastically enhanced, hysteresis-free strain versus electric field ( $\mathcal{E}$ - $E$ ) behavior along the non-polar axis rather than the conventional polar axis. It is easy to understand that the hysteresis-free can be achieved through the inhibition of electric field-induced domain wall motion,<sup>4,7</sup> because all the domains are energetically and crystallographically equivalent with respect to the electric field in non-polar direction, the dramatic strain enhancement along the non-polar direction is, however, less understood. The intrinsic responses to the non-polar electric field were calculated by using the currently available LGD polynomials. The calculations do exhibit piezoelectric anisotropy and enhanced response

along non-polar axis.<sup>8-10</sup> However, analysis shows that the exhibited enhancement is very sensitive to the coefficients employed,<sup>11</sup> and the calculated anisotropy only accounts for a small part of the experimentally measured property enhancement.<sup>6,7</sup> Moreover, the calculation does not explain the domain size effect recently observed in the crystallographically engineered crystals,<sup>6,7</sup> where the piezoelectric properties significantly increase with decreasing domain size.

The domain size effect was discovered by directly correlating the measured piezoelectric properties to the observed domain configurations in barium titanate ( $\text{BaTiO}_3$ ) and potassium niobate ( $\text{KNbO}_3$ ) single crystals.<sup>6,7</sup> Sophisticated thermo-electrical treatment has been developed to control the domain configurations and domain sizes.<sup>6,7</sup> The micrometer-sized ( $5.5\sim 50\mu\text{m}$ ) domains allow direct domain observation and domain size measurement by polarized light microscopy.<sup>6,7</sup> Fig. 4-1(a) shows the domain size-dependent piezoelectric properties ( $d_{31}$  and  $k_{31}$ ) of [111]-oriented tetragonal  $\text{BaTiO}_3$  single crystals.<sup>7</sup> Based on the experimental data in Fig. 4-1(a), namely,  $d_{31}=-97.8, -134.7, -180.1, -230.0\text{pC/N}$  for average domain size (defined as domain width or thickness)  $t=40, 13.3, 6.5, 5.5\mu\text{m}$ , respectively, and  $d_0=-62.0\text{pC/N}$  for single domain ( $t=\infty$ ),<sup>7</sup> we calculate the property increase for engineered multi-domain configuration compared to single-domain state, i.e.,  $\Delta d_{31}=|d_{31}-d_0|$ . In Fig. 4-1(b), we plot  $\Delta d_{31}$  versus the reciprocal domain size (proportional to domain wall density),  $1/t$ . The data  $\Delta d_{31}$  and  $1/t$  are well fitted into a straight line passing the origin ( $\Delta d_{31}=0, t=\infty$ ). The polarizing microscope observation shows that the engineered multi-domain configurations are composed of tetragonal phase with  $90^\circ$ -domain walls ( $\{110\}$  twin boundaries).<sup>7</sup> Since the domains of [100], [010], and [001] polarization orientations have equal energy in [111] electric field, the  $90^\circ$ -domain

walls do not move. Thus, the quantity  $\Delta d_{31}$  excludes both the intrinsic contribution  $d_0$  from individual domains and the extrinsic contribution from domain wall motion. Therefore, the linear relationship between the property increase  $\Delta d_{31}$  and the domain wall density  $1/t$  shown in Fig. 4-1(b) unambiguously attributes the piezoelectric property enhancement and domain size effect to the domain walls themselves.

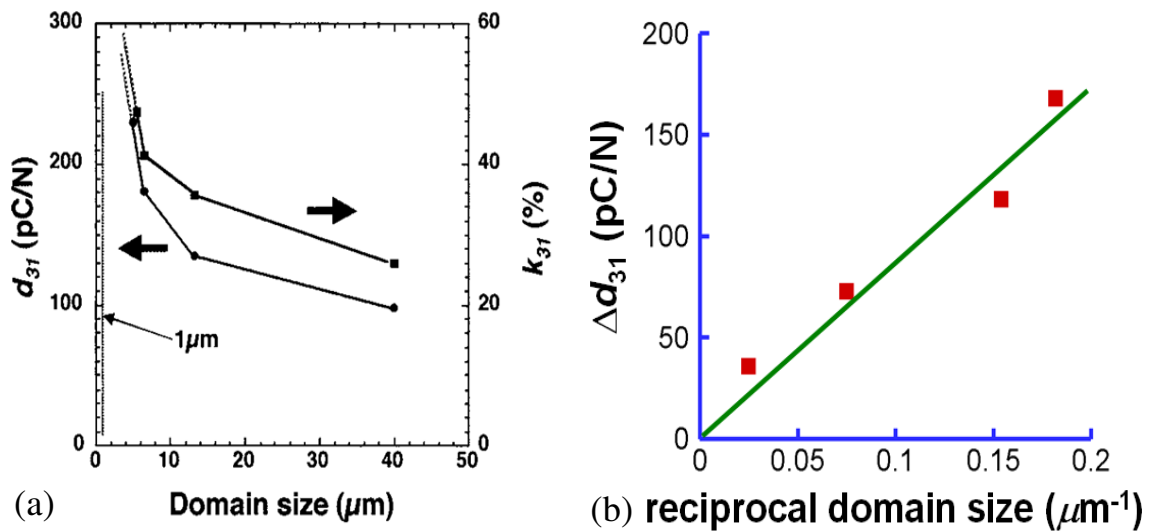


FIG. 4-1. (After ref. 1). Domain size effect in [111]-oriented tetragonal barium titanate single crystals. (a) Experimentally measured piezoelectric properties versus domain size (After ref. 7). (b) A linear relationship between the property increase  $\Delta d_{31}=|d_{31}-d_0|$  and reciprocal domain size (domain wall density), where the data (■) are calculated from (a), and the straight line is obtained by fitting. The result unambiguously attributes the piezoelectric property enhancement and domain size effect to domain walls.

A hypothesis of crystal lattice symmetry change in domain wall has been proposed to provide a qualitative explanation.<sup>14</sup> However, direct experimental observation of domain wall behavior is not available; and a quantitative picture of the competition among several energy contributions in domain wall region need to be explored, such as gradient energy of polarization rotation, elastic energy of lattice misfit, energy gap between

metastable and stable phases, and external energy associated with applied electric field. In this section, we employ computer modeling and simulation to study the underlying domain wall mechanism and clarify the role of domain walls under electric field along non-polar axis.

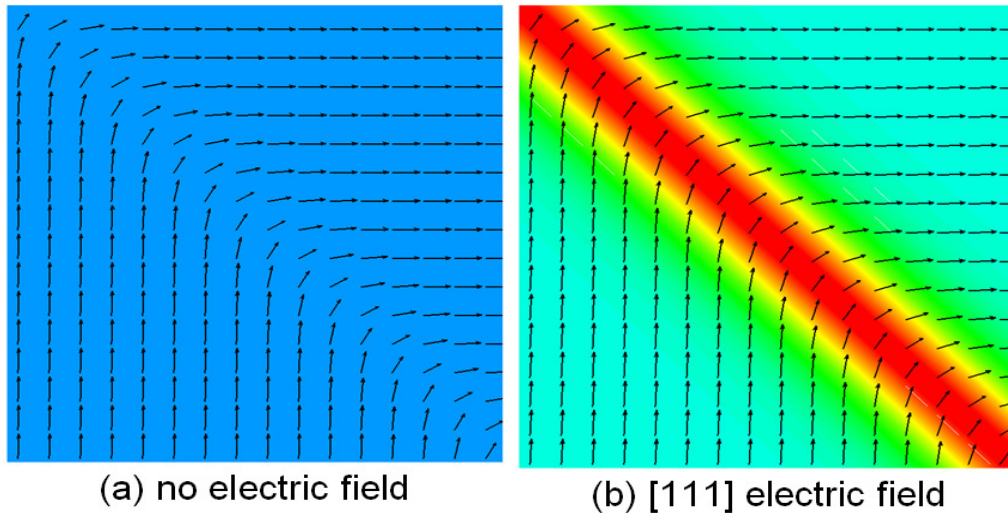


FIG. 4-2. (After ref. 1). Computer simulation of domain wall broadening behavior under electric field along non-polar axis. (a) Equilibrium  $90^\circ$ -domain wall and (110) twin boundary in tetragonal crystal without electric field. (b) Broadened domain wall composed of electric field-induced, heavily stressed [111] rhombohedral domain layer coherently sandwiched between tetragonal domains. The domain wall broadening mechanism explains the enhanced piezoelectric response along non-polar axis and the domain size (domain wall density) effect.

The computer simulation reveals a domain wall broadening mechanism, as shown in Fig. 4-2. We consider a single crystal of stable tetragonal phase with engineered domain configuration in electric field along the non-polar [111] axis. The  $90^\circ$ -domain walls are also (110) twin boundaries. Fig. 4-2(a) shows the equilibrium domain wall without electric field. The arrows represent the polarization vector distribution (the out-of-plane component is represented by color). When electric field is applied along the non-polar

[111] axis, the 90°-domain wall does not move due to the equivalent energetic state of [100] and [010] tetragonal domains, as demonstrated by the evolution sequence in Fig. 4-3. However, as shown in Fig. 4-2(b), the domain wall broadens, where a layer of heavily stressed [111] rhombohedral domain is induced by [111] electric field, which is coherently sandwiched between two adjacent stable tetragonal domains. Such an electric field-induced tetragonal→rhombohedral phase transition produces strain significantly larger than the intrinsic strain of tetragonal phase due to polarization tilting under the same electric field, leading to enhanced piezoelectric response of the single crystal.

As revealed by Fig. 4-3, the domain wall broadening behavior exhibits several important features. Firstly, the domain wall starts to broaden upon the application of electric field and gradually grows with increasing field, which produces enhanced piezoelectric response at low electric field. In this process, the 90°-domain wall serves as pre-existing embryo of the field-induced rhombohedral phase. Secondly, the broadened domain wall shrinks reversibly with decreasing electric field, which produces hysteresis-free  $\epsilon$ - $E$  curve. This reversibility is because the rhombohedral phase is metastable with respect to the stable tetragonal phase in the absence of electric field. Thirdly, the rhombohedral phase is epitaxially stressed by the tetragonal phase along (110) interfaces. Although the elastic strain energy does not favor the formation of a layer of rhombohedral phase in the domain wall, the interplay among various energetic contributions favors domain wall broadening mechanism. Finally, since the contribution of phase transformation strain to the total crystal strain is proportional to the number of domain walls present in the crystal (i.e., domain wall density), the domain wall broadening mechanism leads to the domain size effect of enhanced piezoelectricity.

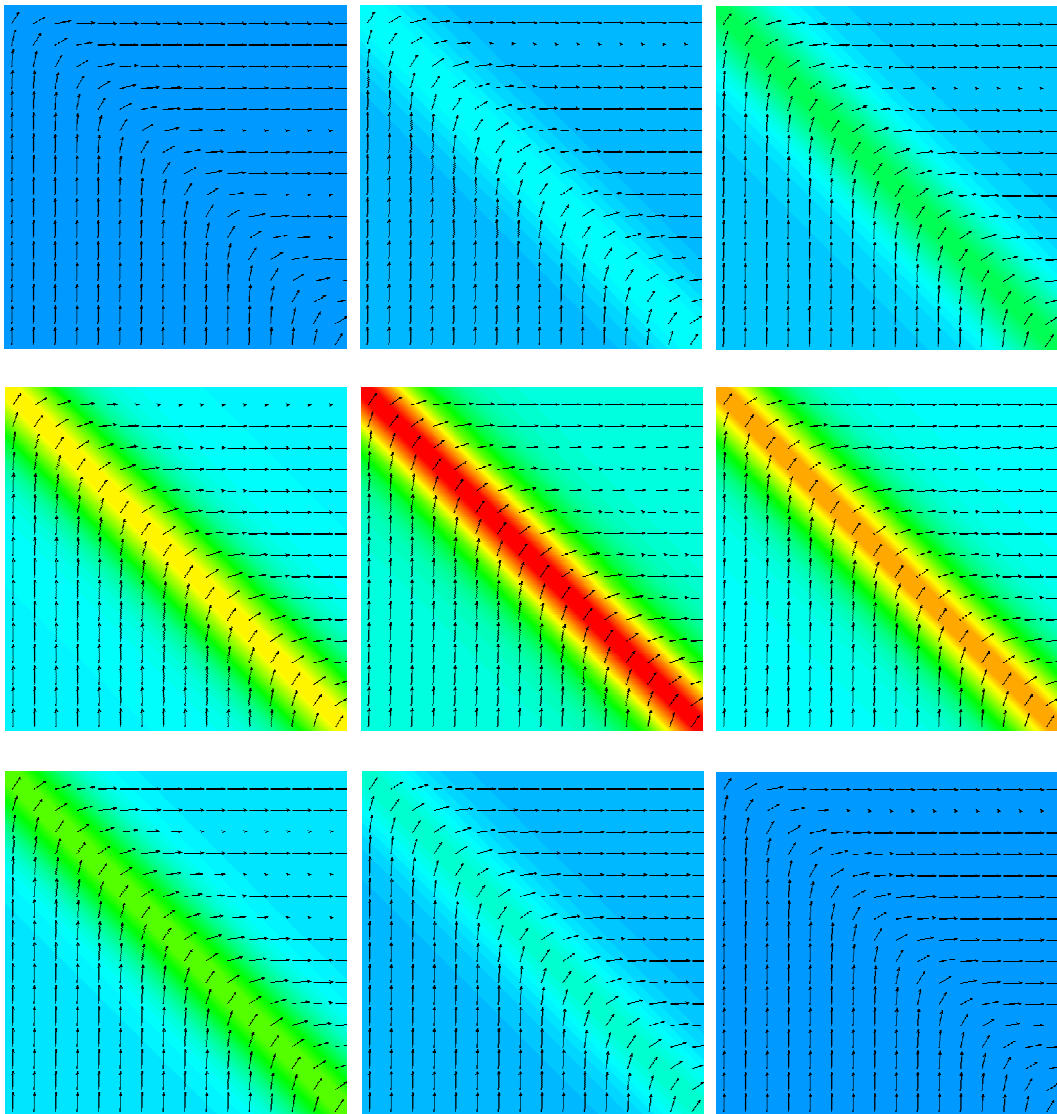
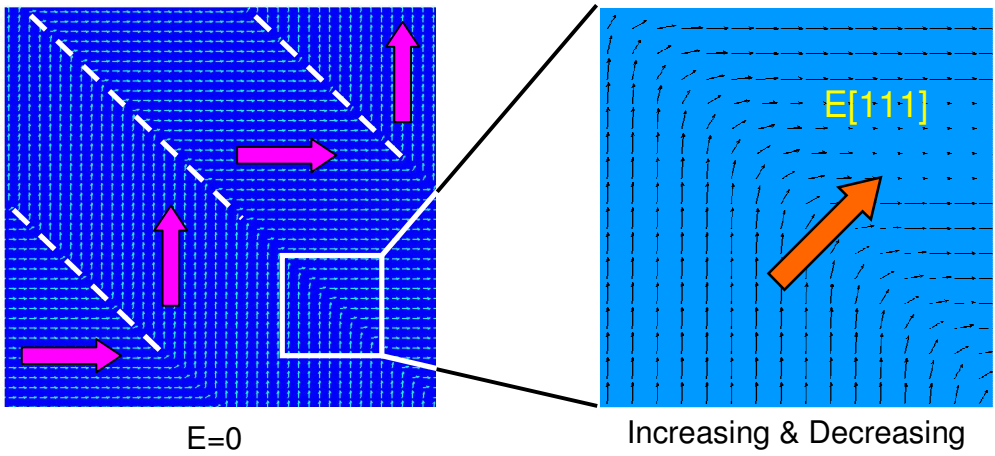


FIG. 4-3. A sequence of domain wall broadening under electric field along non-polar axis. The first two figures show the equilibrium tetragonal (110) twins and the direction of the applied electric field (along [111] non-polar direction). The rest 9 snapshots show the sequence of domain wall broadening with first increasing and then decreasing non-polar electric field, where arrows represent the in-plane components of polarization vectors, and the out-of-plane component is represented by color. It shows that with increasing electric field, a layer of the [111] rhombohedral domain is induced, and with decreasing electric field, the broadened domain wall shrinks reversibly and exactly (For providing more information, the snapshots are not taken at the same magnitudes of electric field during increasing and decreasing electric field).

It is worth noting the similarity between lead-free  $\text{BaTiO}_3$ ,  $\text{KNbO}_3$  in the vicinity of inter-ferroelectric transition temperatures and lead-based solid solutions  $\text{Pb}(\text{Zr}_{1-x}\text{Ti}_x)\text{O}_3$ ,  $\text{Pb}[(\text{Zn}_{1/3}\text{Nb}_{2/3})_{1-x}\text{Ti}_x]\text{O}_3$ ,  $\text{Pb}[(\text{Mg}_{1/3}\text{Nb}_{2/3})_{1-x}\text{Ti}_x]\text{O}_3$  in the vicinity of morphotropic phase boundaries: there exist more than one ferroelectric phases (tetragonal, rhombohedral, orthorhombic) with small energy gap but large crystal lattice transformation strain in these perovskite-type ferroelectrics. An electric field-induced stable→metastable phase transition will produce a large strain associated with the crystal lattice rearrangement. However, in order to exploit the useful properties of the inter-ferroelectric transition, two special requirements must be satisfied: (1) the electric field-induced phase transition must be reversible to achieve hysteresis-free  $\epsilon$ - $E$  curve; and (2) the inter-ferroelectric transition must be induced by sufficiently small electric field to achieve good piezoelectric response at low field regime. In order to meet these conditions, special domain configuration and electric field direction are required. As shown by our simulation (Figs. 4-2 and 4-3), the crystallographically engineered domain configuration and non-polar electric field direction just satisfy these requirements. In this work, we considered  $\text{Pb}(\text{Zr}_{1-x}\text{Ti}_x)\text{O}_3$  in the

vicinity of morphotropic phase boundary. Figs. 4-2 and 4-3 show the [111] electric field-induced tetragonal→rhombohedral phase transition in domain wall region. Since the lead-free and lead-based perovskite-type ferroelectrics are characterized by the same Landau-Ginzburg-Devonshire polynomial with different material-specific expansion coefficients, our results also provide insight into the domain wall broadening mechanism in other systems. In particular, a [01] electric field-induced rhombic→rectangular transition is observed in BaTiO<sub>3</sub> in the vicinity of inter-ferroelectric transition temperature in a two-dimensional simulation, where rectangular phase nucleates at domain walls.<sup>15</sup>

Finally, it is noteworthy that there are evidences showing that engineered nanodomain configuration exhibits in Pb[(Zn<sub>1/3</sub>Nb<sub>2/3</sub>)<sub>1-x</sub>Ti<sub>x</sub>]O<sub>3</sub> and Pb[(Mg<sub>1/3</sub>Nb<sub>2/3</sub>)<sub>1-x</sub>Ti<sub>x</sub>]O<sub>3</sub> single crystals. Intrinsic lattice parameter relationships<sup>16,17</sup> and nanotwin diffraction analysis<sup>18</sup> show that the monoclinic M<sub>C</sub> phase in domain engineered Pb[(Zn<sub>1/3</sub>Nb<sub>2/3</sub>)<sub>1-x</sub>Ti<sub>x</sub>]O<sub>3</sub> and Pb[(Mg<sub>1/3</sub>Nb<sub>2/3</sub>)<sub>1-x</sub>Ti<sub>x</sub>]O<sub>3</sub> is tetragonal nanotwins. Recent TEM experiment directly observes tetragonal twins of average domain size about 10nm,<sup>20</sup> which appears to be M<sub>C</sub> phase in diffraction and polarized light microscopy. Therefore, the domain wall broadening mechanism and domain size effect could play a role at nanoscale and be responsible for the superior piezoelectric properties of these materials.



## IV.3. Engineering of Domain Configuration

In this section, computer modeling and simulation is performed to study the control mechanisms of domain configurations and sizes in crystallographically engineered ferroelectric single crystals. The simulations reveal that minimal domain sizes and highest domain wall densities are obtained with intermediate magnitude of electric field applied along non-polar axis of ferroelectric crystals, while lower and higher fields produce coarser domains and lower domain wall densities. It is shown that selection of polar domain variants by external electric field during nucleation of ferroelectric phase transition significantly affects the subsequent domain growth and coarsening kinetics and controls the formation and sizes of twin-related lamellar domains.

It has been shown in literature<sup>6,7</sup> that the enhanced properties can be achieved by controlling the domain microstructures, i.e., forming structural twined domain configurations. The domain wall broadening mechanism further suggests that twin-structured domain configurations in nanoscale can provide exceptional electromechanical properties under nonpolar electric fields. However, the domain sizes in crystallographically engineered ferroelectric crystals are very sensitive to the experimental conditions during sample treatment. Although sophisticated thermal and electrical processing with precise temperature and voltage control has been employed in experiments to engineer the domain configurations and sizes;<sup>7</sup> the underlying mechanisms are still not fully understood. Since it is hard for experimental research alone to systematically explore techniques of domain engineering, computer modeling and simulation are desired to gain insight as a supplemental tool. In this section, we perform

computer modeling and simulation to investigate the control mechanisms of domain configurations and sizes, with a focus on the effect of external electric field applied along the non-polar axis of single crystals during cooling across ferroelectric phase transition temperature (i.e., Curie temperature).

Our simulation reveals that, with on electric fields upon cooling, all polar domains will form with equal probabilities. Typical domain configurations consist of both 180° and 90° domain walls for ferroelectric single crystals of tetragonal composition, and 71° and 109° domain walls for rhombohedral composition, respectively. For MPB composition, the mosaic domain microstructures form. On the other hand, the simulation shows that, by applying electric fields along the non-polar directions upon cooling, the specific domains of favored orientations, as demonstrated for a tetragonal-phase single crystal by Fig. 4-4, can be selected to form structural twins. Three cases of forming twin-related domain microstructure when cooling ferroelectric single crystals across the Curie temperature by applying non-polar electric fields are observed in our simulation:

- (i). For rhombohedral-phase single crystal, the polar directions are along  $\langle 111 \rangle$  axes. If an electric field along [100] direction is applied, the rhombohedral twins of (100) twin plane form, shown in Fig. 4-5.
- (ii). For rhombohedral-phase single crystal again, under electric field along [110] direction, the rhombohedral twins of (110) twin plane form, shown in Fig. 4-6.
- (iii). For tetragonal-phase single crystal, the polar directions are along  $\langle 100 \rangle$  axes, if an electric field along [111] direction is applied, the tetragonal twins of (110) twin plane form, shown in Fig. 4-7.

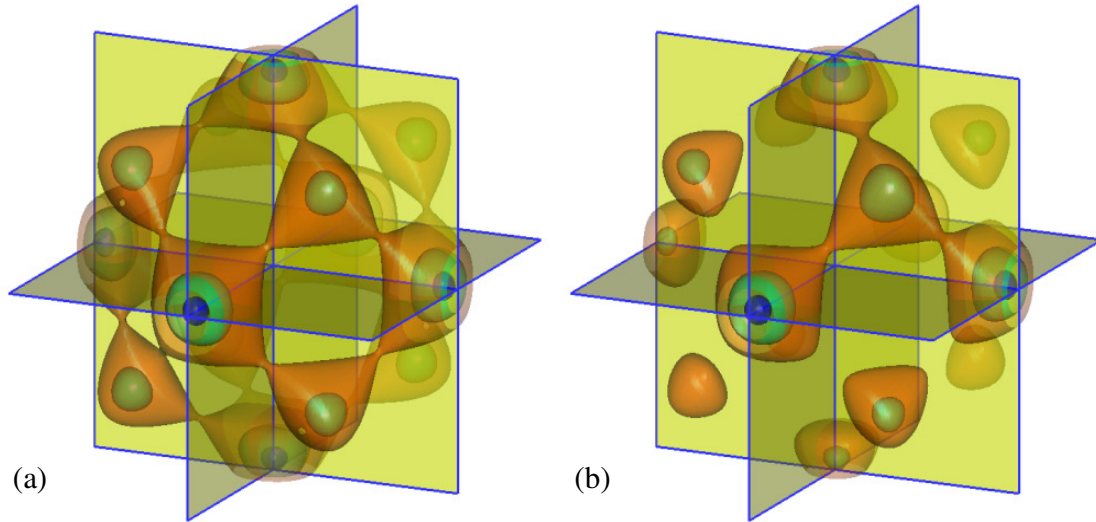


FIG. 4-4. Energy space of MPB-based ferroelectrics on tetragonal side (a) without and (b) with electric field applied along the nonpolar  $[111]$  direction. It is shown in (b) that the nonpolar electric field favors tetragonal variants of  $[100]$ ,  $[010]$  and  $[001]$ , which are able to form  $[110]$  structural twins.

It is shown in experiments<sup>7</sup> that the magnitudes of non-polar electric fields play an important role on controlling the domain sizes. Thus, it is desirable to systematically investigate the statistical effects of the magnitude of cooling electric fields on the formation of twin structures. This can be achieved by using large the computing size and counting the number of individual domains formed under non-polar electric fields. However, this method is strictly limited by the computing capability, and thus impractical. An alternative way is to rotate the coordinate system of the crystals by 45 degree about z axis (perpendicular to the paper plane), and use rectangle computing cells, i.e.,  $1024 \times 64$  and  $2048 \times 256$ , to simulate the formation of tetragonal twins of  $(110)$  plane under  $[111]$  electric field, as the shaded rectangle in Fig. 4-7. In the following part, we use the rotated computational cell and simulate the twin-related domain formation for PZT of tetragonal composition  $x=0.6$ .<sup>11,21,22</sup>

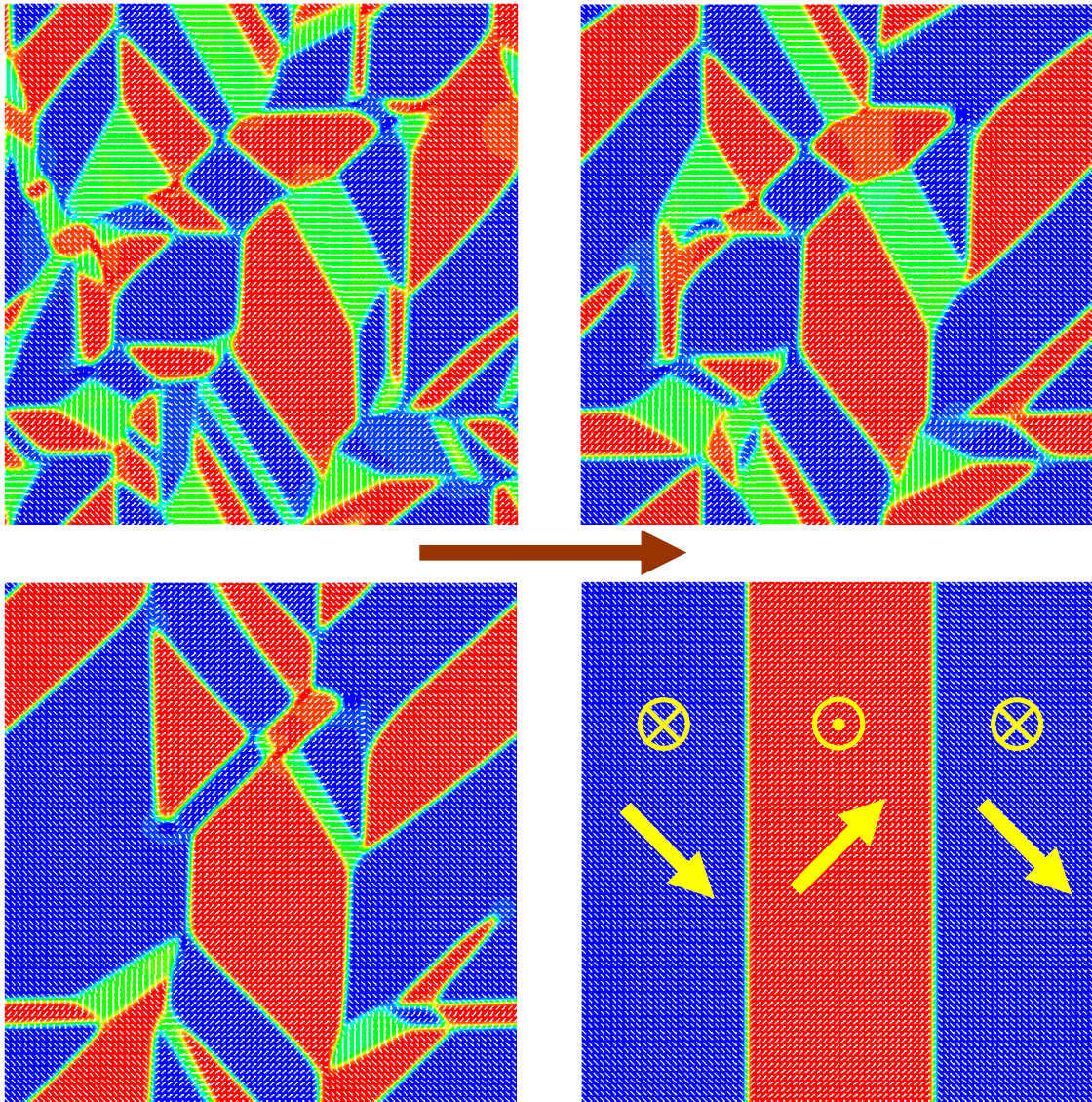


FIG. 4-5. Domain evolution and formation of (100) rhombohedral twins in MPB-based ferroelectric single crystal of rhombohedral composition cooling across Curie temperature with an electric field applied along the non-polar [100] direction. Small arrows in each snapshot represent in-plane components of polarization vector, and the out-of-plane component is represented by color, where green domains are tetragonal phase, and blue and red domains are rhombohedral phase. The brown arrow in the center represents the direction of applied electric field (non-polar [100] direction). Yellow arrows in the last figure represent the directions of polarization in individual domains, and symbols  $\otimes$  and  $\odot$  represent out-of-plane vector components.

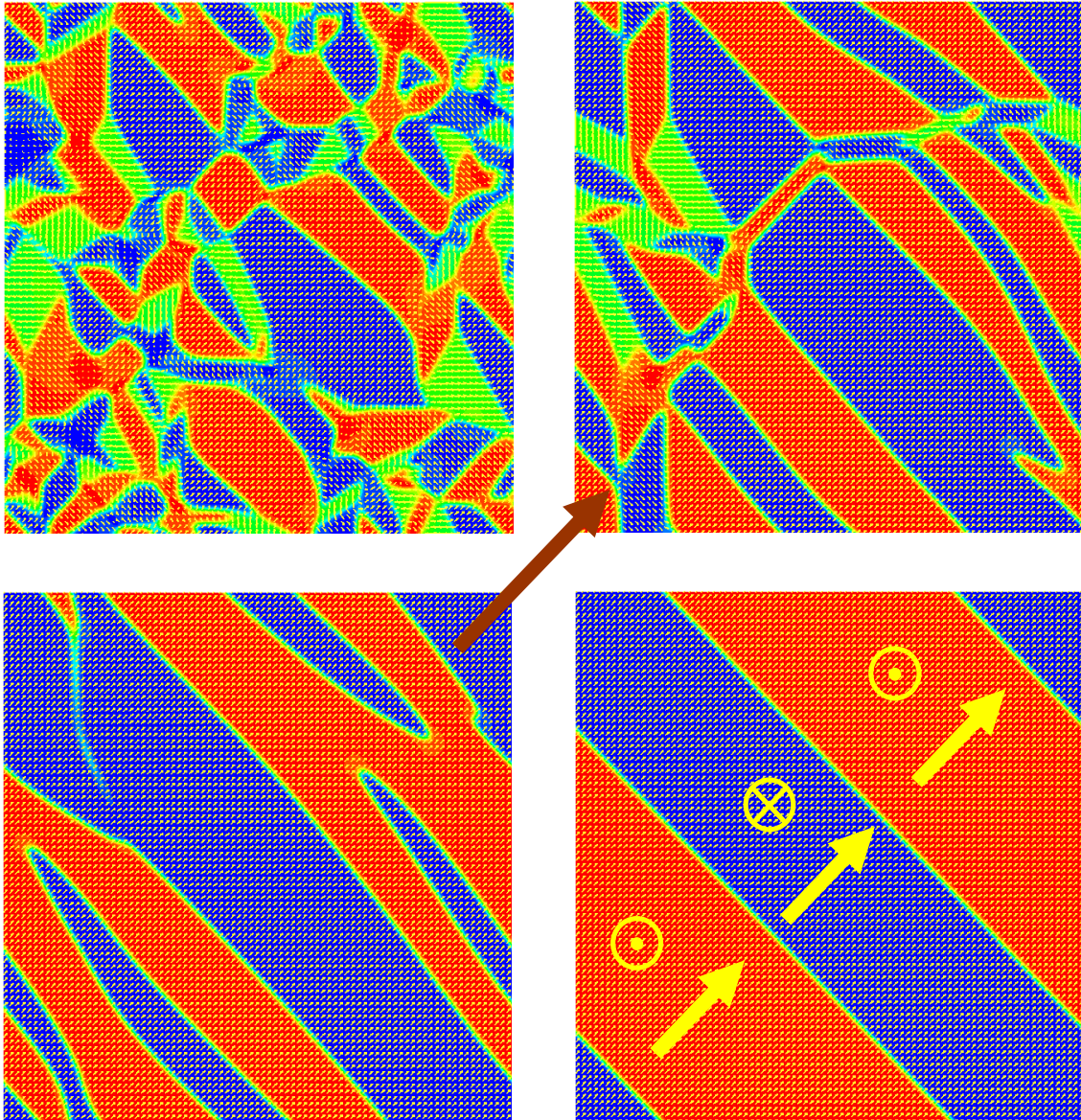


FIG. 4-6. Domain evolution and formation of (110) rhombohedral twins in MPB-based ferroelectric single crystal of rhombohedral composition cooling across Curie temperature with an electric field applied along the non-polar [110] direction. Small arrows in each snapshot represent in-plane components of polarization vector, and the out-of-plane component is represented by color, where green domains are tetragonal phase, and blue and red domains are rhombohedral phase. The brown arrow in the center represents the direction of applied electric field (non-polar [110] direction). Yellow arrows in the last figure represent the directions of polarization in individual domains, and symbols  $\otimes$  and  $\odot$  represent out-of-plane vector components.

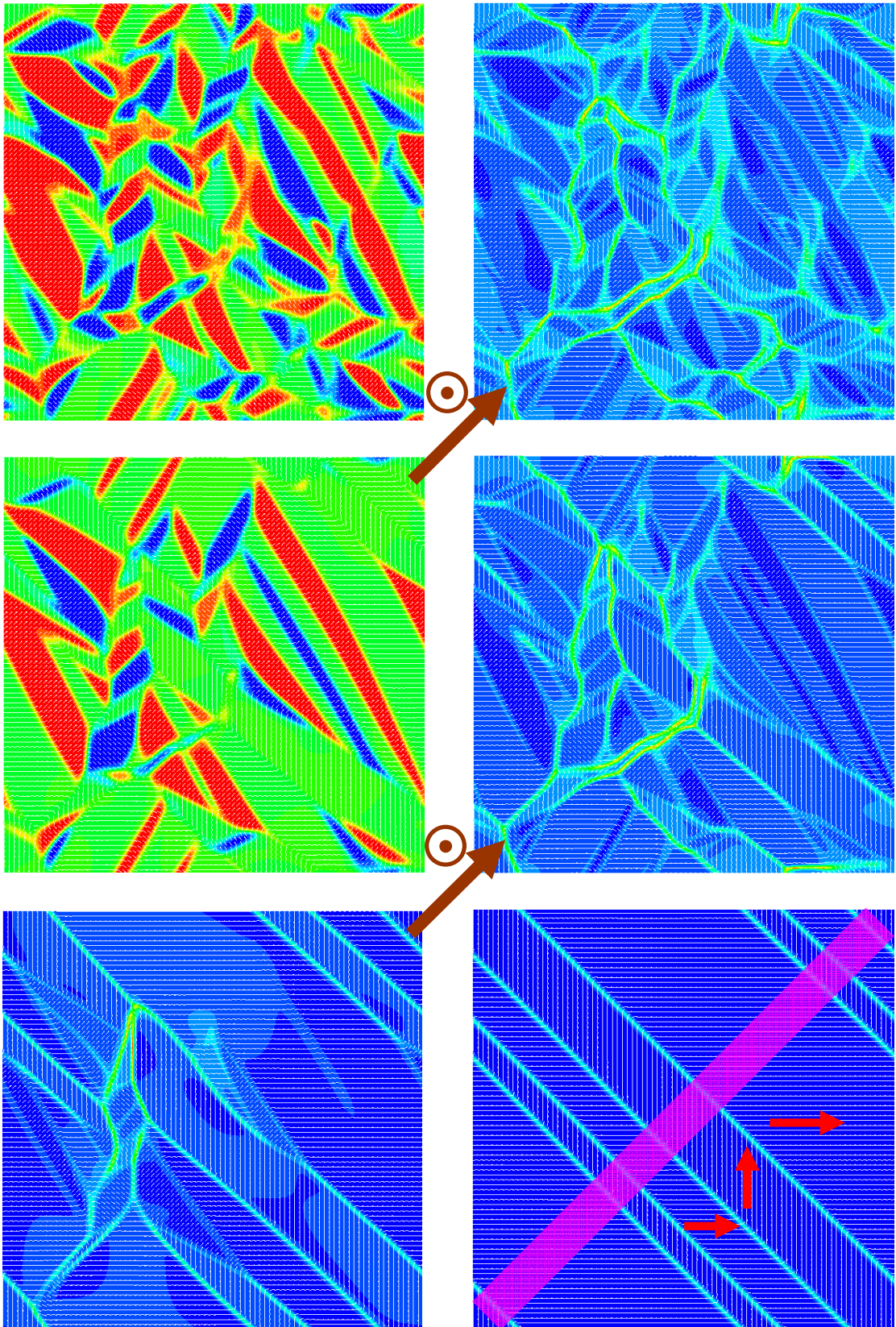


FIG. 4-7. Domain evolution and formation of (110) tetragonal twins in MPB-based ferroelectric single crystal of tetragonal composition cooling across Curie temperature with an electric field applied along the non-polar [111] direction. Two snapshots in the first row, as well as those in the second row, are essentially the same and visualized with different methods. Small arrows represent in-plane components of polarization vector. For the left snapshots of the first two rows, the out-of-plane component is represented by color, where green domains are tetragonal phase, and blue and red domains are rhombohedral phase. For snapshots on the right and in the bottom-row, the color shows the contour of the length of polarizations. The brown arrow and symbol  $\odot$  represent the direction of applied electric field (non-polar [111] direction). Red arrows in the last figure represent the directions of polarization in individual domains. It shows, after forming perfect structural twins, the polarizations are almost the same in every individual domain, and only vary at domain walls (shown by thick lines). Shaded rectangular region in the last figure demonstrates the typical domain microstructures gained from the 45 degree rotated simulation.

Computer simulation reveals that, without applying electric fields, random domain configurations with all possible tetragonal variants form for PZT single crystals of tetragonal composition. Under non-polar [111] electric field, tetragonal variants of [-100] and [0-10] become less favored. However, at low field strengths, it is still possible for them to nucleate and form domains, leading to complex domain patterns comprising of both 180° and 90° domain walls. These patterns are stable until the strength of non-polar electric field reaches certain threshold (activation strength,  $E_a$ ). Above this threshold, tetragonal variants of [100] and [010] become much more favored than of [-100] and [0-10], and thus are selected out to form [110] tetragonal twins, as the shaded rectangle in Fig. 4-8. If further increasing the strength of [111] electric field to certain value (stretch

strength,  $E_s$ ), the otherwise metastable rhombohedral variant of [111] becomes kinetically more favored, thus is selected out to form single-domain microstructure.

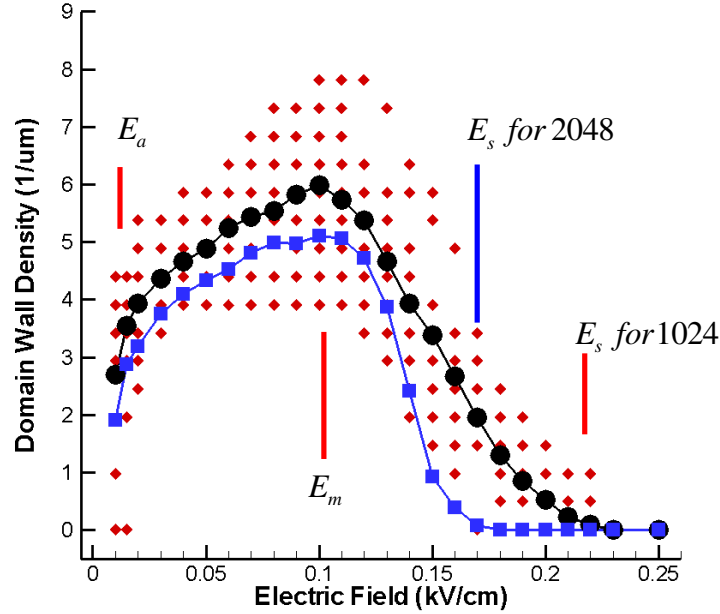


FIG. 4-8. The dependence of average domain size (domain wall density) on the magnitude of electric field applied along non-polar [111] direction at room temperature. Red diamonds represent individual simulation results for computational grids of 1024 by 64, black circles represent average results. For comparison, the average results for computational grids of 2048 by 128 are also shown in blue squares. The approximated activation strength ( $E_a$ ), strength for maximum density ( $E_m$ ), and stretch strength ( $E_s$ ) are indicated by lines.

It shows that selection of domain variants by external electric field during nucleation of ferroelectric phase transition significantly affects the subsequent domain growth and coarsening kinetics and controls the formation and sizes of twin-related lamellar domains. As shown in Fig. 4-8, our statistical simulation suggests that, with increasing the strength of applied non-polar [111] electric field, the domain walls density first increases and then decreases, the maximum values appears at an intermediate strength ( $E_m$ ).



The evolution of domain microstructure can be better understood by considering the energy difference of possible variants/phases versus the lengths of polarization calculated from the LGD polynomials,<sup>21</sup> as shown in Fig. 4-9. It is shown that if the strength of externally applied non-polar [111] electric field is just above the activation strength ( $E \sim E_a$ ), the energy difference among the metastable and stable variants/phases is very small at the very beginning of the nucleation stage, and thus the possibilities of nucleating those variants/phases are nearly equal. Since with the polarization growing, the energies associated with rhombohedral variants increases very fast, as demonstrated by the [111] rhombohedral variant in Fig. 4-9, the nucleated rhombohedral embryos will quickly transform to tetragonal variants at almost equal probabilities. With further growth of the polarization, the energy difference among metastable and stable tetragonal variants become large, thus, the metastable variants of [-100] and [0-10] are finally consumed by the stable variants of [100] and [010]. If increasing the strength of applied electric field ( $E_a < E < E_m$ ), the evolution of domain microstructure is similar, except nucleating more rhombohedral embryos at the beginning. However, due to bigger energy difference among the metastable and stable tetragonal variants at higher non-polar electric field, the possibilities of individually nucleating domains of stable variants are getting bigger. Once nucleated, those stable domains will grow by consuming the metastable ones: either merge together or form tetragonal structural twins, depending on the type of variants separately nucleated in the adjacent domains. Thus, higher chance of individually nucleating domains of stable variants leads to higher chance of forming structural twins, which explains the trend of increasing domain wall density with increasing the strength of applied electric field for  $E_a < E < E_m$ .

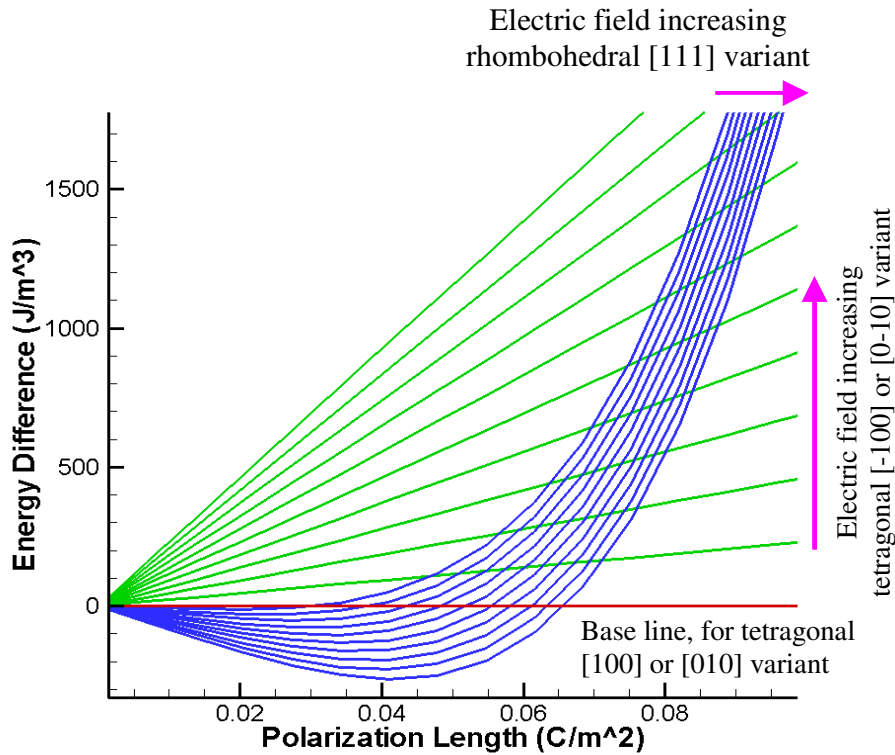


FIG. 4-9. The effects of non-polar [111] electric field on energy difference for different variants versus the polarization length for PZT of tetragonal composition  $x = 0.6$  (calculated from ref.21). The energies associated with all possible variants under different strengths of non-polar [111] electric field are calculated for different lengths of the polarization, the resulted energies then subtract that of tetragonal [100] variant, and the difference is plotted. Where red line is for the energy difference of [100] or [010] variant (always zero because of equal energy states under the non-polar electric field), green lines are for the energy difference between [-100] and [100] (or [0-10] and [100]) tetragonal variants, and blue lines are for the energy difference between rhombohedral [111] variant and tetragonal [100] variant. Those lines, in green and in blue, are plotted for increasing strengths of non-polar electric field. The strength increasing is indicated by arrows and at a pace of 0.02 kV/cm, e.g. the first and second lines are under 0.02 and 0.04 kV/cm, respectively. It shows that, at the very beginning of growing new variants, with increasing the strength of electric field applied along non-polar [111] direction, the relative energy of rhombohedral [111] variant is getting lower, and that of tetragonal [-100] and [0-10] variants are getting higher.

For cases of  $E > E_m$ , the evolution of polar domains takes different kinetic pathways. It is shown in Fig. 4-9 that for  $E > E_m$ , [111] rhombohedral variant is in much lower energy state during the beginning of nucleation, leading to a large amount of embryos of [111] rhombohedral nucleated. These rhombohedral embryos may percolate to form fully developed rhombohedral domains, which will be consumed by tetragonal variants later through domain wall motions. Thus, the chance of individually nucleating stable domains (of either [100] or [010] variant) decreases. As a result, the chance of forming twin walls decreases from the value at  $E = E_m$ , explaining the second part of the trend shown in Fig. 4-8.

The idea of higher chance of individually nucleating stable domains leading to higher chance of forming structural twins is supported by the simulation of offset initials, as shown in Fig. 4-10. A small positive constant is artificially added to all three components of the initial random polarization at each computational grid, and a small non-polar electric field (just above  $E_a$ ) is applied. Fig. 4-10 plots the resulted domain wall density versus the amount of offset. Clearly, the trend shown in this figure is similar to that in Fig. 4-8: with increasing the amount of offset, the domain wall density first increases then decreases. Since the applied non-polar electric field is too low to noticeably change the energy difference among different variants/phases, the amount of offset is responsible for the trend shown in Fig. 4-10. It is straightforward that the amount of offset directly affects the possibilities of nucleating variants: more tetragonal variants of [100] and [010] will be nucleated for intermediate offset, and a large amount of rhombohedral [111] variant will be nucleated for big offset. Thus, it is the chance of nucleating tetragonal

variants of [100] and [010] that determines the formation of structural tetragonal twins of (110) twin plane, and the domain wall density.

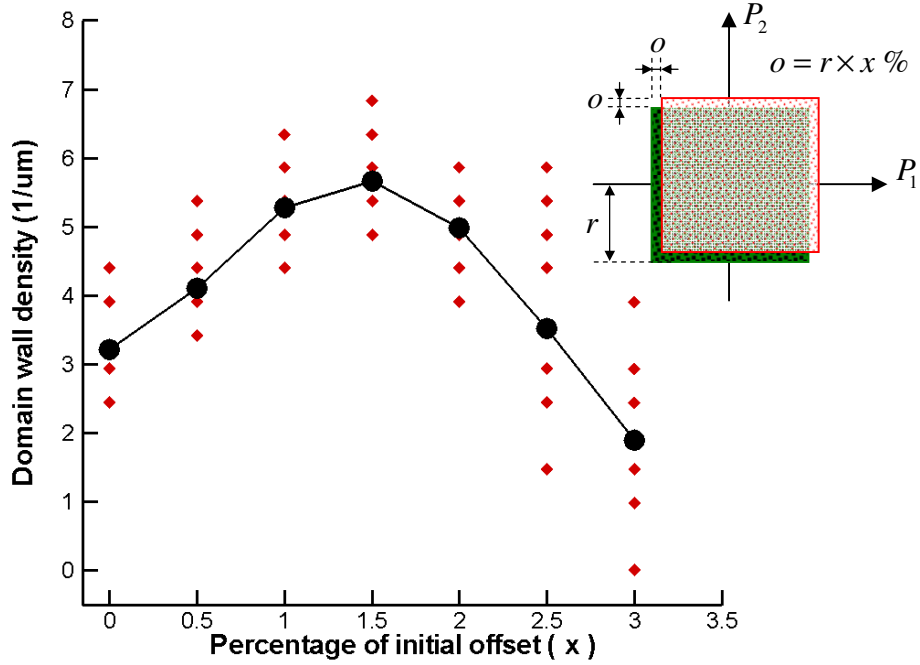


FIG. 4-10. The dependence of average domain size (domain wall density) on the percentage of initial offset under a small non-polar [111] electric field ( $\sim E_a$ ). Red diamonds represent individual simulation results, black circles represent average results. The percentage of initial offset is defined by the figure on the upper right. The initial polarization without offset can randomly have any value (a combination of  $P_1$ ,  $P_2$  and  $P_3$ , where  $P_3$  is not shown for clarity) from the green box of  $2r$  in length. The offset initial polarization is randomly selected from the red box of the same length, but with the center shifted in three components by  $o = r \times x \%$ , where  $x$  is the abscissa shown in this figure.

It is noteworthy that, while our simulation does show the domain wall density is increased by applying an intermediate non-polar [111] electric field, the enhanced domain wall density, comparing to that for  $E \sim E_a$ , is much lower than the value reported in literature (enhanced by about 10 times through sophisticated thermal-electric

treatments).<sup>7</sup> This discrepancy can be attributed to the fact that our simulation does not consider temperature effects on the domain wall density. Our further simulation on cooling across Curie temperature to 250°C, rather than to room temperature, does show that the overall domain wall density is systematically increased, with the maximum density also obtained under intermediate magnitude of electric field applied along non-polar axis, as shown in Fig. 4-11.

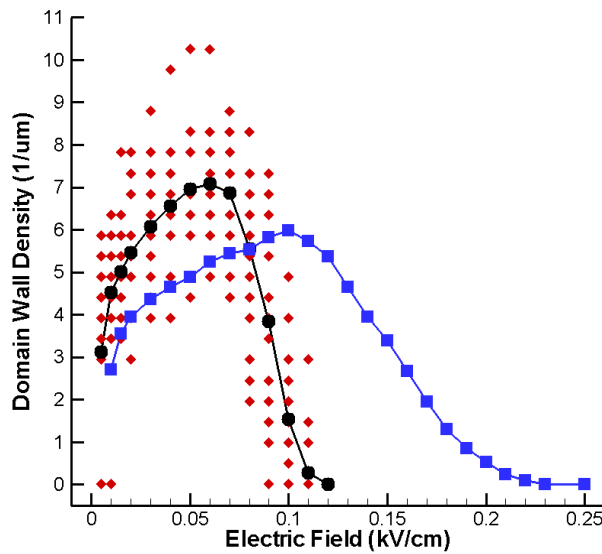


FIG. 4-11. The dependence of average domain size (domain wall density) on the magnitude of electric field applied along non-polar [111] direction at 250°C. Red diamonds and black circles represent individual and average results for computational grids of 1024×64, respectively. For comparison, the average results for 1024×64 at room temperature are also depicted. It is clear that all characteristic field strengths are lower, and the domain wall densities of the increasing branch are systematically higher at elevated temperature (250°C).

## IV.4. Stabilization of Domain Microstructure

In this section, computer modeling and simulation is performed to study the domain stabilization effect due to short-range ordering of charged point defects in aged ferroelectrics. Phase field model takes into account various energetic contributions involved in domain aging phenomenon, including chemical, domain wall, electrostatic and elastostatic energies, as well as domain-dependent internal electric field associated with the short-range ordering of charged point defects. The internal electric field strength is estimated by the computer simulation. Clausius-Clapeyron-type thermodynamic analysis of field-induced ferroelectric phase transition is used to evaluate aging-produced internal field strength from relevant experimental data, which is in agreement with the computer simulation.

It is suggested by the domain wall broadening mechanism<sup>1</sup> and domain size effects<sup>6,7</sup> that twin-structured domain microstructures are optimized configuration and can provide exceptional electromechanical properties under non-polar electric fields. It is also demonstrated in previous section that the domain configurations and domain sizes can be controlled by applying an external electric field along non-polar direction. However, the engineered domain configurations are very fragile if the applied electric fields are deviated from specific directions where every variant is energetic equivalent. Moreover, once the optimized domain microstructures evolve into other configurations, it will be hard to recover them. Thus it is desirable to find ways to stabilize the optimized domain configurations, or, make the engineered domain patterns stay at the optimized states when experiencing mechanical, thermal and/or electrical fluctuations and transform back to the

engineered states once the shortly applied external fields are removed. In this section, we perform computer modeling and simulation to investigate the aging-stabilization effects of ferroelectric domains, with a focus on the internal bias electric field associated with the short-range ordering of charged point defects. We also perform thermodynamic analysis to derive a Clausius-Clapeyron-type equation and predict the magnitude of aging-produced internal bias electric field.

It is reported in literature<sup>12,23</sup> that the symmetry of short-range order of point defects in crystals follows the crystal symmetry when in equilibrium, and the symmetry-conforming properties can lead to “aging-induced microstructure memory”. This general symmetry conforming property of point defects was applied in several ferroelectric systems and large recoverable nonlinear electric-field-induced strains were reported.<sup>12</sup> It is suggested<sup>12,23</sup> that the aging process of crystals with point defects can be viewed as an ion redistribution process, and the broken balance of local charge just makes local unit cells like dipoles, which follow the local symmetry of the ferroelectric phases and form internal electric fields.

Therefore, for an aged ferroelectric sample with domain microstructure described by polarization field  $\mathbf{P}^0(\mathbf{r})$ , the short-range ordering of charged point defects generates an effective internal bias electric field  $\mathbf{E}^0(\mathbf{r})$  that is spatially heterogeneous and depends on the domain microstructure, i.e.,  $\mathbf{E}^0(\mathbf{r})$  is aligned with  $\mathbf{P}^0(\mathbf{r})$  in individual domains.<sup>12</sup> For convenience, we write  $\mathbf{E}^0(\mathbf{r}) = \kappa \epsilon_0^{-1} \mathbf{P}^0(\mathbf{r})$ , where  $\epsilon_0$  is the permittivity of free space, and  $\kappa$  a constant characterizing the internal field strength. We incorporate this internal bias field into the model described in chapter 2, and perform the computer simulation for tetragonal PZT of composition  $x=0.6$ .<sup>11, 21, 22</sup>

The computer simulation shows that domain microstructures are stabilized in sufficiently aged ferroelectric samples, where the original, aged domain configurations are automatically recovered from arbitrarily deviated states, as shown in Fig. 4-12. The restoring force to such domain stabilization and recovery behaviors is the internal bias electric field associated with the short-range ordering of charged point defects. The degree of short-range ordering and, thus, strength of the internal field is characterized by the parameter  $\kappa$ . In an aged sample, the short-range ordering is maintained during a diffusionless process, such as domain switching driven by a short-period external electric field<sup>12</sup> or phase transformation during rapid heating-cooling cycle.<sup>23</sup>

To investigate domain stabilization and recovery phenomena, we consider a rapid heating-cooling cycle during which an aged multi-domain ferroelectric sample transforms first to paraelectric phase and then back to ferroelectric phase. Since the sample stays in paraelectric state only for a short period, diffusion of point defects does not have sufficient time to alter their short-range ordering, as experimentally observed;<sup>12</sup> upon transforming back to ferroelectric phase, the sample tends to form the same domain microstructure as in the aged state to minimize total system free energy. Figure 4-12(f) shows an aged lamellar domain microstructure representative of engineered domain configurations, where the short-range ordering of charged point defects and the associated internal bias field conform to the polarization distribution. Figures 4-12(a)-(f) show the simulated domain recovery process in a sufficiently aged sample ( $E^0 \approx 1.0$  kV/cm, or  $\kappa \approx 1.5 \times 10^{-6}$ , corresponding to red regions on Fig. 4-14) upon cooling across Curie temperature (i.e., transforming back to ferroelectric phase after rapid heating) under the effect of internal bias field: Fig. 4-12(a) shows an arbitrary polarization distribution at



the initial stage of cooling-induced ferroelectric phase transformation under the effect of thermal noise, and Figs. 4-12(b)-(f) show the evolution of a random initial to the fully recovered domain microstructure that turns out to be identical to the original, aged domain configuration (Fig. 4-12(f) is shown as both the original and recovered domain configurations).

For comparison, a similar heating-cooling cycle is also simulated for an insufficiently aged sample, and a very different domain microstructure is formed, as shown in Fig. 4-13 ( $E^0 \approx 0.05$  kV/cm, or  $\kappa \approx 7.5 \times 10^{-8}$ , corresponding to blue regions on Fig. 4-14), which is typical of multi-domain ferroelectric states consisting of both  $90^\circ$  and  $180^\circ$  domain walls. The lack of domain stabilization and recovery effects in such an insufficiently aged sample is expected because the charged point defects only form weak short-range ordering, thus, restoring force is not strong enough to recover the domain microstructure.

In order to determine the critical strength of internal bias field required for domain recovery in aged ferroelectrics, statistical simulations are performed with different initials and parameter  $\kappa$ , as shown in Fig. 4-14. It is found that when internal bias field is much greater than about 0.45kV/cm (or, red regions on Fig. 4-14), domain configurations are immediately fully recovered after the heating-cooling cycles, as shown in Fig. 4-12. A case of smaller internal field is also plotted in Fig. 4-15 ( $E^0 \approx 0.42$  kV/cm, or  $\kappa \approx 6.3 \times 10^{-7}$ , corresponding to the boundaries between red and green regions on Fig. 4-14). The comparison between Figs. 4-12 and 4-15 shows that, domains nucleate with polarization aligned with local bias field (conforming to the symmetry of short-range ordering), and higher strength of internal field leads to better alignment of nucleated polarization and faster recovery of the domain microstructures.

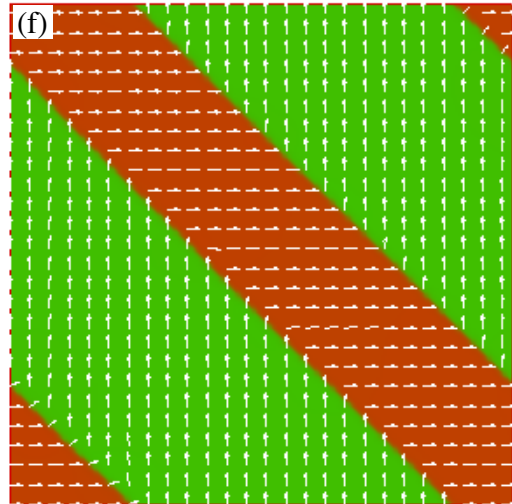
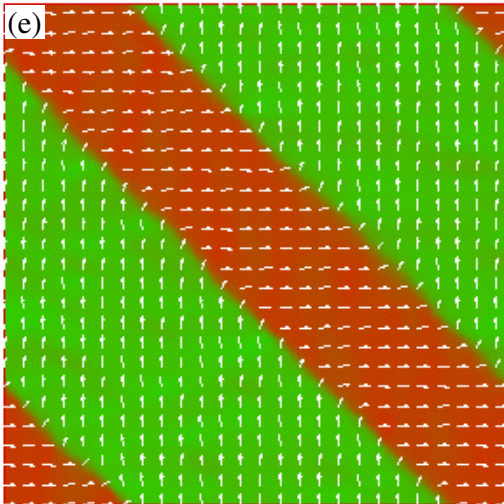
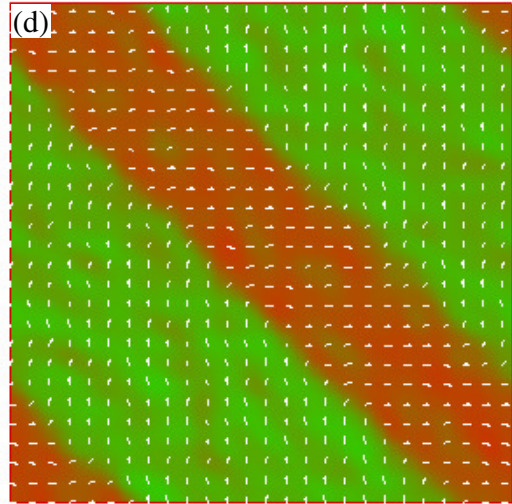
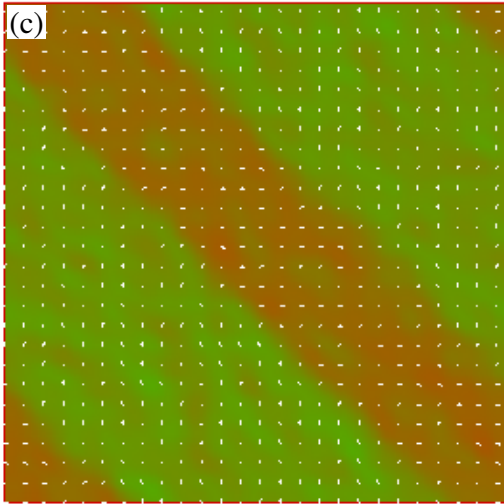
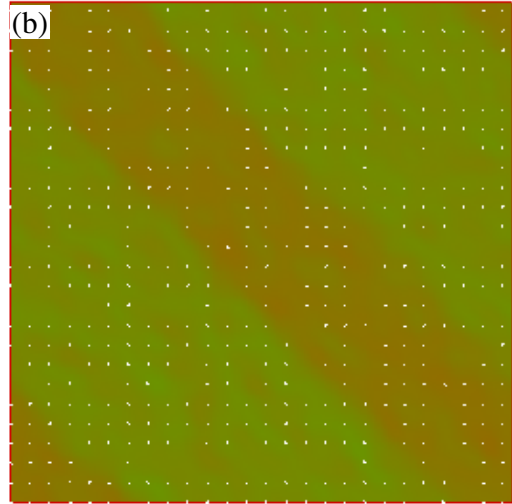
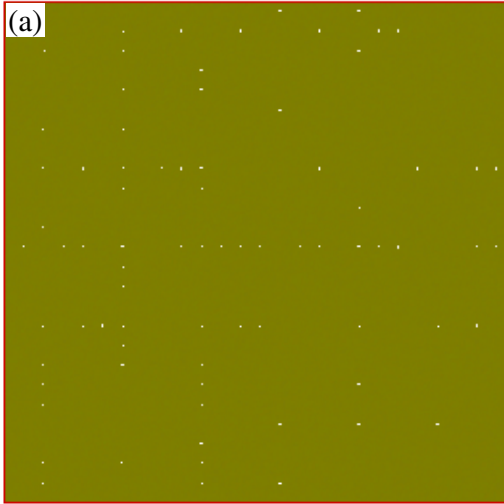


FIG. 4-12. Domain stabilization and recovery behaviors of an aged tetragonal PZT of composition  $x=0.6$  during a rapid heating-cooling cycle. The internal bias electric field is about 1.0 kV/cm. (a) is an arbitrary polarization distribution at the initial stage of cooling process, (b)–(f) demonstrates the process of restoring the original, aged domain configuration (corresponding to simulation time  $t=2, 2.4, 2.8, 3.2, 4$ , respectively). Since the resulted domain microstructure is identical to the original one, (f) also represents the original, aged domain microstructure. Arrows represent the in-plane polarization components. A mapping between components of polarization ( $P_x, P_y, P_z$ ) and color elements (red, green and blue) is employed to represent the polarization states, and thus the polar domains in light color are close to those in the same deep color. It is shown that the nucleation and growth of polar domain are strongly affected by internal bias field associated with the short-range ordering of charged point defects, and the restoring process is fast.

On the other hand, with internal field weaker than about 0.07kV/cm, domain recovery is not guaranteed. The presence of such a weak bias field is not able to generate sufficient driving force for resembling the original domain states from the beginning, thus, the resultant domain microstructure depends on the kinetic pathway of evolving high temperature random initial. If a domain pattern very different to the original one is kinetically favored, the domain microstructure may evolve as if there is not internal field, as demonstrated in in Fig. 4-13. If a domain pattern similar to the original one is favored, and the internal field is not negligible, a slow process of domain wall motions might be followed to recover the original configuration, as demonstrated in Fig. 4-16 ( $E^0 \approx 0.065$  kV/cm, or  $\kappa \approx 9.75 \times 10^{-8}$ , corresponding to green regions on Fig. 4-14). This restoring process, generating similar domain configurations and then moving domain walls to fully recover, is always observed with intermediate internal bias field, no matter whether it is kinetically favored or not, as shown by the green regions on Fig. 4-14.

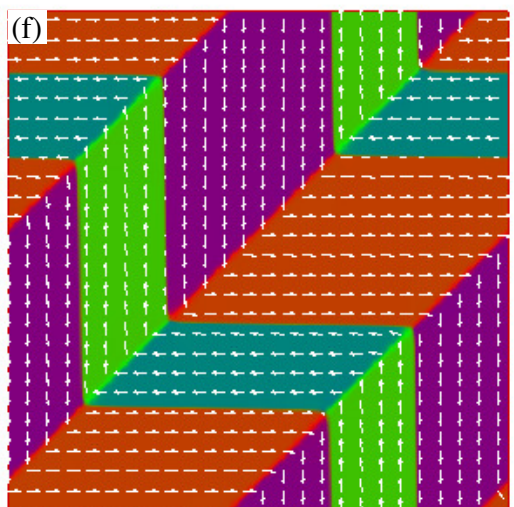
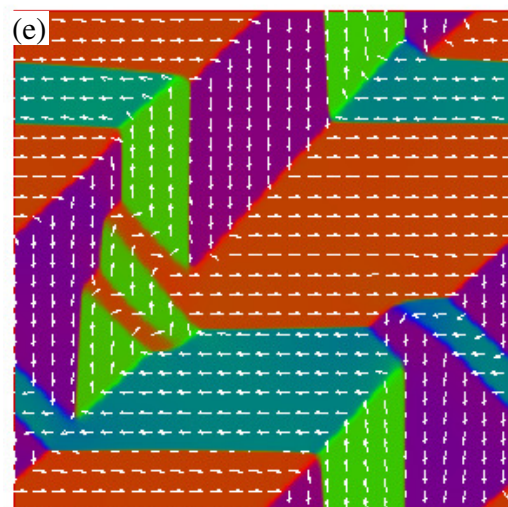
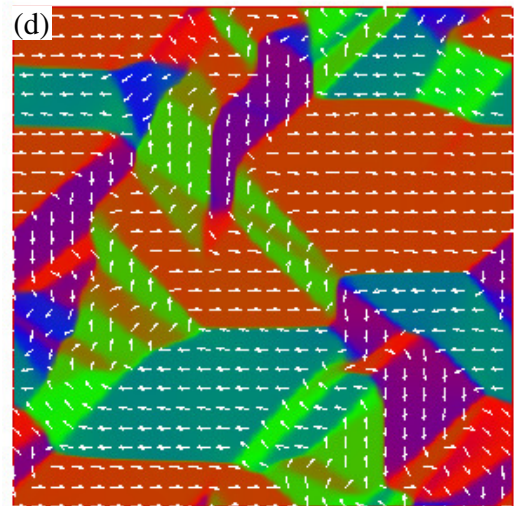
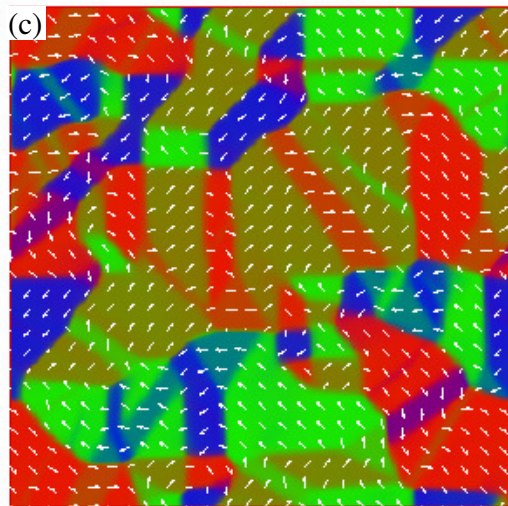
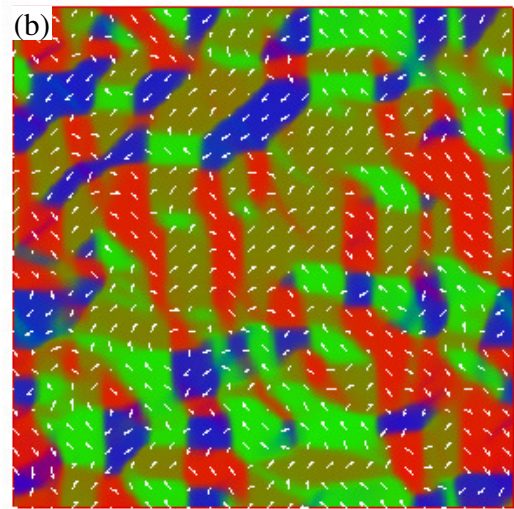
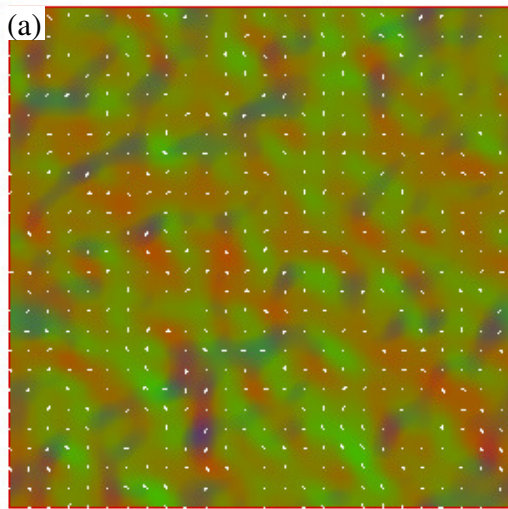


FIG. 4-13. Random domain evolution of an insufficiently aged tetragonal PZT of composition  $x=0.6$  during a rapid heating-cooling cycle. The internal bias electric field is about 0.05 kV/cm. (a)–(f) demonstrates the process of evolving to a pattern different to the original, aged domain configuration (corresponding to simulation time  $t=3, 6, 21, 36, 96,$  and  $300,$  respectively). It is shown that, with a relatively weak internal field, the nucleation and growth of polar domain are dependent on the initial: if unfavorable domain pattern is resulted, the internal field will not be able to restore the aged domain configuration.

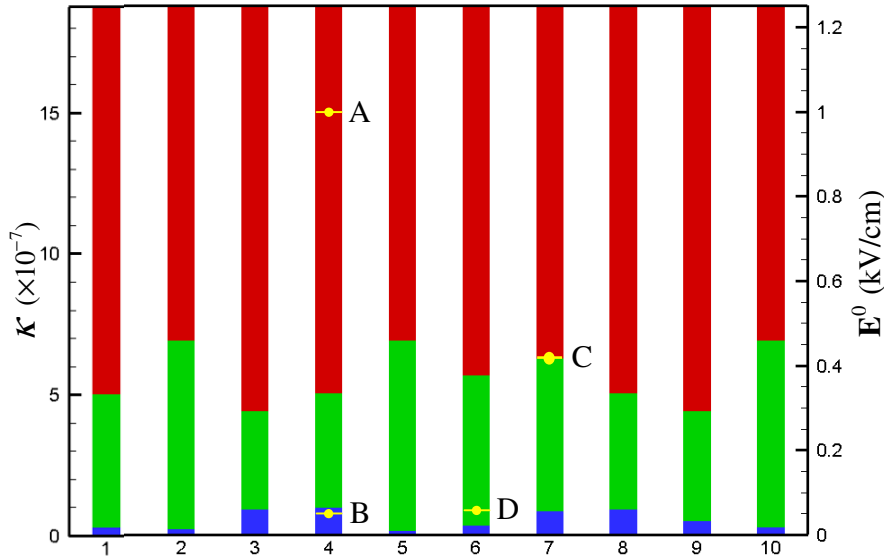


FIG. 4-14. Statistical results on the domain microstructure recovery of 10 aged tetragonal PZT samples of composition  $x=0.6$  during a rapid heating-cooling cycle. The internal bias electric fields are systematically varied, and three different domain processes are identified for each series, as shown by color on bars: red regions are for immediate recovery of the domain microstructure under relatively large internal field, green regions are for domain configuration recovery involving a slow process of domain wall motions with intermediate internal field, blue regions are for the cases of weak internal field, where the domain microstructures do not recover. The simulation cases shown in Figs. 4-12, 4-13, 4-15, and 4-16 are marked on the bars as A, B, C, and D, respectively.

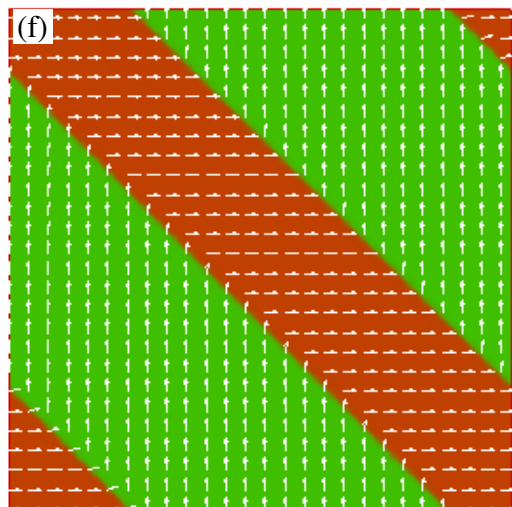
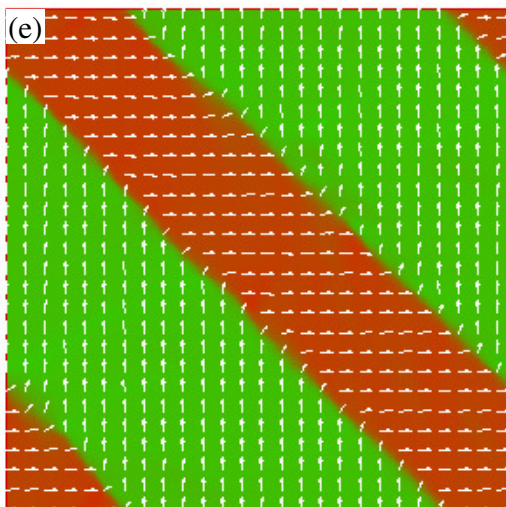
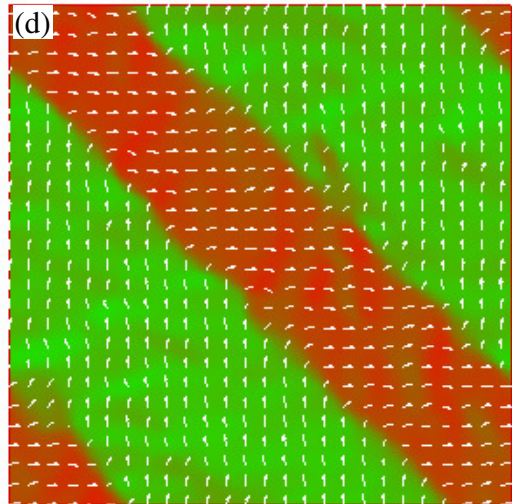
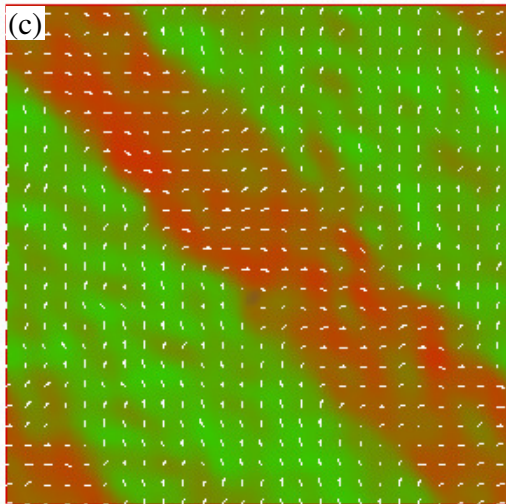
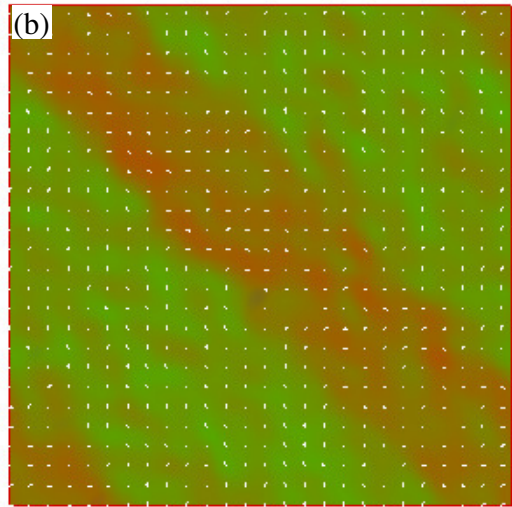
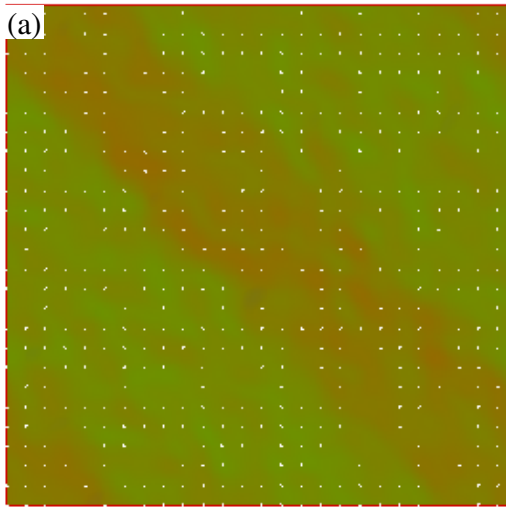


FIG. 4-15. Domain stabilization and recovery behaviors of an aged tetragonal PZT of composition  $x=0.6$  during a rapid heating-cooling cycle. The internal bias electric field is about 0.42 kV/cm. (a)–(f) demonstrates the process of restoring the original, aged domain configuration (corresponding to simulation time  $t=2.4, 2.8, 3.2, 3.6, 4.0,$  and  $6.0,$  respectively).

It is interesting to note in Fig. 4-16 that, though most parts of the matured polar domains align along the original ones, nucleating and growing polar domains of unfavorable orientations are still possible. If no internal field presented, the resultant domain microstructure, Fig. 4-16(d), is stable. It is the presence of internal field that makes the misaligned domains shrink to fully recover the original domain microstructure, as shown in Figs. 4-16(d)-(f), and strength of the internal field that determines the speed of the motions of domain walls.

It is noteworthy that charged point defects are usually introduced by doping, which effectively reduces domain wall mobility, as in hard PZT. Friction to domain wall motion due to point defects is not considered in the simulation, thus above intermediate internal field strength should be insufficient for complete domain recovery in real ferroelectric samples, and the estimated critical field strength of 0.5kV/cm should be taken as a lower limit.

To compare our simulation with experiment, we also evaluate the internal bias electric field strength from relevant experimental data. Based on the fact that aging-generated internal electric field produces the same effect in individual ferroelectric domains as an externally applied electric field does in electric field-induced ferroelectric phase transformation, it is expected that the Curie temperature increases with the internal field strength in aged samples ( i.e., degree of aging and short-range ordering of charged

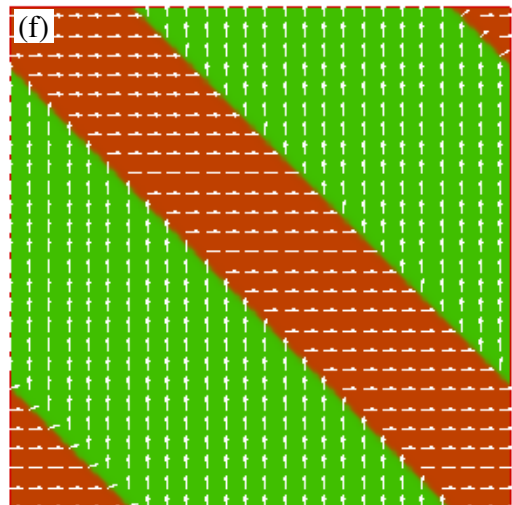
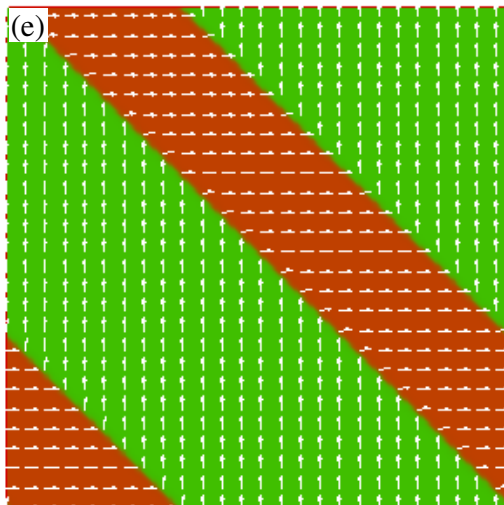
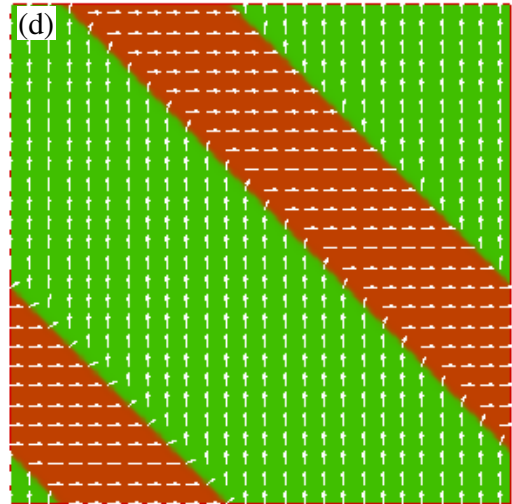
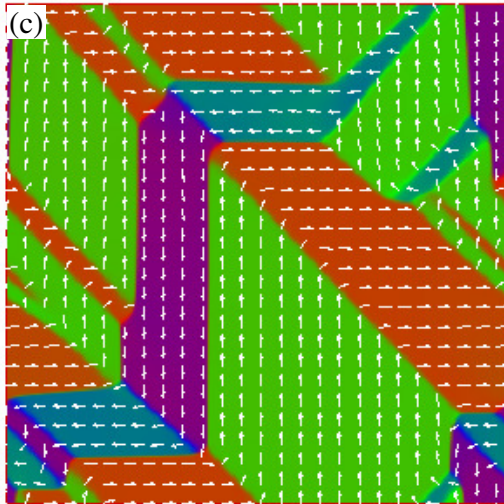
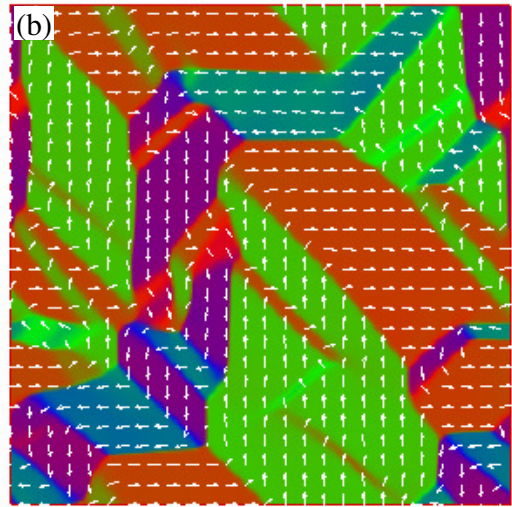
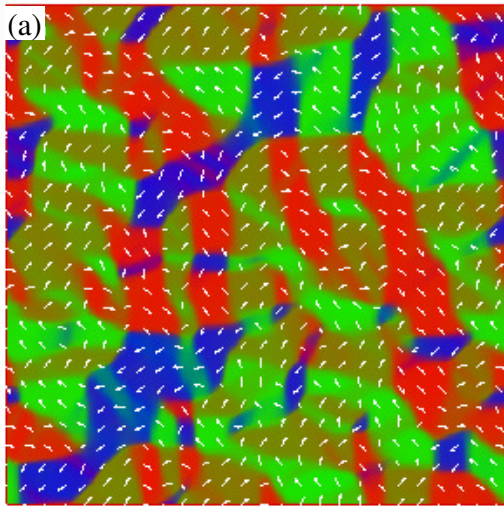




FIG. 4-16. Domain stabilization and recovery behaviors of an aged tetragonal PZT of composition  $x=0.6$  during a rapid heating-cooling cycle. The internal bias electric field is about 0.065 kV/cm. (a)–(f) demonstrates the process of restoring the original, aged domain configuration (corresponding to simulation time  $t=6, 20, 40, 160, 30000,$  and  $100000,$  respectively). (d) is a domain pattern similar to the original, aged one, and (d)–(f) demonstrate a very slow process of domain wall motion, as suggested by the corresponding simulation time.

point defects). Such a phenomenon is, indeed, experimentally observed in  $\text{BaTiO}_3$ .<sup>13</sup> Therefore, the internal bias field strength can be evaluated from the Curie temperature change of aged samples. Considering the equality of Gibbs free energy  $G=H-TS$  between paraelectric and ferroelectric phases at Curie temperature  $T_C$  under zero electric field, and their equal free energy change  $dG=-SdT-PdE$  under nonzero electric field (assuming constant pressure), thermodynamic analysis gives a Clausius-Clapeyron-type equation:

$$\frac{dT}{dE} = \frac{\Delta P}{\Delta S}, \quad (27)$$

where  $\Delta P=P_{\text{ferro}}-P_{\text{para}}=P_s(T_C)$  is equal to the spontaneous polarization at Curie temperature  $T_C$ , and  $\Delta S$  is the entropy change of ferroelectric phase transition. Using  $\Delta P=0.18\text{C/m}^2$  and  $\Delta S=13.5\text{kJ}/(\text{m}^3\cdot\text{K})$  reported for  $\text{BaTiO}_3$ ,<sup>24,25</sup> we obtain  $dT/dE=1.33\times 10^{-5}\text{C}\cdot\text{m}\cdot\text{K}/\text{J}$ . Experiments observe a Curie temperature change of 2K in fully aged samples,<sup>13</sup> thus the internal electric field is evaluated to be 1.5kV/cm. It is worth noting that this experimentally evaluated value in the fully aged samples should be higher than the critical value estimated from computer simulations. Therefore, simulation and experiment are in agreement and the aging-produced internal bias field in sufficiently aged ferroelectric samples is of the order of magnitude of 1kV/cm.

## IV.5. References

1. W.F. Rao and Y.U. Wang, *Appl. Phys. Lett.* **90**, 041915 (2007).
2. W.F. Rao, K.W. Xiao, and Y.U. Wang, “ *Control of Domain Configurations and Sizes in Crystallographically Engineered Ferroelectric Single Crystals: Phase Field Modeling and Simulation*” (to be published).
3. W.F. Rao, T.L. Cheng, and Y.U. Wang, “ *Aging-Stabilization of Ferroelectric Domains through Short-Range Ordering of Charged Point Defects: Phase Field Modeling and Clausius-Clapeyron Analysis* ” (to be published).
4. S. E. Park and T. R. Shrout, *J. Appl. Phys.* **82**, 1804 (1997).
5. S. E. Park, S. Wada, L. E. Cross, and T. R. Shrout, *J. Appl. Phys.* **86**, 2746 (1999).
6. S. Wada, K. Muraoka, H. Kakemoto, T. Tsurumi, and H. Kumagai, *Jpn. J. Appl. Phys.*, Part 1 **43**, 6692 (2004).
7. S. Wada, K. Yako, H. Kakemoto, T. Tsurumi, and T. Kiguchi, *J. Appl. Phys.* **98**, 014109 (2005).
8. X. Du, U. Belegundu, and K. Uchino, *Jpn. J. Appl. Phys.* **36**, 5580 (1997).
9. X. Du, J. Zheng, U. Belegundu, and K. Uchino, *Appl. Phys. Lett.* **72**, 2421 (1998).
10. D. Damjanovic, *J. Am. Ceram. Soc.* **88**, 2663 (2005).
11. W.F. Rao and Y.U. Wang, “*Intrinsic Electrostrictive and Piezoelectric Properties of Lead Zirconate Titanate (PZT): Analysis of Diffraction Data*” (to be published).
12. X. Ren, *Nature Mater.* **3**, 91 (2004).
13. D. Sun, X. Ren, and K. Otsuka, *Appl. Phys. Lett.* **87**, 142903 (2005).
14. S. F. Liu, S. E. Park, H. Lei, L. E. Cross, and T. R. Shrout, *Ferroelectrics* **221**, 169 (1999).
15. R. Ahluwalia, T. Lookman, A. Saxena, and W. Cao, *Appl. Phys. Lett.* **84**, 3450 (2004).
16. Y.M. Jin, Y.U. Wang, A.G. Khachatryan, J.F. Li, and D. Viehland, *Phys. Rev. Lett.* **91**, 197601 (2003); *J. Appl. Phys.* **94**, 3629 (2003).
17. Y.U. Wang, *Phys. Rev. B* **73**, 014113 (2006);
18. Y.U. Wang, *Phys. Rev. B* **74**, 104109 (2006);
19. Y.U. Wang, *Phys. Rev. B* **76**, 024108 (2007).

20. H. Wang, J. Zhu, N. Lu, A. A. Bokov, Z. G. Ye, and X. W. Zhang, *Appl. Phys. Lett.* **89**, 042908 (2006).
21. A. Amin, M.J. Haun, B. Badger, H. McKinstry, and L.E. Cross, *Ferroelectrics* **65**, 107 (1985).
22. T. Fett and D. Munz, *J. Testing Evaluation* **28**, 27 (2000).
23. X. Ren and K. Otsuka, *Phys. Rev. Lett.* **85**, 1016 (2000).
24. F. Jona and G. Shirane, *Ferroelectric Crystals* (Pergamon Press, Oxford, 1962).
25. Y.L. Li, L.E. Cross, and L.Q. Chen, *J. Appl. Phys.* **98**, 064101 (2005).

# Chapter V

## Piezoelectricity under External Fields

### V.1. Introduction

Since single crystals of MPB-based ferroelectrics are either unavailable or too expensive, polycrystalline ceramics are widely applied to manufacture high-performance electromechanical devices. Usually, untextured ferroelectric polycrystals with random distribution of grain orientations exhibit isotropic macroscopic properties that are independent of directions. These materials, if properly “poled” along an arbitrary direction by electric field, can exhibit anisotropic properties. They possess low-symmetry phases with several crystallographically equivalent orientation and/or polar variants that form domain microstructures. Without application of external mechanical, or electric field, the domains form with equal probability for all orientation/polar variants, resulting in macroscopic isotropy of the untextured polycrystals. However, within an external field, the energies of crystallographically equivalent variants are no longer equal and the

domains with energetically favorable orientations or polar directions are selected, leading to macroscopic anisotropy of the untextured polycrystals. Such phenomena are sometimes called variant selection in ferroelastics and domain texture in ferroelectrics.

In this chapter, we employ phase field modeling and simulation to study the electromechanical properties of MPB-based ferroelectric polycrystals under externally applied electric and/or mechanical fields. In the first section, we investigate the piezoelectric response of electrically poled polycrystals along the original poling direction and the macroscopic non-polar directions, report single-crystal-like strong piezoelectric anisotropy where the piezoelectricity is significantly enhanced in a non-polar direction rather than the conventional macroscopic polar direction. In the second section, the evolution of domain microstructure and its effects to the macroscopic responses of MPB-based ferroelectric polycrystals are investigated. It is found that while stress alone can not pole the ferroelectric polycrystals, the resulted domain configurations can significantly reduce the required poling electric field. In the last section, both electric and mechanical fields will be applied to the polycrystals, and the resulted macroscopic hysteresis and butterfly loops will be examined. It reveals that the longitudinal piezoelectric coefficient is dramatically increased with the applied compressive stress field approaching a level of initiating the polarization rotations.

## V.2. Anisotropic Piezoelectricity

In this section, phase field model is employed to investigate the poling-induced piezoelectric anisotropy in untextured ferroelectric polycrystalline ceramics with random grain orientations. It is found that the poled ceramics exhibit single-crystal-like strongly anisotropic piezoelectricity, where the maximum piezoelectric response is obtained along a macroscopic nonpolar direction about  $50^\circ$  away from the poling and macroscopic polar direction. This behavior resembles the anisotropy observed in ferroelectric single crystals with engineered domain configuration. The underlying domain microstructures in poled ferroelectric ceramics and their evolutions in response to electric field applied along different directions are examined to explain the observed anisotropy. It shows that extrinsic contributions from preferred domain wall motions between poling-selected domains of favored orientations play a dominant role in piezoelectric anisotropy and enhancement in macroscopic nonpolar direction.

In order to obtain better properties in ferroelectric polycrystalline materials, special processing routes are often employed to achieve a preferred (non-random) distribution of the crystallographic orientations of grains (i.e., texture).<sup>2-5</sup> A textured ferroelectric polycrystal exhibits anisotropic properties, e.g., the material's macroscopic response to external stimulus depends on the direction along which the measurement is performed. Alternatively, electric poling of ferroelectric polycrystals is routinely used to render untextured ceramic samples macroscopic piezoelectricity.<sup>6</sup> It is known that the poled untextured samples also possess low-symmetry phases with several crystallographically equivalent orientation and/or polar variants that form domain microstructures, where the

energies of crystallographically equivalent variants are no longer equal and the domains with energetically favorable orientations or polar directions are selected, leading to macroscopic anisotropy of the untextured polycrystals. However, since these materials are conventionally used in the same direction of poling, that is, piezoelectric response is exploited with electric field applied or electric signal measured in the original poling direction, anisotropic piezoelectric responses of poled ferroelectric ceramics poled ceramics are rarely found in literatures. It is thus desirable to investigate this topic by using computer modeling and simulation.

In this section, phase field modeling and simulation are performed to study the piezoelectric responses of ferroelectric ceramics under externally applied electric fields, along the poling direction, as well as macroscopic non-polar direction. In the simulation, the experimentally determined LGD polynomial coefficients,<sup>7</sup> ultrasonically-measured elastic constants,<sup>8</sup> and Rietveld refinement-derived electrostriction coefficients<sup>9</sup> for PZT system at room temperature are applied. We first discuss the piezoelectric responses, or the ferroelectric shape memory effects, in MPB-based ferroelectric ceramics along the poling direction. More interestingly, we also report single-crystal-like strong anisotropy of significantly enhanced piezoelectricity in a nonpolar direction rather than the conventional macroscopic polar direction, which is in striking analogy to the recently discovered piezoelectric anisotropy of ferroelectric single crystals where the best property is obtained along nonpolar rather than polar axes.<sup>10</sup> Since PZT is the current material of choice for a wide variety of high-performance electromechanical devices, and it is intractable for PZT single crystal growth, single-crystal-like property in untextured polycrystalline ceramics is particularly important. Moreover, grain texturing techniques

are more complex and costly than the conventional ceramic poling processes, thus the finding of single-crystal-like property in untextured polycrystals has important implication in both fundamental understanding and technological application of piezoelectric ceramics.

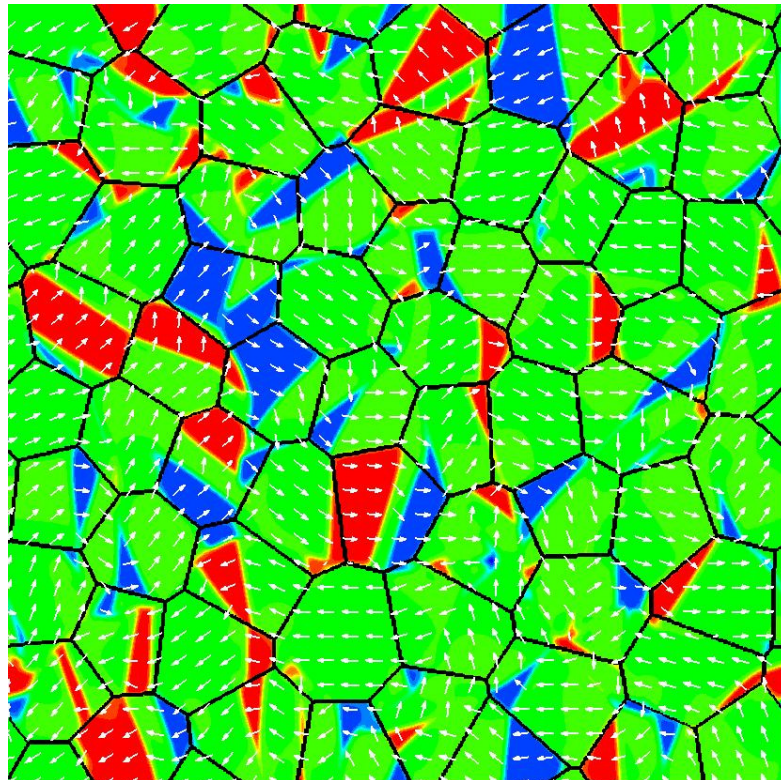


FIG. 5-1. A typical domain microstructure in a MPB-based ferroelectric polycrystal of randomly oriented 64 grains. Arrows represent the in-plane components of polarization vector, and the out-of-plane component is represented by color, where green domains are tetragonal phase, and red and blue domains are rhombohedral phase, the grain orientations are indicated by the arrows in green regions.

In this and the following sections, a two-dimensional polycrystalline structure of 64 grains is first generated by Voronoi tessellations,<sup>11-14</sup> with random grain orientations specified by the rotation matrixes assigned to all computational grids, as described in chapter 2. The grain structure is then simulated with computational grids of 512×512,



without varying the rotation matrixes, as shown in Fig. 5-1. Figure 5-1 shows a typical domain microstructure for a MPB-based ferroelectric polycrystal cooling across Curie temperature. It clearly shows that the bridging domains are usually developed around grain boundaries and their junctions, especially for grains with larger misorientations.<sup>14-15</sup>

Our simulation shows that under an external electric field, the bridging domains usually sever as starting points, and the growth of favorable domains of either metastable or stable phases at the expense of adjacent domains is the major process for adjusting the domain configuration to reduce the total free energy. Under small electric fields, it is shown that evolution of domain microstructures is reversible, which produces the ferroelectric shape memory effects.<sup>15</sup> However, since defects are not considered, the constraints imposed by grain boundaries alone can only trap the randomly evolved domain configuration under small electric fields. Once the driving force provided by externally applied electric field is large enough to overcome the energy barriers among local minima, domain microstructure will evolve to other local minimum states, instead of deviating from its original state. It is worthy noting that, however, upon several cycles of electric fields (training cycles), the mosaic domain microstructure<sup>15</sup> can always find a relative stable state capable of being recovered under electric fields lower than the training fields, as shown in Fig. 5-2. While Fig. 5-2(a) demonstrates that during the training cycles, the domain microstructure experiences several local minima, Fig. 5-2(b) shows that the domain evolution will eventually end up at a relative stable state, and once it gets there, the electric field-strain curve nearly becomes linear and closed (minimizing the energy dissipation). It is noted that, the round segments and small area surrounded by

the curve are due to the electric field applied in a relatively high speed (faster than the polarization switching).

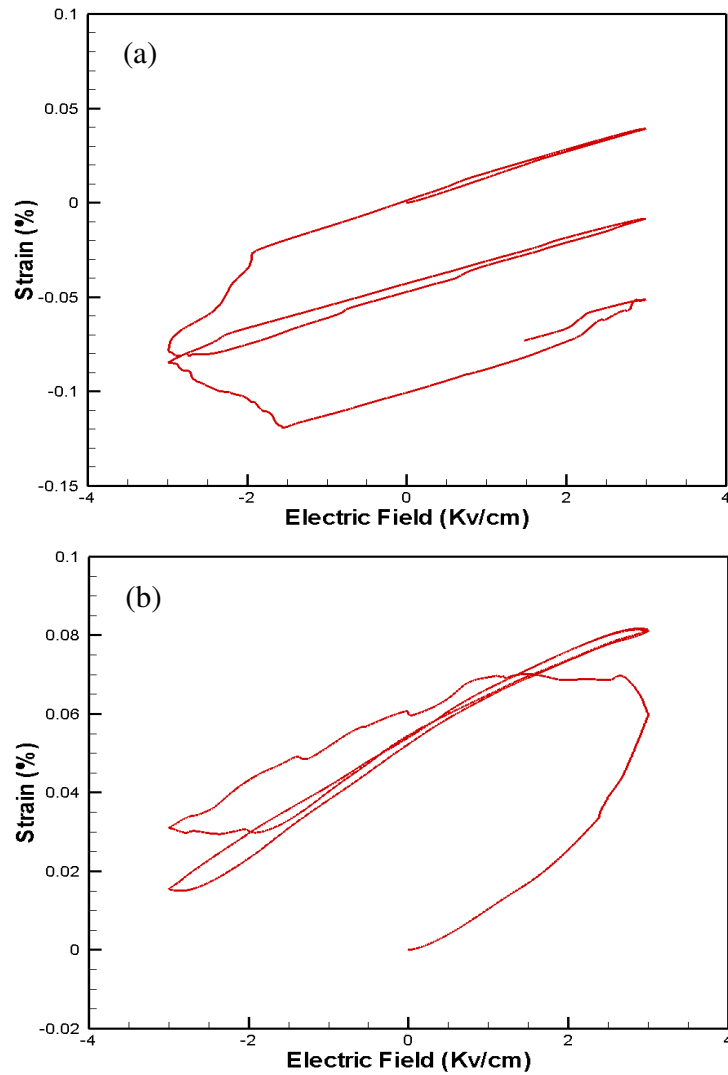


FIG. 5-2. Two typical electric field-strain curves for training MPB-based ferroelectric polycrystals.

The necessity of training cycles in the MPB-based ferroelectric polycrystals suggests that if a large external electric field (should be lower than the coercive fields) will be applied to the polycrystals, a poling process is needed to evolve the domain

microstructures to a very stable state. However, fully poling is not necessary if the polycrystals will only work under low electric fields. Meanwhile, our simulation reveals that the electromechanical property of less poled polycrystals is at least not worse than those fully poled ones, which means fully aligned domain microstructures do not guarantee the best properties.

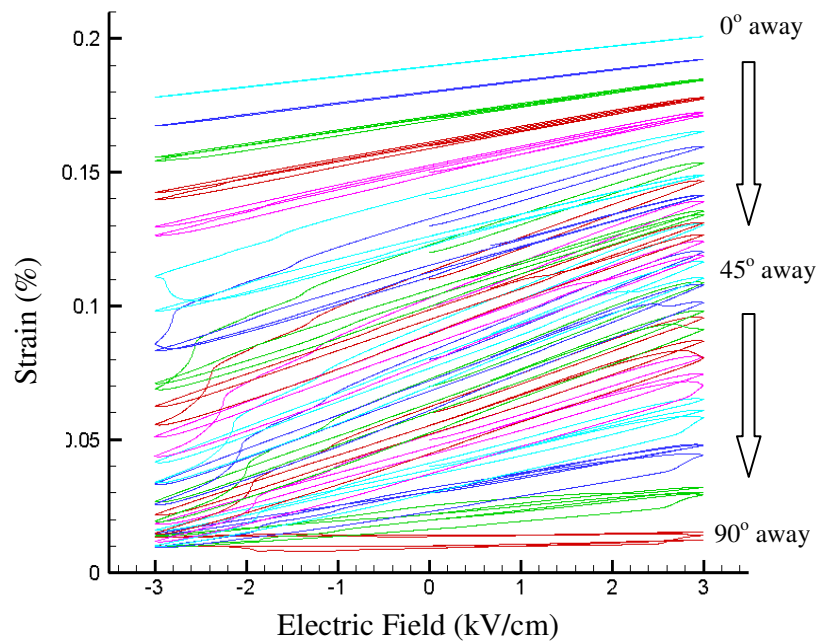


FIG. 5-3. Longitudinal strain versus strength of electric fields for poled ferroelectric polycrystals around MPB. The fields are applied along directions away from the poling direction at a pace of  $5^\circ$ . For clarity, the curves are shifted with different constants.

We rotate the direction of applied electric field to study the piezoelectric anisotropy in ferroelectric polycrystals around MPB. It is interestingly found that the best electromechanical property of the MPB-based ferroelectric polycrystals is along about  $50^\circ$  away from the poling direction, as shown in Fig. 5-3.

To reveal the underlying mechanism of the poling-induced piezoelectric anisotropy, similar simulation is performed for tetragonal phase PZT polycrystals of composition

$x=0.65$  to avoid the complication associated with phase coexistence around MPB, as shown in Fig. 5-4. Figure 5-4 shows a typical poled domain microstructure for a polycrystal with randomly distributed crystallographic [100] and [010] axes and uniform [001] axis. The main feature shown in Fig. 5-4 is that for each individual grain, either two possible tetragonal variants of [100] and [010] form  $90^\circ$  domain structure to macroscopically best align along the poling direction, denoted as  $D_p$ , or a single domain state is reached if the crystallographic [100] axis is close to  $D_p$ .

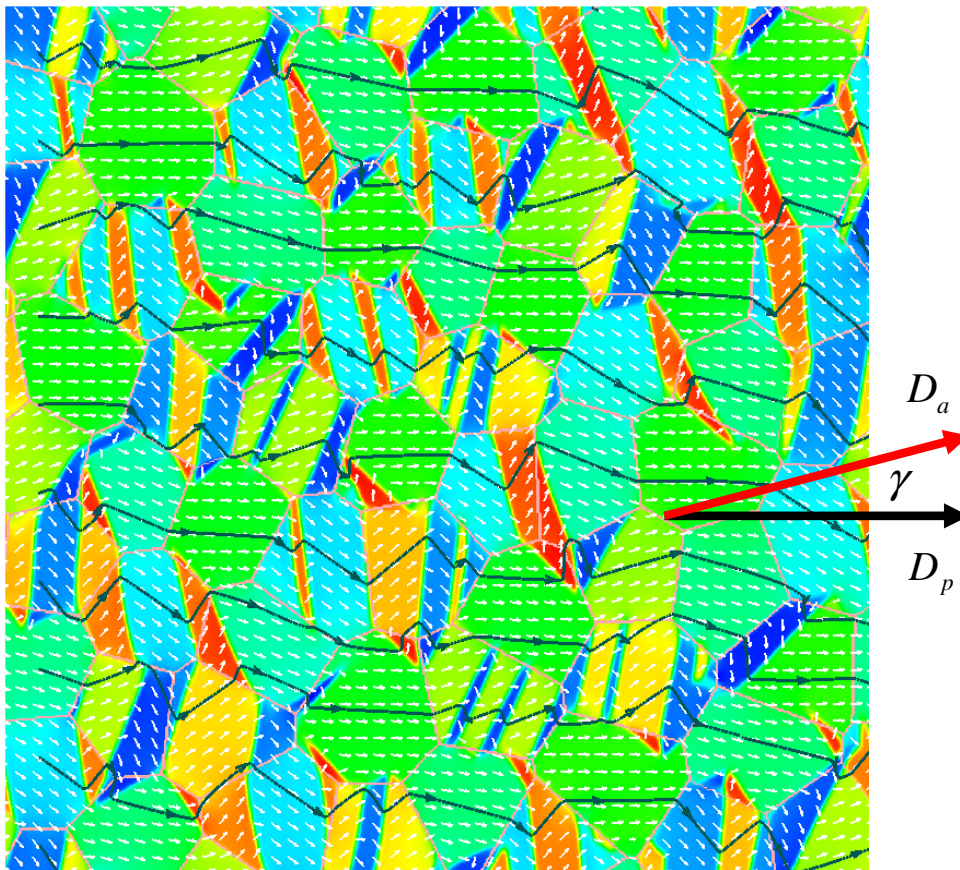


FIG. 5-4. A typical domain microstructure for a poled tetragonal PZT polycrystal ( $x = 0.65$ ). The grain boundaries are depicted by pink lines; vectors represent the local polarizations in each grain. The black streamtraces are to guide to the eyes and show that two possible tetragonal variants of [100] and [010] form  $90^\circ$  domain structure to macroscopically align along the poling direction.

Externally applied electric fields, denoted as  $E_a$ , rotating away from  $D_p$  are then applied to the poled domain configuration, Fig. 5-4. The electromechanical response is plotted in Fig. 5-5. Fig. 5-5(a) shows the longitudinal strain along  $D_a$  versus the strength of electric field applied along  $D_a$ , and Fig. 5-5(b) shows the normalized slopes of those curves versus the angle between  $D_a$  and  $D_p$ , denoted as  $\gamma$ . It is clear that the largest piezoelectricity is obtained when  $\gamma$  is about  $50^\circ$ , which resembles the anisotropy experimentally<sup>10,16</sup> and theoretically<sup>17-19</sup> reported in perovskite single crystals near MPB. However, it is shown that the intrinsic anisotropy theoretically predicted from the LGD polynomials is strong only for rhombohedral compositions with small  $Q_{44}/Q_{11}$ ,<sup>9</sup> where  $Q_{11}$  and  $Q_{44}$  are electrostrictive coefficients. Meanwhile, since the simulated composition is tetragonal and relatively far away from the MPB, the intrinsic explanation for the piezoelectric anisotropy is excluded. This is further confirmed by summing up the piezoelectric response of each individual computational grid under the rotated electric fields. Therefore, it must be the extrinsic contributions, i.e., evolutions of domain microstructure that are responsible for the property enhancements along non-poling directions for ferroelectric polycrystals.

By examining the evolution of domain microstructure, it is found that, while almost no domain wall motion is observed at  $\gamma=0^\circ$ , the most severe domain wall motions are experienced at  $\gamma=90^\circ$ , although almost no net strain is induced in this case. In the cases of  $\gamma \approx 50^\circ$ , some amounts of domain wall motions are noticed, producing the largest strain. Since the strain change induced by extrinsic domain wall motions, or switching variants, is much bigger than that induced by intrinsic elongations of the polarizations, the observation above conceptually suggests that the strain increase at low  $\gamma$

( $0^\circ < \gamma < 50^\circ$ ) is due to the strain contributions from the domain wall motions, and at high  $\gamma$  ( $50^\circ < \gamma < 90^\circ$ ), the strain induced by some domain wall motions is canceled by that induced by others, leading to decreasing the overall strain, or, the macroscopic piezoelectric responses of ferroelectric polycrystals.

Above explanation can be better understood by formulating the strain induced by domain wall motions in an untextured ferroelectric polycrystal. Generally, the poling process will select out three tetragonal variants of [100], [010] and [001] in each grain to form  $90^\circ$  domain walls, as suggested by Fig. 5-4. It shows in Fig. 5-6 that, to equally account for any randomly distributed grain orientations, we define the poling direction ( $D_p$ ) in local crystallographic  $\langle 100 \rangle$  axes by  $\varphi$  and  $\theta$  of values from  $0^\circ$  to  $90^\circ$ , and rotate the field applying direction ( $D_a$ ,  $\gamma$  angle away) along  $D_p$  with  $\omega$  running from  $0^\circ$  to  $360^\circ$ . Thus, the strain of a variant, i.e., [100], in the global poling coordinate system is,

$$g_{ij}^{[100]}(\gamma, \theta, \varphi, \omega) = \varepsilon_{kl}^{[100]} T_{ik}(\gamma, \theta, \varphi, \omega) T_{jl}(\gamma, \theta, \varphi, \omega), \quad (28)$$

where  $T_{ik}(\gamma, \theta, \varphi, \omega)$  is the rotation tensor transforming the local crystallographic axes to the global poling coordinate system, and  $\varepsilon_{kl}^{[100]}$  is the spontaneous strain tensor of tetragonal [100] variant in the local crystallographic coordinate system, coupled to local polarization as,

$$\varepsilon_{11}^{[100]} = Q_{11} P_T^2, \quad \varepsilon_{22}^{[100]} = \varepsilon_{33}^{[100]} = Q_{12} P_T^2, \quad \text{and} \quad \varepsilon_{12}^{[100]} = \varepsilon_{13}^{[100]} = \varepsilon_{23}^{[100]} = 0, \quad (29)$$

Since the poled domain configuration is a stable state under the poling field, the criteria for switching from one variant to others, i.e., from [100] and [010], can be expressed by,

$$C_{010}^{100}(\gamma, \theta, \varphi, \omega) = d_a^{100}(\gamma, \theta, \varphi, \omega) - d_a^{010}(\gamma, \theta, \varphi, \omega) - d_p^{100}(\theta, \varphi) + d_p^{010}(\theta, \varphi), \quad (30)$$

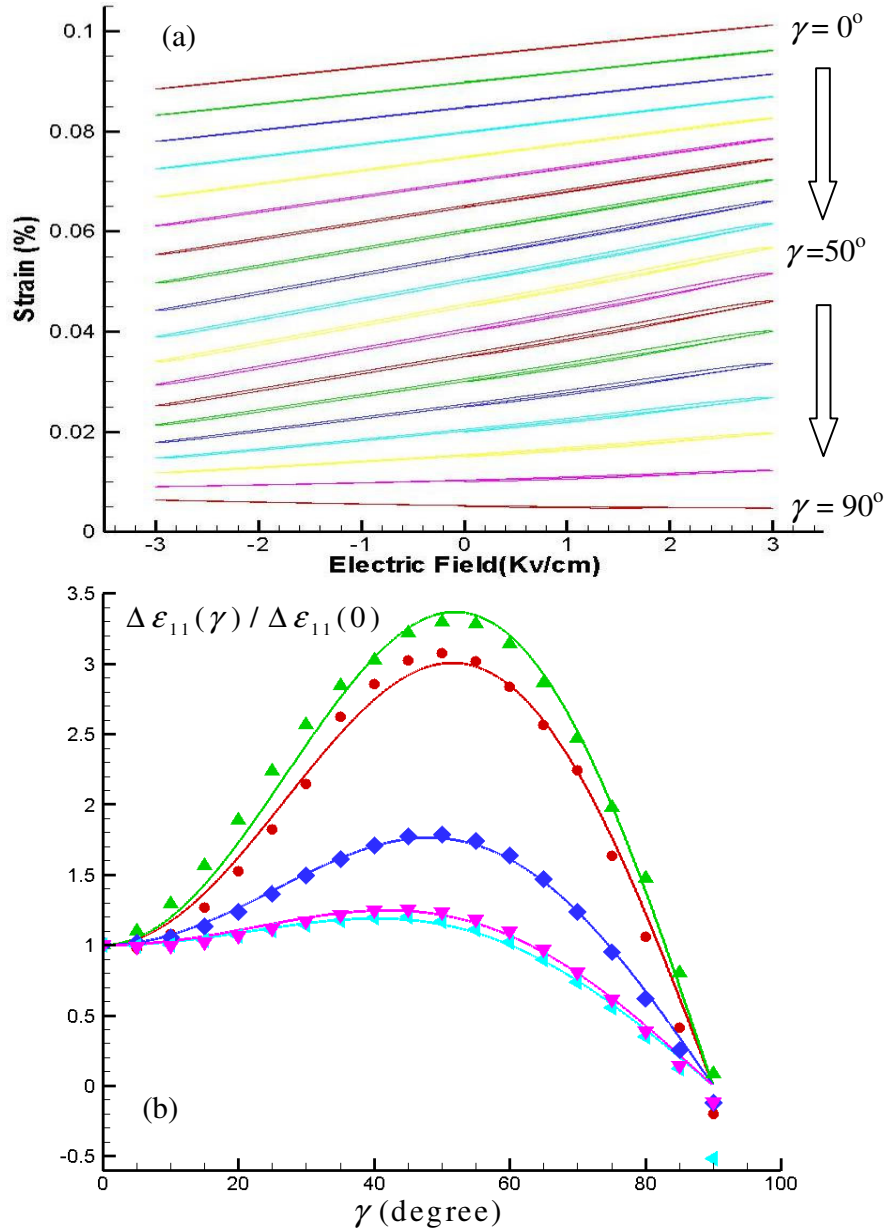


FIG. 5-5. Electromechanical response of poled ferroelectric polycrystals. (a) Longitudinal strain versus the strength of electric field applied along  $D_a$ , where  $\gamma$  increases from  $0^\circ$  to  $90^\circ$  at a pace of  $5^\circ$ . For clarity, the curves are shifted with different constants. (b) Normalized strain difference versus  $\gamma$ , read from figures like (a). Blue points are read from (a), red and green data are for MPB compositions, and purple for rhombohedral composition, and cyan for tetragonal composition with pseudo 3 D grain orientations. The corresponding curves are fitted to Eq. (35) with different  $c$  (7.203, 6.255, 2.963, 1.517, and 1.340).

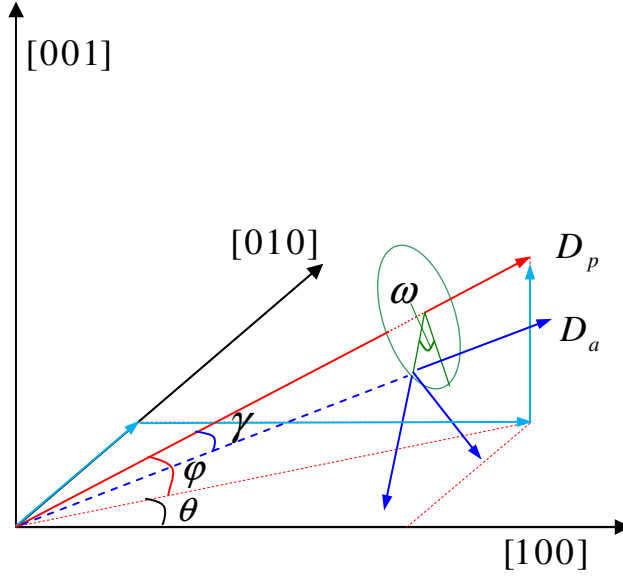


FIG. 5-6. Coordinate system for correlating the crystallographic  $\langle 100 \rangle$  axes (black axes) to the global coordinate system (blue axes) in each individual grain. The cyan vectors are to demonstrate a possible combination of tetragonal variants to align along the macroscopic poling direction.

where  $d_a$  and  $d_p$  are unit vectors along  $D_a$  and  $D_p$ , and the superscript 100 and 010 represent the [100] and [010] components of unit vectors in the local crystallographic coordinate system. Thus, positive  $C_{010}^{100}$  means domain switching from 010 to 100 will occur. If all domain wall motions equally contribute to the final strain change, the total strain change from the domain wall motions can be calculated in the global poling coordinate system as,

$$\begin{aligned}
 \Delta \varepsilon_{ij}^{ex}(\gamma) = & \frac{2}{\pi^3} \int_0^{\frac{\pi}{2}} \int_0^{\frac{\pi}{2}} \int_0^{2\pi} \text{Sign}(C_{010}^{100})(g_{ij}^{100} - g_{ij}^{010}) d\omega d\varphi d\theta \\
 & + \frac{2}{\pi^3} \int_0^{\frac{\pi}{2}} \int_0^{\frac{\pi}{2}} \int_0^{2\pi} \text{Sign}(C_{001}^{100})(g_{ij}^{100} - g_{ij}^{001}) d\omega d\varphi d\theta, \\
 & + \frac{2}{\pi^3} \int_0^{\frac{\pi}{2}} \int_0^{\frac{\pi}{2}} \int_0^{2\pi} \text{Sign}(C_{100}^{010})(g_{ij}^{010} - g_{ij}^{001}) d\omega d\varphi d\theta
 \end{aligned} \tag{31}$$



For  $\Delta\epsilon_{11}(\gamma)$ , it shows in Fig. 5-7 that the numerical solution of Eq.(31) can be approximated by a constant times of the analytical solution for the case shown in Fig. 5-4, where  $\varphi = \omega = 0$ , and

$$\Delta\epsilon_{11}^{ex}(\gamma) = \frac{4}{\pi} (Q_{11} - Q_{12}) P_T^2 \cos \gamma \sin \gamma, \quad (32)$$

The external electric field applied along  $D_a$  can be decomposed to two components of perpendicular and parallel to  $D_p$ , written as  $E_{\perp} = E \sin \gamma$  and  $E_{\parallel} = E \cos \gamma$ , respectively. If assuming that the amount of extrinsic domain wall motions is proportional to  $E_{\perp}$ , and the amount of intrinsic polarization elongation is proportional to  $E_{\parallel}$ , the total strain change induced by applying electric field is,

$$\Delta\epsilon_{ij}(\gamma) = c_{ex} E_{\perp} \Delta\epsilon_{ij}^{ex}(\gamma) + c_{in} E_{\parallel} \Delta\epsilon_{ij}^{in}(\gamma), \quad (33)$$

where  $\Delta\epsilon_{ij}^{in}(\gamma)$  is the intrinsic strain change,  $c_{ex}$  and  $c_{in}$  are two constants. Normalizing Eq. (33), we have,

$$\frac{\Delta\epsilon_{ij}(\gamma)}{\Delta\epsilon_{ij}(0)} = \frac{c_{ex} \Delta\epsilon_{ij}^{ex}(\gamma)}{c_{in} \Delta\epsilon_{ij}^{in}(0)} \sin \gamma + \cos \gamma \frac{\Delta\epsilon_{ij}^{in}(\gamma)}{\Delta\epsilon_{ij}^{in}(0)}, \quad (34)$$

Since the extrinsic contributions to  $\Delta\epsilon_{11}(\gamma)/\Delta\epsilon_{11}(0)$  is considered in this letter, and  $\Delta\epsilon_{11}^{in}(\gamma) < \Delta\epsilon_{11}^{in}(0)$  for tetragonal composition, it is safe to exaggerate  $\Delta\epsilon_{11}^{in}(\gamma)$  by letting  $\Delta\epsilon_{11}^{in}(\gamma)/\Delta\epsilon_{11}^{in}(0) = 1$ . Thus, applying Eq.(32), we have,

$$\frac{\Delta\epsilon_{11}(\gamma)}{\Delta\epsilon_{11}(0)} \approx \frac{c_{ex} \Delta\epsilon_{11}^{ex}(\gamma)}{c_{in} \Delta\epsilon_{11}^{in}(0)} \sin \gamma + \cos \gamma = c \sin \gamma \cos \gamma \sin \gamma + \cos \gamma, \quad (35)$$

where  $c = 4c_{3d}c_{ex} (Q_{11} - Q_{12}) P_T^2 / \pi c_{in} \Delta\epsilon_{11}^{in}(0)$ , and  $c_{3d}$  is a constant that correlates the 3 dimensional Eq.(31) to 2 dimensional Eq(32). Thus,  $c$  is a measure of the ratio of the

strain induced by domain wall motions to that by the intrinsic elongation of polarization in the ferroelectric polycrystals.

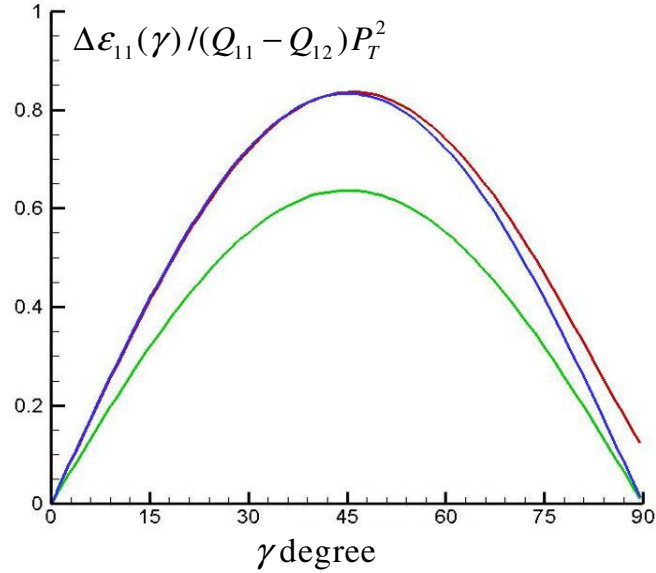


FIG. 5-7. Strain change induced by domain wall motions, where red is the numerical solution for a randomly distributed polycrystal, green is the analytical solution for a polycrystal with fixed [001], and the blue is  $\pi/2.4$  times of green curve.

This model, though very simple, fits very well to the simulation results, as shown in Fig. 5-5(b), even for compositions around MPB and on rhombohedral side, in polycrystals of fixed [001] axes and randomly distributed grain orientations. Thus, it is a general feature of untextured ferroelectric ceramics that domain wall motions play a dominant role in defining the anisotropic piezoelectricity.

It is worth noting that the piezoelectric anisotropy is much higher around MPB, as shown in Fig.5-6(b). This is because the possible tetragonal and rhombohedral variants form bridging domains around MPB<sup>14,15</sup> to better release the constraints imposed by grain boundaries, which is more fragile under the non-polar electric fields, confirmed by

comparing Fig. 5-3 and Fig. 5-5(a). Our simulation and analysis thus suggest that, to exploit the best electromechanical properties in the non-polar directions through preferred domain wall motions, it is necessary to optimize the combination of the density and fragility, or switching ability, of domain walls. This could be achieved by using ferroelectric ceramics of MPB composition/temperature and making the grain sizes distributed in an appropriated range, because appropriate grain sizes around MPB can optimize the amount of individual domains,<sup>14</sup> and domain wall motions around MPB through bridging domain mechanism are easier.<sup>15</sup>

### V.3. Domain Microstructure under Stresses

In this section, phase field modeling and simulation is employed to investigate the domain microstructure evolution of MPB-based ferroelectric polycrystals under variable stresses. It shows that the formation of cross-grains regions is an essential feature of the domain configuration, where the orientations of fairly straight region boundaries are mainly determined by the externally applied stress fields, and the actual grain structure of a ferroelectric polycrystal plays insignificant roles in defining the region formation. It is also revealed that stress alone can not pole the ferroelectric polycrystals, the resulted layered domain microstructure, however, can be utilized as a starting point to reduce the required strength of poling electric field.

The triangular bipolar stress fields are applied to the stabilized ferroelectric polycrystalline sample (Fig. 5-1) to study the pure stress effects on the evolution of domain microstructure. To reduce the dependence of initial configurations, the external stress fields are applied along different directions in the simulations, for example, along the directions of 0, 45, 90, and 135 degree that counterclockwise rotated from the horizontal x axis. Due to the brittleness of ferroelectric ceramics, the tensile stress applied in simulations is in fact impractical in experiments. The reason for applying bipolar stress fields is to study the similarity of the effects of tensile stresses and perpendicular compressive stresses, and thus to facilitate the investigation of the mechanically depoling and “*poling*” effects in the directions parallel and perpendicular to the compressive fields that are usually experienced in applications. To clearly demonstrate the underlying

mechanism of domain switching under externally applied stress field, the simulation results of one and a quarter cycles of stress fields are shown in Fig. 5-8.

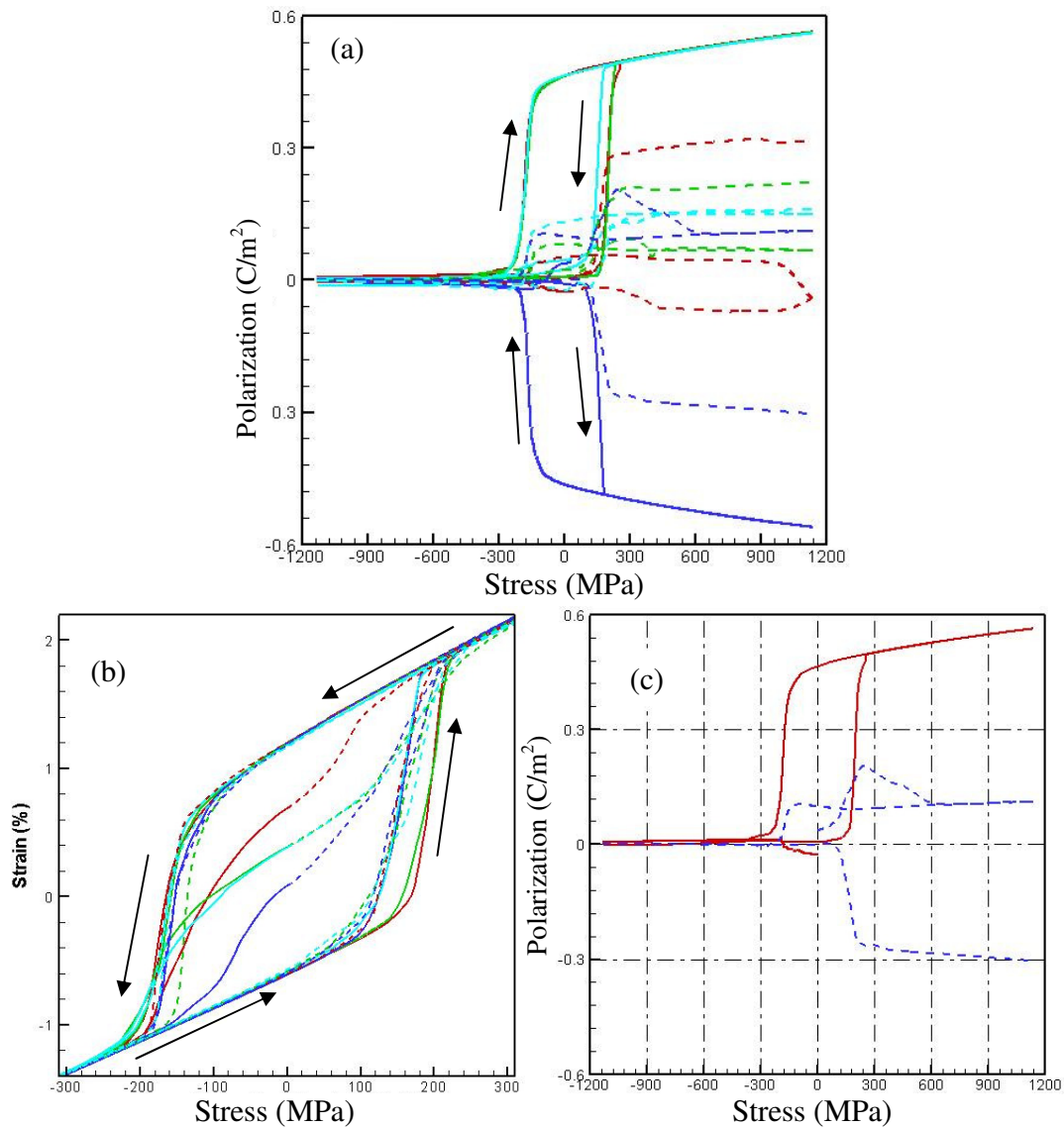


FIG. 5-8. Macroscopic responses of MPB-based ferroelectric polycrystals under mechanical field, where (a) is for averaged polarization versus stress fields, (b) is for stress-strain curves, and (c) is two selected curves in (a), for whom the domain evolution will be discussed. The solid and dashed curves stand for the responses of starting from compression and tension, respectively, the red, green, blue, and cyan curves represent the results of along 0, 45, 90, and 135 degree to the horizontal direction, respectively.

Figure 5-8 shows the macroscopic responses of a ferroelectric polycrystal under pure mechanical loadings, starting from the stress-free configuration shown in Fig. 5-1. In Fig. 5-8(a), the average polarization along the direction of applying field versus the stress field is plotted, where the solid and dashed curves stand for the responses of first applying compression and tension, respectively; the red, green, blue, and cyan curves represent the results of along 0, 45, 90, and 135 degree, respectively. For clarity, the corresponding stress strain curves are only plotted in the stress range of -300MPa and 300MPa, in Fig. 5-8(b), since the trends outside are just linear extensions. It shows in Fig. 5-8(b) that the mechanical behaviors of all cases are nearly isotropic and history independent, the polarization rotation switching processes, corresponding to the points of nonlinearly strain increase, start at about the same stress level.

However, as shown in Fig. 5-8(a), while the depoling effects of compression are consistently observed, the “*poling*” effects of tension are strongly dependent on the loading history. The average polarization under tension of those cases of first applying tensile stresses (dashed curves) are far from the saturate state, whereas, it is shown that the polarization tends to be closer to the saturate value after a compression cycle. Furthermore, the average polarization of those cases of applying compression first (solid curves) is almost saturated after the stress induced switching. It is also shown that the saturated polarization continuously and linearly increase, mainly due to the linear elasticity assumed in computer simulation. This observation seems to suggest that the tensile stress is able to “*poling*” the ferroelectric polycrystals and the previous compressive stress can facilitate this process. However, to our best knowledge, this is not supported by experiments, due to the presence of 180 degree domain walls.

To study the discrepancy, it is necessary to examine the evolution of polar domain microstructures. The domain microstructures of two representative cases (starting from compression along 0 degree and from tension along 90 degree, respectively) at different simulation steps are shown in Figs. 5-9 and 5-10, and the corresponding polarization stress curves are reproduced in Fig. 5-8 (c) for direct comparison.

In Figure 5-9 and 5-10, the grain boundaries are shown by light cyan color. For clarity, the sub-grain phases, for example, tetragonal and rhombohedral phases, are not illustrated; only the in-plane components of certain polarization, selected as one out of 400 computational grids, are represented by arrows with the aid of colors. This visualization method, nevertheless, smears out some detailed information, helps to demonstrate the overall polarization rotation process.

Figures 5-9(a) and 5-10(a) are essentially the same as Fig. 5-1, but in-plane components of polarization vectors are displayed in three categories, as shown by red, blue and green for the vectors close to point-down, point-up and horizontal, respectively. It is noted that, without externally applied fields, three types of cross-grain regions roughly form clusters and distribute with different sizes and irregular shapes. If a stress field is applied to the sample, as 0 degree compression in Fig. 5-9 and 90 degree tension in Fig. 5-10, the stabilized domain configuration is broken and the polarization rotations are initiated through the shrinkage, growth and motions of bridging domains. When the applied field is small, the internal constrains imposed by grain boundaries play important roles in nucleating new bridging domains, shaping the geometries and hindering the growths and motions of bridging domains. If the field becomes large enough to compete

with the internal stress induced by grain boundaries, a severe evolution of polar domain microstructures is observed.

Comparing the Figs. 5-9 (b) to 5-9(a) and Figs. 5-10(b) to 5-10(a), it is shown that while the unfavorable regions, green ones, dramatically decrease in the region number and area, the situations for the equally favored regions, red and blue ones, are complex. When the external mechanical loadings make them grow at the expense of green ones and merge with those of the same color, they also compete with each other. This can be analogous to the grain growth process where the driving force is from reducing the interface area. Thus, if the boundaries between two regions are curved, they are likely to be stretched and an immersed small region tends to be consumed.

It is worthy of note that, the orientations of region boundaries are mainly determined by externally applied stress field, and actual grain configuration of a ferroelectric polycrystal plays insignificant roles in defining region formations. This is more apparent after the stress induced rotation process is suddenly finished, where fairly straight boundaries between red and blue regions pass through different grains with little deviations. Meanwhile, the region boundaries are perpendicular to compressive stress in Fig. 5-9(c) and parallel to tensile stress in Fig. 5-10(c), respectively. Because there are many variants (6 tetragonal variants and 8 rhombohedral variants) in the phase-coexisting composition range, it is expected that the internal stress induced by the grain boundaries can be accommodated easily, which partly explains why straight region boundaries can quite freely cross grains after applying large stress fields.



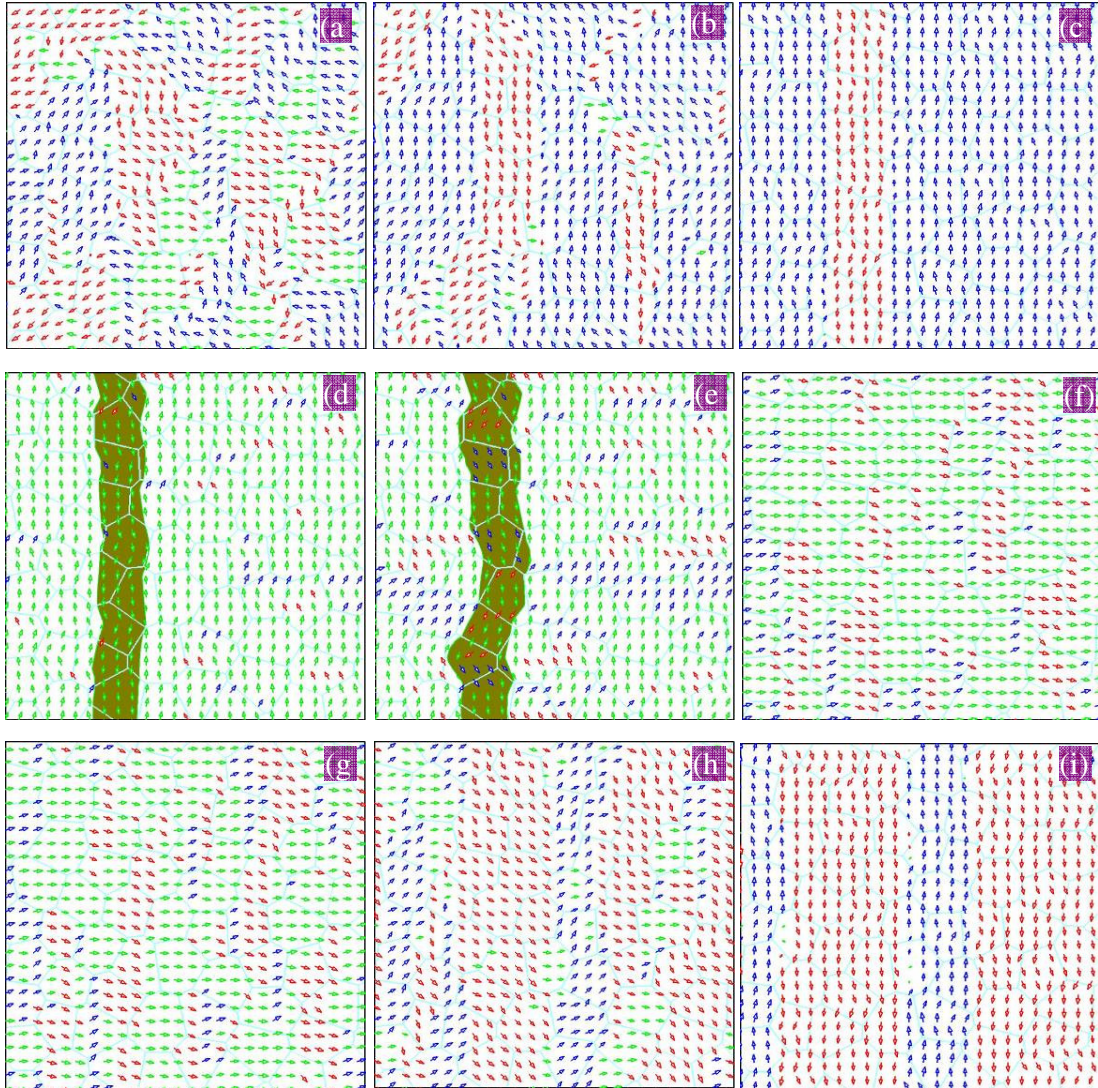


FIG. 5-9. Evolution of domain microstructure of a MPB-based ferroelectric polycrystal under pure mechanical stresses along the horizontal direction. The grain boundaries are shown by light cyan color. For clarity, the sub-grain phases, e.g., tetragonal and rhombohedral phases, are not illustrated; only the in-plane components of certain polarizations, selected as one out of 400 computational grids, are represented by arrows with the aid of colors. The snapshots, from(a) to (i), are corresponding to the solid red curve in Fig. 5-8 (c) with stress states (in MPa) at 0, -160, -320, 0, 160, 320, 0, -160, and -320, respectively.

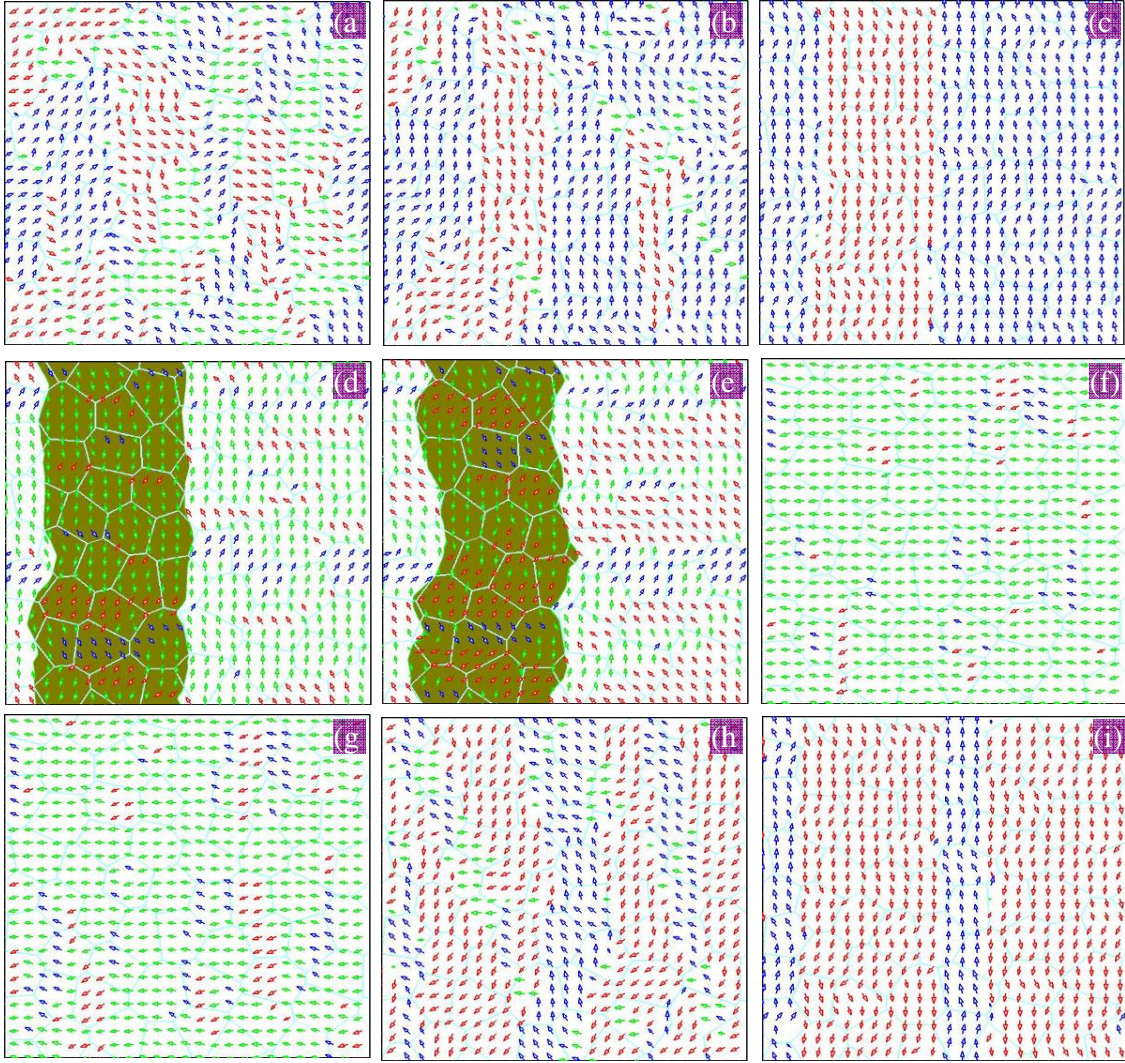


FIG. 5-10. Evolution of domain microstructure of a MPB-based ferroelectric polycrystal under pure mechanical stresses along the vertical direction. The snapshots, from(a) to (i), are corresponding to the dashed blue curve in Fig. 5-8 (c) with the stress states (in MPa) at 0, 160, 320, 0, -130, -320, 0, 160, and 320, respectively.

However, domain microstructures are still confined by the grain boundaries and most of the domain walls are close to either perpendicular (major walls) or parallel (minor walls) directions of applied fields, minimizing the interfacial charge density by satisfying  $\mathbf{n} \cdot (\mathbf{P}^1 - \mathbf{P}^2) \approx 0$ , where  $\mathbf{n}$  is the normal vector of domain wall, and  $\mathbf{P}^1$  and  $\mathbf{P}^2$  are the polarization vectors of two adjacent domains.

The preferred orientations of domain walls and region boundaries do not mean the polarizations in a region are aligned perfectly. In Figs. 5-9 (d)-(e) and 5-10 (d)-(e), the polarizations are depicted by different colors for distinguishing two polarization rotation paths when gradually changing the signs of applying stress fields. It is shown in Figs. 5-9(d)-(f) and 5-10(d)-(f) that, the polarizations switch from vertical to horizontal by either counterclockwise or clockwise rotations. These processes, through nucleation and growth processes, suddenly finish when the stress field reaches some thresholds (see Fig. 5-8(c)). However, because of inevitable misalignments caused by grain misorientations, the growth of existing regions is dominantly observed.

During the growth of favorite regions, it is interesting to note in Figs. 5-9(e) and 5-10(e) that, the boundaries of pre-aligned regions are twisted under oppositely applied stress fields, and stripes are formed inside the pre-aligned regions, with the normal direction parallel to the original region boundaries. As the twisting goes severer, those preferred stripes (red and blue regions) become wider and consume those unflavored (green) regions. When magnitudes of applying fields are close to some threshold values, interaction between matured stripes inside and outside of the shaded regions becomes significant, the balance between alternative stripes is broken, and only favored regions grow.

In general, the interaction is equally in favor of both counterclockwise and clockwise rotations, thus two types of regions (to the left and to the right) should coexist beyond stress threshold, with the boundaries oriented along the stripes. However, it is noted that, for phase field modeling and simulation, when the feature size, for example, the characteristic length of a region in our simulation, is comparable to the computational

size, the periodic boundary condition is satisfied so strictly that some situations with a little less possibility are hard to survive during the microstructure evolution. Thus, there is only one region in one case, as to the left shown in Fig. 5-9(f) and to the right shown in Fig. 5-10(f). The equal favorite is also demonstrated when the sign of applying field changes again. It is shown in Fig. 5-9(i) and 10(i) that, when no interaction between two regions exists, the matured stripes finally develop to layers. The evolution sequences shown in Figs. 5-9 and 5-10 thus explain the microscopic origin of the “poling” effects of tensile stresses and history dependence behaviors of mechanical loadings observed in Fig. 5-8. However, to our best knowledge, mechanical poling of a ferroelectric polycrystal has not been reported in experiments.

This can be explained by the limitations of our simulations. In current work, only several matured regions are developed, which oversimplifies the otherwise complex configuration in a real ferroelectric polycrystal consisting of tons of grains; our model is defects free, it is not easy for some events with a little less possibilities to survive. In order to directly compare with experimental observations, it is thus required to increase the computational size, and/or integrate the pinning effects of defects into our modeling. However, it is beyond the scope of this work to develop a new methodology to consider defects, and impractical to increase the simulations size, due to the extreme computation intensity.

In spite of these difficulties, detailed examination can still be exercised to draw valuable conclusions. The similarities shown in corresponding microstructures in Figs. 5-9 and 5-10, suggest that the in-plane responses of a ferroelectric polycrystal under an externally applied compressive field can also be achieved by applying a tensile field

along the in-plane perpendicular direction. The possibility of evolving into two equivalent states under the influence of the interaction between pre-existing opposite regions ( Figs. 5-9(f) and 5-10(f) ), and that of evolving from one predominant region into multiple-region states (Figs. 5-9(i) and 5-10(i)) suggest that there is no preferred switching path under solely mechanical loadings, and regions with opposite signs will equally exist all the time in real ferroelectric polycrystals. Thus, no poled state can be reached by solely applying mechanical loadings, and there is no history dependence of loading.

After applying compression, the layered domain microstructure is anisotropic. It is expected that the resulted domain configuration can be utilized as a starting point to reduce the required poling electric field, as shown in Fig. 5-11. Figure 5-11(a) shows a MPB-ferroelectric polycrystal forming layered regions after cycles of compression, where the volume fractions of two different regions are approximately half to half. Different strengths of electric fields are applied to the sample along the horizontal and vertical directions, and average polarization along the field applying direction is recorded, as plotted in Fig. 5-11(c) and Fig. 5-11(d), respectively. For comparison, averaged polarization for a sample experienced no stress history (Fig. 5-1) is also recorded in Fig. 5-11(b) for different strengths of applying electric field. It is thus clear that, the strength of electric field for poling a MPB-based polycrystal is reduced when the field is applied along the horizontal direction of the pre-compressed sample, while it is dramatically increased when the field is applied along the vertical direction.

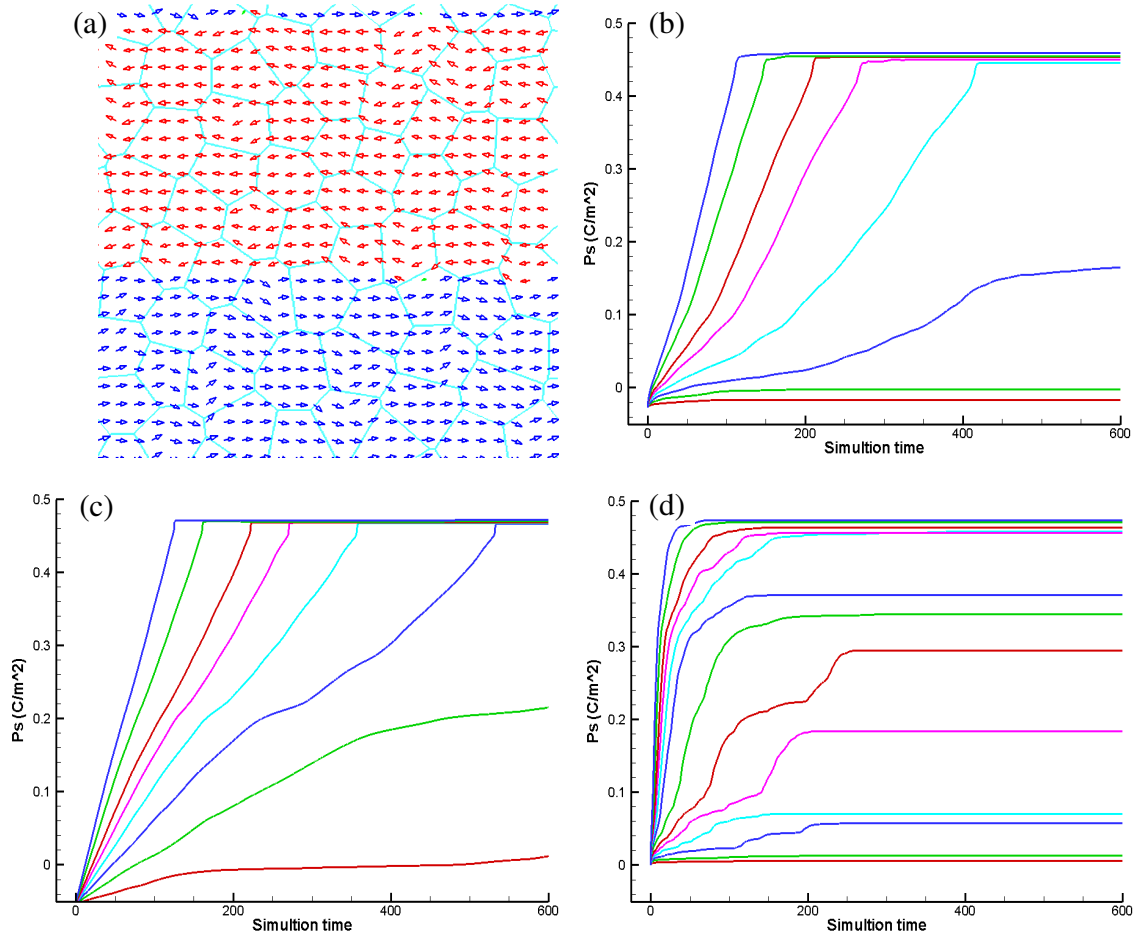


FIG. 5-11. Average polarization of a MPB-based ferroelectric polycrystal under different strengths of externally applied electric fields. (a) shows layered regions for a pre-compressed sample, (b) is for a sample without stress history (see Fig. 5-9(a) for the region information), (c) and (d) are for the sample shown in (a). (b)-(d) record the average polarization under different strengths of electric fields, where the fields are applied along horizontal (b and c) and vertical (d). From lower to upper, the curves in (b)-(c) represent for electric field at 1, 2, 3, 4, 5, 6, 8, and 10 kV/cm, respectively, and the curves in (d) are for electric field at 1, 2, 3, 4, 5, 6, 8, 10, 12, 14, 20, and 25 kV/cm, respectively.

## V.4. Piezoelectricity under Electric and Mechanical Fields

In this section, phase field modeling and simulation is employed to investigate the hysteresis, butterfly loops, and the associated evolution of domain microstructure of MPB-based ferroelectric polycrystals under fixed compressions and variable electric fields. Our simulation shows that the shape and characteristic electric fields and strains for the hysteresis and butterfly loops of the compressed ferroelectric ceramics are significantly modified by the applied compressive stresses, where the formation of cross-grain regions is an essential feature of domain configuration. It is also revealed that longitudinal piezoelectric coefficient can be enhanced by applying compressions, with the best properties found when the compression alone is about to initiate the depolarization process.

In this section, we study the effects of fixed stress on the macroscopic hysteresis and butterfly loops and the evolution of microscopic domain microstructure of a MPB-based ferroelectric polycrystal. Prior to applying electric field, different compressive stresses are applied to the sample, Fig. 5-1. With keeping the compression as constant, triangular bipolar electric fields along the same direction of compression are then applied to the compressively stabilized configuration.

Our simulation shows that the loops under variable electric and fixed stress fields of any direction well represent those of other directions, and the loops will be center-symmetric if averaging the responses of many cycles. To directly correlate to the evolution of domain microstructure and reduce dependences of the initial configuration,

hysteresis and butterfly loops of the second cycle of fields applied along horizontal direction are depicted in Fig. 5-12, which is not completely center-symmetric and somewhat shifted, due to the inevitable dependences of current domain microstructure.

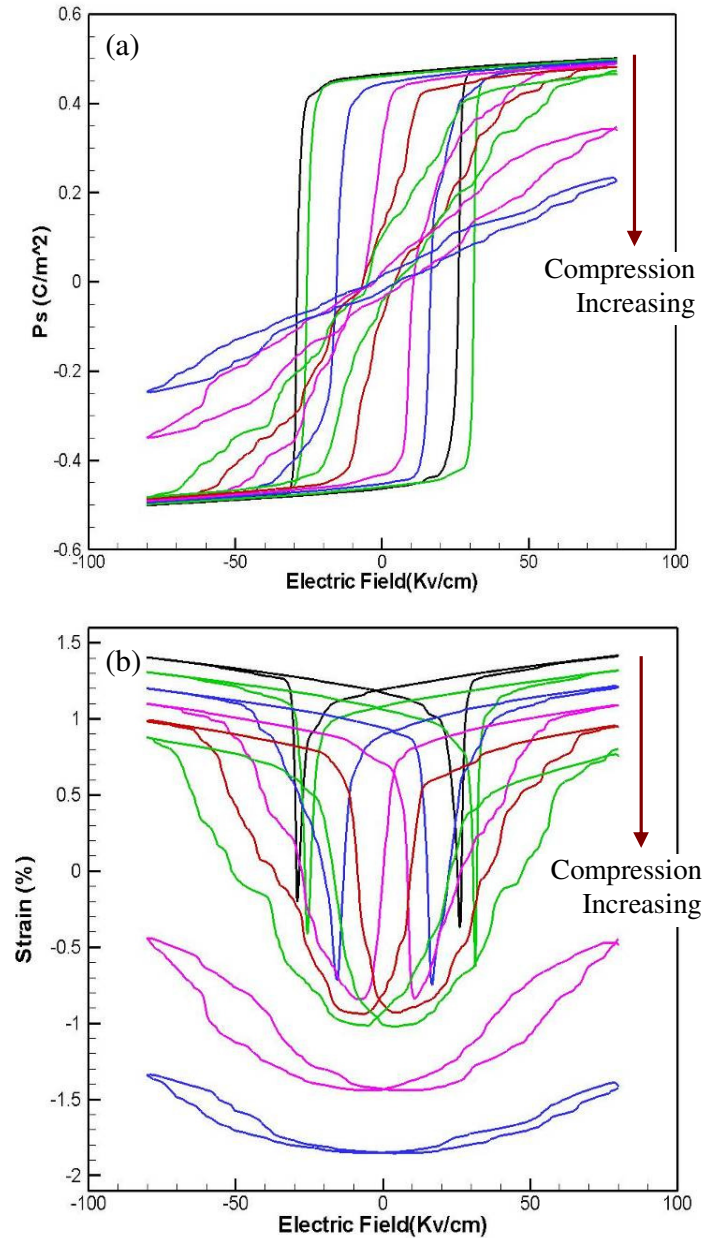


FIG. 5-12. One cycle of typical hysteresis and butterfly loops for MPB-based ferroelectric polycrystals under constant compressions. The corresponding compressions (in MPa) are about 0, -30, -65, -95, -130, -160, -325, and -490 respectively.



Figure 5-12 (a) shows that, with the applied compressive stresses are gradually increased from zero, the areas enclosed by hysteresis loops (hysteresis loss) decrease without significant shape changes; if the magnitude of compression is greater than certain value ( $\sim -80\text{MPa}$ ), the hysteresis loops clockwise rotate significantly, and the enclosed areas quickly decrease; when the applied compressive stresses are overwhelming, the hysteresis loops seem to close up, and become bumpy.

It is worthy to note that, the bumpiness shown in Fig. 5-12(a), as well as in 5-12(b), is come from discontinuous region switching. In other words, as a method to reduce the total energy, the domain microstructures are likely to form regions (clusters) under large compressive stresses, and the polarizations in a region are likely to rotate at the same pace, which causes bumpiness in single-cycle simulation curves. This situation can be alleviated significantly by using a larger computational size and/or averaging the results over several cycles. Thus, the bumpiness is not a real hysteresis behavior of ferroelectric polycrystals under fixed compression.

It is shown in Fig. 5-12(b) that, as the applied compression increasing, the butterfly loops shift down as a whole, and characteristic strains, i.e., lowest strains, strains at zero and maximum electric fields, change dramatically. It is also shown in Fig. 5-12(b) that the shapes of butterfly loops can be roughly separated into three categories, according to the strain changes during the polarization switching processes: (i) sudden needle-like strain changes at low compressions, where the suppressive effect of compressions is insufficient, the average polarization quickly pass the lowest strain states that are perpendicular to the external electric fields; (ii) smooth strain changes under large

compressions, due to the extensive polarization suppression, and (iii) neither needle-like nor smooth strain changes when intermediate compressions are applied. It is worthy to note that, since the sudden switching under low compressions is an instable process, the corresponding electric field varies to some extent, and the needle-like shapes may be smeared out in experiments.

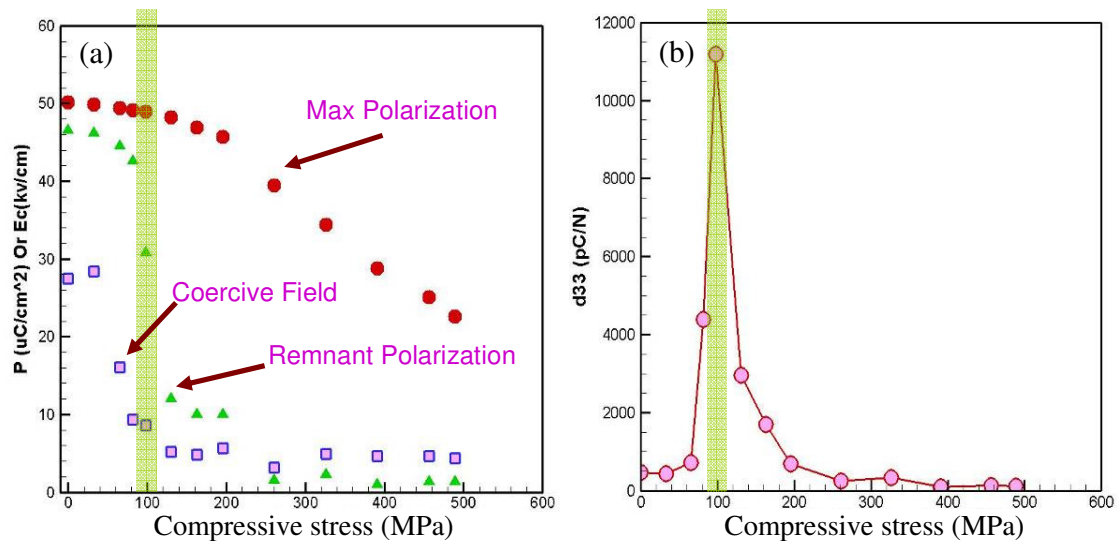


FIG. 5-13. (a) Maximum polarizations (red dots), remnant polarizations (green triangles), coercive fields (pink square), and (b) longitudinal piezoelectric coefficients of MPB-based ferroelectric polycrystals under constant compressions read from Fig. 5-12.

The maximum polarizations, remnant polarizations, coercive fields, and the slopes at zero electric field (corresponding to the slopes of continuously decreasing electric field to the opposite direction) of cases in Fig. 5-12, as well as cases for other stress levels not shown in Fig. 5-12, are read, averaged, and plotted as functions of magnitudes of the applied compressive stresses in Fig. 5-13. Because the model, the LGD polynomial and material constants used in our simulations are not sufficient to describe a real, complex ferroelectric polycrystalline material system, and those values in Fig. 5-13 are taken from

curves of single-cycle-one-direction simulations, large dispersions are expected and serious consideration of those values is not recommended. However, the tendencies shown in Fig. 5-13 are reliable and informative.

Fig. 5-13(a) shows that, while the maximum polarizations smoothly decrease with compression increasing, the remnant polarizations and coercive fields are nonlinearly correlated with the externally applied compressive fields. It is interesting to note that, the magnitudes of compression for dramatically decreasing the remnant polarizations and coercive fields are about -100MPa, close to but a little less than the lowest compression for inducing polarization rotations under pure compression, as shown in Fig. 5-8(b). This finding suggests that externally applied compressive stresses directly influence polarization rotation and hysteresis behaviors of ferroelectric polycrystals.

An interesting enhancement shown in Fig. 5-13(b) is that, the longitudinal piezoelectric coefficient (induced by electric field oppositely applied along the poling direction) is dramatically increased with the compression approaching to a level ( $\sim$  -100 MPa) of initiating the polarization rotation. But on the other side, if further increasing the magnitude of compression, the coefficient drops quickly.

The underlying mechanism of enhancing piezoelectric properties by applying compressive stress can be illustrated by examining the evolution of domain microstructure. Domain microstructures at representative stress levels are shown in Fig. 5-14, where visualization method similar to that used in Figs. 5-9 and 5-10 are employed. For each case, the domain configurations under maximum, zero and coercive electric fields, and under fields of starting significant polarization rotations are arranged according to decreasing the strengths of applying electric fields.

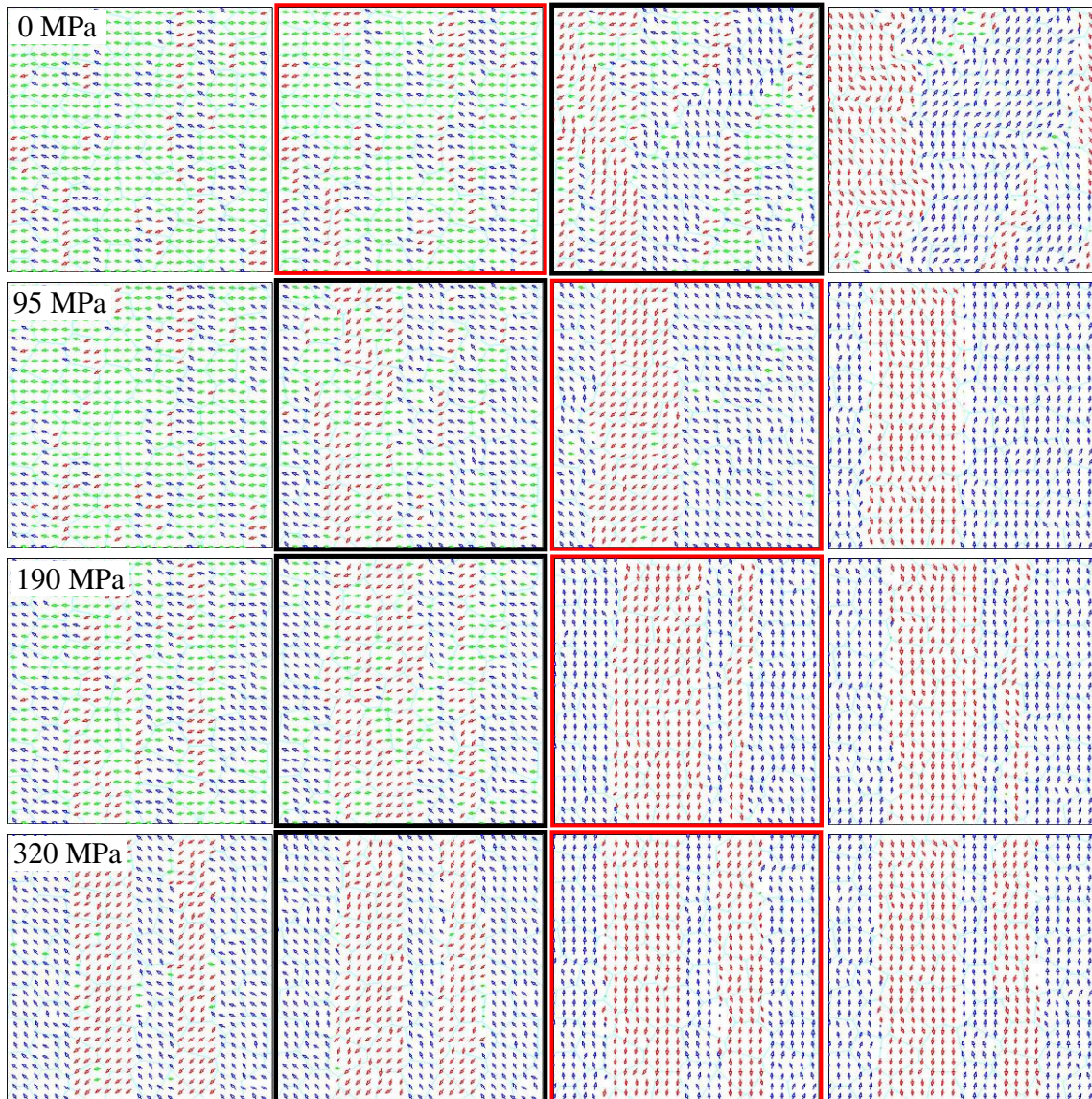


FIG. 5-14. Domain microstructures of a MPB-ferroelectric polycrystal under fixed compression and variable strengths of electric field. For each row, the applied compression is the same, and the applied electric fields decrease from left to the right. From top row to bottom row, the compressions (in MPa) are 0, -95, -190 and -320, respectively. The characteristic electric fields selected for each row are the maximum, zero (red boxes) and coercive electric fields, as well as the electric field of starting significant polarization rotations (black boxes). The corresponding strengths of electric field (in kV/cm) are: 80, 0, -27,-29 for the first row; 80, 3, 0, and -7 for the second row; 80, 33, 0, and -6 for the third row, and 80, 42, 0, and -3 for the last row.

Domain microstructures shown in the first row of Fig. 5-14 are for the case of applying electric field only. The first two figures (under maximum and zero electric fields) essentially have the same domain configurations. It is interesting to note that the red and blue regions in these two figures form stripes, similar to the microstructures shown in Figs. 5-9 (f)-(g), and 5-10(f)-(g), and are normal to the applied electric fields. It is shown that the polarization switching processes are finished by growing the pre-existing stripes. However, this is a deconstruction process. Without the help of compression, the former stripe patterns are gradually distorted when the electric field goes negative, and are completely destroyed under the coercive field. This observation demonstrates a vector-like property of electric fields: unlike tensor-like effect of stress fields discussed in previous section, the electric field has no effect on controlling the domain microstructures in the normal direction of the applied field. That is, there is no microstructure relationship between the in-plane negative electric fields and the in-plane perpendicular electric fields. Therefore, the domain patterns are modified along the perpendicular direction by other constraints, i.e., grain boundaries.

Conceptually, the compressive stress field is to suppress the polarization along the field direction, while the electric field is to rotate it to the direction. Hence, when both fields are applied to a ferroelectric polycrystal, the compression affects the polarization rotation process profoundly. If electric fields and compressive stress fields are along the same direction, stripe formation is an effective way to reduce both electrostatic and elastostatic energies. It is shown in the first column of Fig. 5-14 (under the maximum electric fields) that, the amount of green sites decreases, and red and blue stripes grow and even interconnect as the compression increasing. It is also shown in the last column

of Fig. 5-14 (coercive fields) that under larger compressions, the stripes are straighter, and polarizations inside regions are closer to perpendicular direction.

The domain microstructures shown in black boxes of Fig. 5-14 are right before the sudden polarization rotations. Since under large compression, hysteresis loops are severely rotated, as shown in Fig. 5-12, the point of sudden polarization rotation is weakly defined. Thus, we compare the first three domain microstructures and find that, before overall polarization rotations, the green regions become isolated and the number of sites is, although reduced notably, about the same for three domain configurations. This suggests that the amount of green regions serves as a barrier for overall polarization rotation, the potential for overcoming the barrier is accumulated through growth of pre-existed red and blue stripes, and the overall switching is triggered when the amount of green regions reaches some critical values.

Analyzing the domain microstructure under zero electric field, enclosed by red boxes, is more important for understanding the properties enhancement induced by applying compression, as shown in Fig. 5-13(b). It is shown in the first red box that, under no compression and zero electric field, the polarizations (green regions) of a poled sample are well aligned along the poling direction, with some mild deviations shown as red and blue regions. If we apply a small electric field along parallel or anti-parallel to the poling direction, for aligned polarizations, only intrinsic piezoelectric responses will occur; for mildly deviated polarizations, both intrinsic responses and polarization rotations will take place. Because there are only a few deviated sites and driving force for rotating the mildly deviated polarization is small, the sample intrinsically reacts to external electric field dominantly. Thus, small piezoelectric coefficient is expected under no compression,

due to the small strain induced by intrinsic responses. Our simulation also shows that the amount of deviated sites increases and the deviation becomes severe when the sample is under increasing compressions. More contributions from polarization rotations are expected to enhance the longitudinal piezoelectric coefficient, as shown in Fig. 5-13(b).

When the applied compression is further increased, under zero electric field, the amount of green site decreases and the polarizations are deviated severely from the poling direction, as shown in the second red box of Fig. 5-14. Based on the same arguments, further property enhancement is expected. However, this contribution is not enough to explain the dramatic enhancement demonstrated in Fig. 5-13(b). As examining Fig. 5-12(b) again, it shows that the polarization switching occurs at low electric field, which suggests that the compression “*push*” the domain configuration to a very fragile state (as it is close to phase transition): a small electric field oppositely applied along the poling direction is enough to severely rotate the polarization. Comparing Figs. 5-8 and 5-13, it shows that the most fragile state or the largest longitudinal coefficient is reached when the compression alone is about enough to initiate the depolarization process.

If the applied compression is further increased, although the polarizations are deviated more severely, the depolarized domain microstructures become stable again. Thus excessive suppression effect of compression should be overcome by poling effect of electric field to rotate the polarization, as exemplified in the third red box of Fig. 5-14. If the sample is over-compressed (the last red box of Fig. 5-14), although all polarizations are close to the direction normal to the poling direction, overwhelming suppressive effects of compression are capable to reduce the rotation effectively. As a result, the piezoelectric coefficients is even smaller than that under no compression.

## V.5. References

1. W.F. Rao and Y.U. Wang, “*Poling-Induced Single-Crystal-Like Piezoelectric Anisotropy in Ferroelectric Polycrystalline Ceramics*” (to be published).
2. U.F. Kocks, C.N. Tomé, and H.-R. Wenk, *Texture and Anisotropy: Preferred Orientations in Polycrystals and Their Effect on Materials Properties* (Cambridge University Press, Cambridge, U.K., 1998).
3. J.L. Jones, B.J. Iverson, and K.J. Bowman, *J. Am. Ceram. Soc.* **90**, 2297 (2007).
4. K.J. Bowman, *Mater. Sci. Forum* **157-162**, 43 (1994).
5. G.L. Messing, S. Trolier-McKinstry, E.M. Sabolsky, C. Duran, S. Kwon, B. Brahmaroutu, P. Park, H. Yilmaz, P.W. Rehrig, K.B. Eitel, E. Suvaci, M. Seabaugh, and K.S. Oh, *Crit. Rev. Solid State Mater. Sci.* **29**[2], 45 (2004).
6. B. Jaffe, W.R. Cook, and H. Jaffe, *Piezoelectric Ceramics* (Academic Press, London, 1971).
7. A. Amin, M.J. Haun, B. Badger, H. McKinstry, and L.E. Cross, *Ferroelectrics* **65**, 107 (1985).
8. T. Fett and D. Munz, *J. Testing Evaluation* **28**, 27 (2000).
9. W.F. Rao and Y.U. Wang, “*Intrinsic Electrostrictive and Piezoelectric Properties of Lead Zirconate Titanate (PZT): Analysis of Diffraction Data*” (to be published).
10. S.E. Park and T.R. Shrout, *J. Appl. Phys.* **82**, 1804 (1997).
11. Y.M. Jin, A. Artemev, and A.G. Khachaturyan, *Acta Mater.* **49**, 2309 (2001).
12. Y.U. Wang, Y.M. Jin, and A.G. Khachaturyan, *Acta Mater.* **52**, 1039 (2004).
13. Y.M. Jin, Y.U. Wang, A. Kazaryan, Y. Wang, D.E. Laughlin, and A.G. Khachaturyan, *J. Appl. Phys.* **92**, 6172 (2002).
14. W.F. Rao and Y.U. Wang, *Appl. Phys. Lett.* **92**, 102905 (2008).
15. W.F. Rao and Y.U. Wang, *Appl. Phys. Lett.* **90**, 182906 (2007).
16. S.-E. Park, S. Wada, L. E. Cross, and T. R. Shrout, *J. Appl. Phys.* **86**, 2746 (1999).
17. X. Du, U. Belegundu, and K. Uchino, *Jpn. J. Appl. Phys.* **36**, 5580 (1997).
18. X. Du, J. Zheng, U. Belegundu, and K. Uchino, *Appl. Phys. Lett.* **72**, 2421 (1998).
19. D. Damjanovic, *J. Am. Ceram. Soc.* **88**, 2663 (2005).



# Chapter VI

## Conclusions and Future work

### VI.1. Conclusions

In this dissertation, phase field model is employed to study the underlying mechanism for the enhanced electromechanical properties in single crystals and polycrystals of MPB-based ferroelectrics. A general three dimensional phase field model for ferroelectric polycrystals is first described in Chapter 2. This model is then applied to study the phase-coexisting domain microstructures of MPB-based ferroelectric single crystals and polycrystals in Chapter 3. Chapter 4 is focused on investigating the best electromechanical properties of the MPB-based single crystals through domain engineering. The utilization of the best piezoelectric properties of MPB-based ferroelectric polycrystals is discussed in Chapter 5. Main findings of this dissertation are:

Characteristic multidomain microstructures are reported for coherent phase decomposition (diffusional) in PZT around MPB, where nanoscale lamellar domains of tetragonal and rhombohedral phases coexist with well-defined crystallographic orientation relationships and produce coherent diffraction effects. The simulated

microstructures provide important information for interpretation of diffraction data and identification of phases near MPB. It is demonstrated in the bridging domain mechanism (diffusionless) that minor domains of metastable phase spontaneously coexist with and bridge major domains of stable phase to reduce total system free energy around MPB. The existence of bridging domains also explains the enhanced piezoelectric response in the vicinity of MPBs, and the mosaic domain microstructures can be stabilized by internal mechanical and electric boundary conditions imposed by the grain boundaries, which leads to the grain size effect of phase coexistence, that is, the width of phase coexistence composition range increases with decreasing grain sizes.

A domain wall broadening mechanism is proposed to explain the domain size effect of enhanced piezoelectric properties in domain engineered ferroelectric single crystals. It shows that, under electric field applied along the nonpolar axis, without the domain wall motion, the domain wall broadens and serves as embryo of field-induced new phase, producing large reversible strain free from hysteresis. Our simulation demonstrated that this twin-related domain configuration can be optimized by the controlling the magnitude of electric fields applied along non-polar axis of ferroelectric crystals, because the selection of polar domain variants by external electric field during nucleation of ferroelectric phase transition significantly affects the subsequent domain growth and coarsening kinetics and controls the formation and sizes of twin-related lamellar domains. It is also shown that the engineered domain configuration can be stabilized by the presence of domain-dependent internal electric field associated with the short-range ordering of charged point defects.

It is revealed that the poled ferroelectric polycrystalline ceramics with random grain

orientations exhibit single-crystal-like strongly anisotropic piezoelectricity, where the maximum piezoelectric response is obtained along a macroscopic non-polar direction about  $50^\circ$  away from the poling and macroscopic polar direction. It shows that extrinsic contributions from preferred domain wall motions between poling-selected domains of favored orientations play a dominant role in piezoelectric anisotropy and enhancement in macroscopic nonpolar direction. The simulation on the stress effects on the domain microstructure shows that the formation of cross-grain regions is an essential feature, where the actual grain structure of a ferroelectric polycrystal plays insignificant roles in defining the region formation. Although stress alone can not pole the ferroelectric polycrystals, the resulted layered domain microstructure can be utilized as a starting point to reduce the required strength of the poling electric field. Investigations on the effects of compressions on piezoelectricity of MPB-based ferroelectric polycrystals show that the shape and characteristic electric fields and strains of hysteresis and butterfly loops are significantly modified by the applied compressive stresses, where the formation of cross-grain regions is an essential feature of domain configuration. It is also revealed that longitudinal piezoelectric coefficient can be enhanced by applying compressions, with the best properties found when the compression alone is about to initiate the depolarization process.

## **VI.2. Future Work**

The developed LGD polynomials have been used to predict the intrinsic properties of MPB-based ferroelectrics, and widely employed in the phase field model as a description of the chemical free energy of single-phase, single-domain single crystals. However, as

pointed out in the Appendix, there is a natural concern about the accuracy and applicability of the polycrystalline ceramics-based LGD theory, and our simulation has shown that the position of MPB can not be correctly reproduced by the currently available LGD polynomials. Thus, it is highly desired to have more high quality experimental data to develop more accurate LGD polynomials, especially around MPBs.

It is shown in Appendix that the lattice parameters of PZT vary rapidly near MPB. It is unknown whether this is an intrinsic behavior or instead a result of coherence diffraction effect due to the phase-coexisting nanodomain microstructure. Answers to this question will help better understand the nature of MPB, phase coexistence, PZT phase diagram, and enhanced piezoelectricity near MPB. To further address this important issue, it is thus desirable to conduct three-dimensional simulation to investigate the polyhedral shapes and interface orientations of the coexisting domains, and detailed computational diffraction analysis of the phase-coexisting multi-domain microstructures, i.e., diffusional lamellar domain microstructures and diffusionless mosaic domain microstructures.

It is pointed out that the domain wall broadening mechanism and domain size effect could play a role at nanoscale and be responsible for the superior piezoelectric properties of these materials. Thus, systematic investigation of the domain wall broadening mechanism and enhanced piezoelectric properties in different systems involving ferroelectric tetragonal, rhombohedral and orthorhombic phases in the vicinity of transition temperatures and MPBs will be helpful to better understand the inter-ferroelectric phase transitions.

Our simulation demonstrates that the average domain sizes can be controlled by combining heat treatments with an electric field applied along non-polar direction. In the next step, it will be good to systematically investigate the mechanism of sophisticated thermal-electrical approaches applied in the experiments for varying the domain size, explore the possibilities of combining different heat treatments to further reduce the domain size, and find effective thermal-electrical treatments to optimize the domain configurations for enhanced electromechanical properties in ferroelectric single crystals.

It is found that the configuration of the short range order (original domain configuration) plays a role on the stabilization/recovery process. Thus, further simulations could be carried out to statistically study this effect by varying the volume fraction, the average size of domains in simply twined and complex domain configurations. It is also found that the strength of the short range order field can not be uniform; otherwise, it is difficult to explain the experimentally observed behaviors of aged single crystals. Thus, variable distributions, e.g., Gaussian distributions, of the strength of short range order electric fields could be introduced to explore the possibility of controlling the properties of aged, engineered single crystals. Since complex grain structures provide extra constraints on the evolution of domain microstructures, the stabilization process is expected to be different. Further simulation and analysis on stabilizing the domain microstructures in ferroelectric polycrystals will be helpful for understanding the experimentally observed aging induced stabilization.

Our simulation and analysis suggest that better piezoelectric properties can be achieved along a non-polar direction by making the domain wall fragile and optimizing phase coexistence through the grain size effects. Even for the properties along

conventional poling direction, our simulation suggests that the longitudinal piezoelectric coefficient can be enhanced by simply applying compressions. Since the processing techniques involved in above-mentioned cases are relatively simple, it is desirable to systematically explore those ideas by real material experiments, as well as further computer simulations.

# Appendix

## A.1. Intrinsic Electrostrictive and Piezoelectric Properties

Full sets of phenomenological thermodynamic LGD<sup>3-9</sup> theory have only been developed for the most extensively studied PZT solid solution. The LGD free energy function<sup>3-9</sup> provides a systematic description of the PZT properties, in good agreement with the experimental results of polycrystalline ceramics. However, because of the unavailability of single-domain single crystals of PZT samples, upon which the intrinsic dielectric, piezoelectric, and elastic properties could be directly measured, the polynomial coefficients and relevant material parameters are determined by using indirect methods. It is thus an outstanding and challenging issue to accurate determination of the intrinsic electrostrictive and piezoelectric properties of PZT system over its whole composition range, in particular, near its morphotropic phase boundary (MPB), which can then be used to separate intrinsic and extrinsic contributions to the piezoelectric behaviors of polycrystalline ceramics used in practical applications, clarify the underlying mechanisms, and understand the relationships between domain microstructures and electromechanical properties.

According to the concept of Landau,<sup>10</sup> LGD free energy function describes the nonequilibrium (with equilibrium as a special case at the free energy minimum)

thermodynamic properties of a homogeneous ferroelectric system.<sup>11</sup> That is, LGD theory describes the intrinsic properties of ferroelectric material, in particular, PZT system in a single-phase, single-domain and single-crystal state (i.e., *homogeneous state*). Therefore, the LGD polynomial coefficients and relevant material parameters assume, in principle, the values that are fitted to the experimental data of homogeneous materials, which, however as mentioned above, are not available for PZT. Although care has been taken when fitting the coefficients to polycrystalline ceramics data,<sup>3-9</sup> it is difficult to exclude all extrinsic effects, such as domain wall motions, phase transformations, mechanical and electric boundary conditions associated with the complex grain structures of polycrystalline ceramics, etc. Furthermore, phase coexistence phenomenon is commonly observed around MPB, and the best piezoelectric properties are obtained at compositions near the MPB.<sup>12</sup> It is unclear if the property enhancement at MPB is mainly an intrinsic or extrinsic effect. While the developed LGD theory provides valuable insight into this issue,<sup>3-9,13-15</sup> there is, nevertheless, a natural concern about the accuracy and applicability of the polycrystalline ceramics-based LGD theory when applied to single-phase, single-domain single crystals, due to the above-mentioned reasons.

Electrostriction is an intrinsic property of a ferroelectric material that simultaneously exhibits spontaneous polarization and lattice strain, which are correlated through a fourth-rank electrostrictive coefficient tensor  $\mathbf{Q}$ , as in Eq.(3). Since the elastostatic energy plays an important role on the ferroelectric domain formations and evolutions, the electrostrictive tensor is essential in our model. In principle, if both the lattice parameters and the polarization of a ferroelectric phase are known, the electrostrictive coefficients can be directly determined, which, however, requires accurate structural information of



atomic arrangements as well as electronic distributions of ions in the ferroelectric phase unit cell. Alternatively, the values of  $Q_{ijkl}$  can be derived from macroscopic measurements of electric field-induced strain and polarization on polycrystalline ceramic samples, which, however, inevitably suffers from certain extrinsic effects. With a growing body of experimental data from high-resolution X-ray and neutron diffraction and Rietveld refinement results recently reported in the literature<sup>16-30</sup>, it becomes possible to investigate the intrinsic electrostrictive and piezoelectric properties of PZT directly from an analysis of available diffraction data.

The symmetry property of the electrostrictive coefficient tensor  $\mathbf{Q}$  is determined by the symmetry of high-temperature paraelectric phase. Therefore,  $\mathbf{Q}$  is a fourth-rank tensor of cubic symmetry, which has three independent components  $Q_{1111}$ ,  $Q_{1122}$  and  $Q_{1212}$ , with other nonzero components obtained from them by cubic symmetry operations. The three independent components can be determined from the spontaneous polarization and lattice strain in ferroelectric tetragonal (assuming polarization along [001] to be specific) and rhombohedral (polarization along [111]) phases according to the following relations:

$$\varepsilon_{33}^T = Q_{1111} P_T^2, \quad \varepsilon_3^T = Q_{11} P_T^2, \quad (\text{A.1})$$

$$\varepsilon_{11}^T = \varepsilon_{22}^T = Q_{1122} P_T^2, \quad \varepsilon_1^T = \varepsilon_2^T = Q_{12} P_T^2, \quad (\text{A.2})$$

$$\varepsilon_{23}^R = \varepsilon_{31}^R = \varepsilon_{12}^R = \frac{2}{3} Q_{1212} P_R^2, \quad \varepsilon_4^R = \varepsilon_5^R = \varepsilon_6^R = \frac{1}{3} Q_{44} P_R^2, \quad (\text{A.3})$$

where superscript and subscript  $T$  and  $R$  indicate tetragonal and rhombohedral phases, respectively, and  $P_T$  and  $P_R$  are the magnitudes of spontaneous polarization in respective phases. Both tensor and Voigt matrix notations convenient for engineering application are adopted in Eqs.(A.1)-(A.3). If the lattice parameters and polarization of both

rhombohedral and tetragonal phases are obtained at the same composition and temperature, Eqs.(A.1)-(A.3) completely determine the electrostrictive tensor  $\mathbf{Q}$ .

The spontaneous strain components  $\varepsilon_{33}^T$  and  $\varepsilon_{11}^T$  of tetragonal phase are defined as

$$\varepsilon_{33}^T = \frac{c_t - a_c}{a_c}, \quad \varepsilon_{11}^T = \frac{a_t - a_c}{a_c}, \quad (\text{A.4})$$

where  $c_t$  and  $a_t$  are the tetragonal lattice parameters, and  $a_c$  is the cubic lattice parameter. In evaluating the strains in Eq. (A.4), the parameter  $a_c$  of the cubic paraelectric phase should be extrapolated to the ferroelectric phase temperature, at which  $c_t$  and  $a_t$  are measured. To avoid this ambiguity associated with the extrapolation, instead of  $\varepsilon_{33}^T$  and  $\varepsilon_{11}^T$ , we analyze their difference:

$$\varepsilon_{33}^T - \varepsilon_{11}^T = \frac{c_t - a_t}{a_c}, \quad (\text{A.5})$$

which is insensitive to the value of  $a_c$  extrapolated with different structural models, because of the smallness of spontaneous strain, i.e.,  $a_t < a_c < c_t$  and  $a_t \approx a_c \approx c_t$  within 1%. To be specific, we use  $a_c = \sqrt[3]{\Omega}$ , where  $\Omega$  is the pseudocubic unit cell volume ( $\text{\AA}^3$ ) that is well described by a linear function of composition  $x$  in the range of  $0.1 \leq x \leq 0.8$ , i.e.,  $\Omega = 71.80 - 8.75x$ .<sup>29</sup> It is noted that so-obtained  $a_c$  is used only in Eq. (A.5) but not in Eq. (A.4), because the former is insensitive while the latter sensitive to the value of  $a_c$ .

The spontaneous strain component  $\varepsilon_{23}^R$  of rhombohedral phase is defined as

$$\varepsilon_{23}^R = \frac{1}{2} \left( \frac{\pi}{2} - \alpha \right), \quad (\text{A.6})$$

where  $\alpha$  is the rhombohedral angle. Using the hexagonal cell parameters  $a_H$  and  $c_H$ ,  $\alpha$  is expressed as

$$\alpha = \cos^{-1} \frac{c_H^2 - 6a_H^2}{c_H^2 + 12a_H^2}. \quad (\text{A.7})$$

The spontaneous polarization for tetragonal and rhombohedral phases, defined as dipole moment per unit volume, can be written as,

$$\mathbf{P}_T = \frac{2e}{a_t^2} \left\{ 2 \left[ (1-x) \delta_{Zr} + x \delta_{Ti} \right] - 2\delta_{O_{2,3}} - \delta_{O_1} \right\} \mathbf{z}. \quad (\text{A.8})$$

$$\mathbf{P}_R = \frac{8\sqrt{3}e}{a_H^2} (s + 2t) \mathbf{c}. \quad (\text{A.9})$$

where  $e$  is elementary charge,  $\mathbf{z}$  is a unit vector along tetragonal  $c_t$  axis, the fractional ionic displacements  $\delta$ s are defined with respect to the tetragonal unit cell,  $\mathbf{c}$  is a unit vector along hexagonal  $c_H$  axis, and the fractional ionic displacements  $s$  and  $t$  are defined with respect to the hexagonal cell.<sup>29</sup>

It is worth noting that the above dipole moment as determined from nominal ionic charges and point ion displacements only captures the ionic contribution to the polarization. In fact, the interatomic bonding in PZT exhibits strong covalent character, as reflected by the electronegativity values of respective elements. Thus, Eqs. (A.8) and (A.9) do not take into account the electronic contribution to the polarization. Based on the Rietveld refined lattice parameters and ionic displacements,<sup>16-30</sup> Eqs. (A.8) and (A.9) provide approximation of the polarization, which, together with directly measured values of saturation polarization,<sup>19,31-33</sup> reveal the composition dependence of polarization in PZT system.

We employ the above equations to analyze the diffraction data and Rietveld refinement results reported in the literature<sup>16-30</sup> to evaluate spontaneous strain and polarization from the refined lattice parameters and ionic displacements, from which the electrostrictive coefficients and piezoelectric properties are further calculated.

Figure A-1 plots the lattice parameters of tetragonal and rhombohedral phases within their respective phase stability composition ranges at room temperature. These data points are determined from the diffraction experiments,<sup>16-30</sup> as indicated by different color symbols. Figure A-2 plots the spontaneous polarization of tetragonal and rhombohedral phases within their respective phase stability composition ranges at room temperature. These data points are determined from Eqs. (A.8) and (A.9) and the Rietveld refinement results,<sup>19,20,22-24,27,29,30</sup> as indicated by different color symbols. It is shown that the Rietveld refinement-derived spontaneous polarization, plotted as red and blue dashed curves in Fig. A-2, seems to reasonably describe the general behavior of its composition dependence. (See ref. 1 for more discussions on the analysis of the experimental data).

The electrostrictive coefficients can be determined from the lattice parameters in Fig. A-1 and the spontaneous polarization in Fig. A-2. In particular, for tetragonal phase,  $Q_{11}$ – $Q_{12}$  can be calculated as,

$$Q_{11} - Q_{12} = \frac{c_t - a_t}{a_c P_T^2}. \quad (\text{A.10})$$

For rhombohedral phase, Eqs. (A.3) and (A.6) give

$$Q_{44} = \frac{3}{P_R^2} \left( \frac{\pi}{2} - \alpha \right). \quad (\text{A.11})$$

Fig. A-3(a) plots  $Q_{11}$ – $Q_{12}$  and  $Q_{44}$  within respective tetragonal and rhombohedral composition ranges. The black curves are determined from diffraction data and Rietveld refinement results<sup>16-30</sup> as summarized in Fig. 1 (black solid curves) and Fig. 2 (red and blue dashed curves). The composition ranges of respective phases are determined by the experimental data.

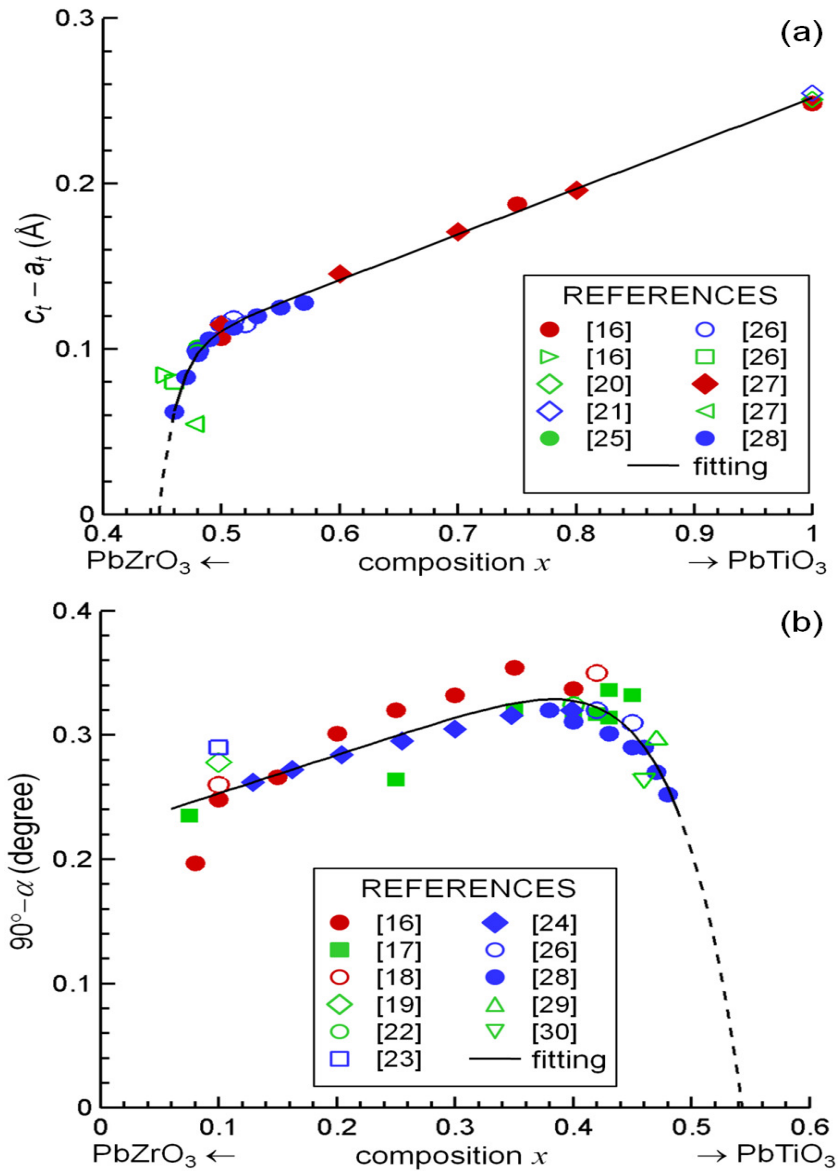


FIG. A-1. (After ref.1) Lattice parameters of tetragonal and rhombohedral phases of PZT within respective phase stability composition ranges at room temperature, as determined from the diffraction data and Rietveld refinement results reported in the literature.<sup>16-30</sup> (a) Tetragonal phase:  $c_t - a_t$ . (b) Rhombohedral phase:  $90^\circ - \alpha$ . Color symbols represent data points and indicate their original experimental literature, as listed in the figure legend. Black lines are fitting curves to guide the eye.

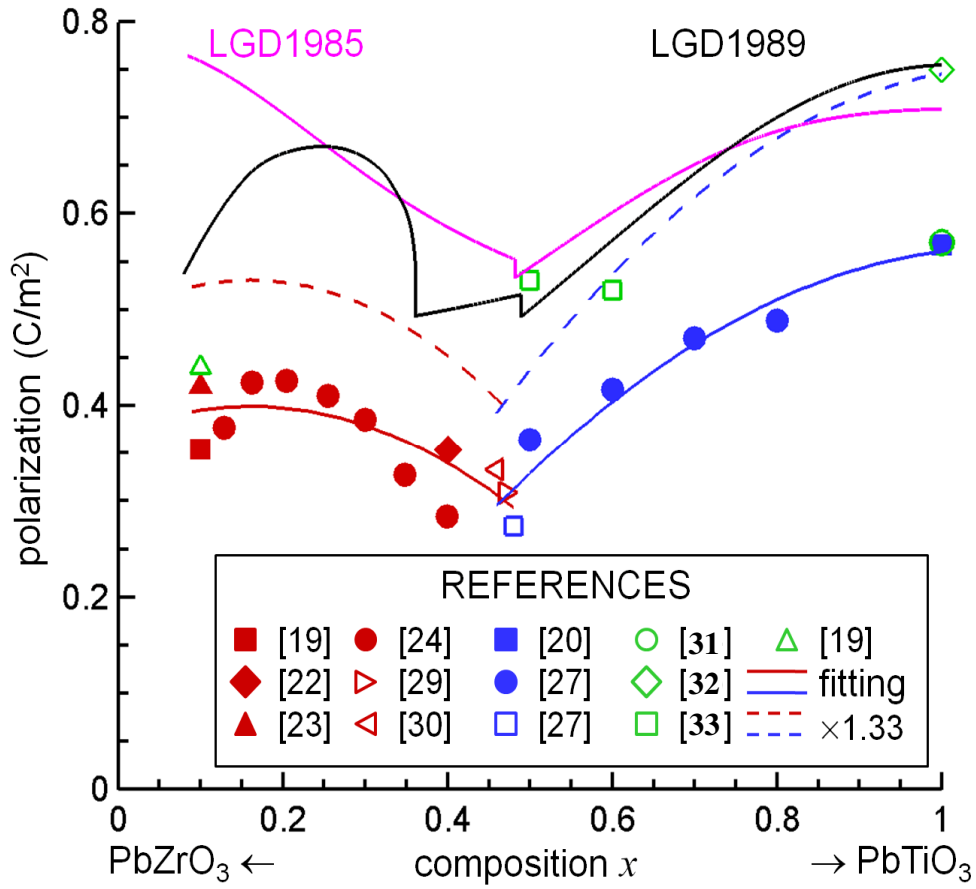


FIG. A-2. (After ref.1) Spontaneous polarization of tetragonal (blue symbols) and rhombohedral (red symbols) phases of PZT within respective phase stability composition ranges at room temperature, as determined from Eqs. (A.8) and (A.9) and the Rietveld refinement results reported in the literature.<sup>19,20,22-24,27,29,30</sup> Saturation polarization (green symbols) from direct experimental measurements<sup>19,31-33</sup> are also shown. Color symbols represent data points and indicate their original experimental literature, as listed in the figure legend. Red and blue solid lines are fitting curves to guide the eye. Red and blue dashed curves are 1.33 times the original fitting curves to coincide with the saturation polarization at end member  $\text{PbTiO}_3$  of composition  $x=1$ .<sup>32</sup> For comparison, purple and black lines plot the spontaneous polarization as a function of composition at room temperature, as obtained from LGD theories,<sup>3-9</sup> where black line takes into account the low-temperature  $F_{R(LT)}$  phase of  $R3c$  space group with oxygen octahedron tilting.

It is worth noting two pronounced features in the composition dependence of electrostrictive coefficients near MPB. First, the electrostrictive coefficients drastically increase when composition approaches MPB from both sides, which is caused by the drastic decrease in spontaneous polarization of both phases with composition approaching MPB, as shown in Fig. A-2. Second, the electrostrictive coefficients suddenly decrease within the MPB composition range, which is caused by the rapid decrease in spontaneous lattice strain (i.e.,  $90^\circ-\alpha$  and  $c_r-a_t$ ) of both phases around MPB, as shown in Fig. A-1. The coexistence of tetragonal and rhombohedral phases around MPB makes it possible to completely determine the electrostrictive coefficient tensor  $\mathbf{Q}$  from the diffraction data.

Fig. A-3(b) plots  $Q_{11}$ ,  $Q_{12}$  and  $Q_{44}$  within the MPB composition range, as shown in black curves. As mentioned above, in order to determine individual  $Q_{11}$  and  $Q_{12}$  from their difference  $Q_{11}-Q_{12}$ , one more relation is required. To this end, we consider the fact that the hydrostatic electrostrictive constant  $Q_h$  of PZT is small around MPB,<sup>9</sup> which means  $Q_{11}/Q_{12}\sim-2$ . We adopt  $Q_{11}/Q_{12}=-2.1$  around MPB,<sup>9</sup> which is used to determine  $Q_{11}$  and  $Q_{12}$  curves shown in Fig. A-3(b). It is worth noting that  $Q_{44}/Q_{11}$  drastically drops from 3.25 to 0.814 across MPB within  $0.45 < x < 0.5$ . This behavior is a direct result of the rapid decrease in spontaneous lattice strain around MPB, i.e.,  $90^\circ-\alpha$  of rhombohedral phase rapidly drops with increasing composition for  $x > 0.4$ , and  $c_r-a_t$  of tetragonal phase rapidly drops with decreasing composition for  $x < 0.5$ , as shown in Fig. A-1. Since tetragonal phase is not observed for  $x < 0.45$  and rhombohedral phase not observed for  $x > 0.5$ ,  $Q_{11}$  and  $Q_{12}$  for  $x < 0.45$  and  $Q_{44}$  for  $x > 0.5$  cannot be determined from above direct diffraction data analysis.

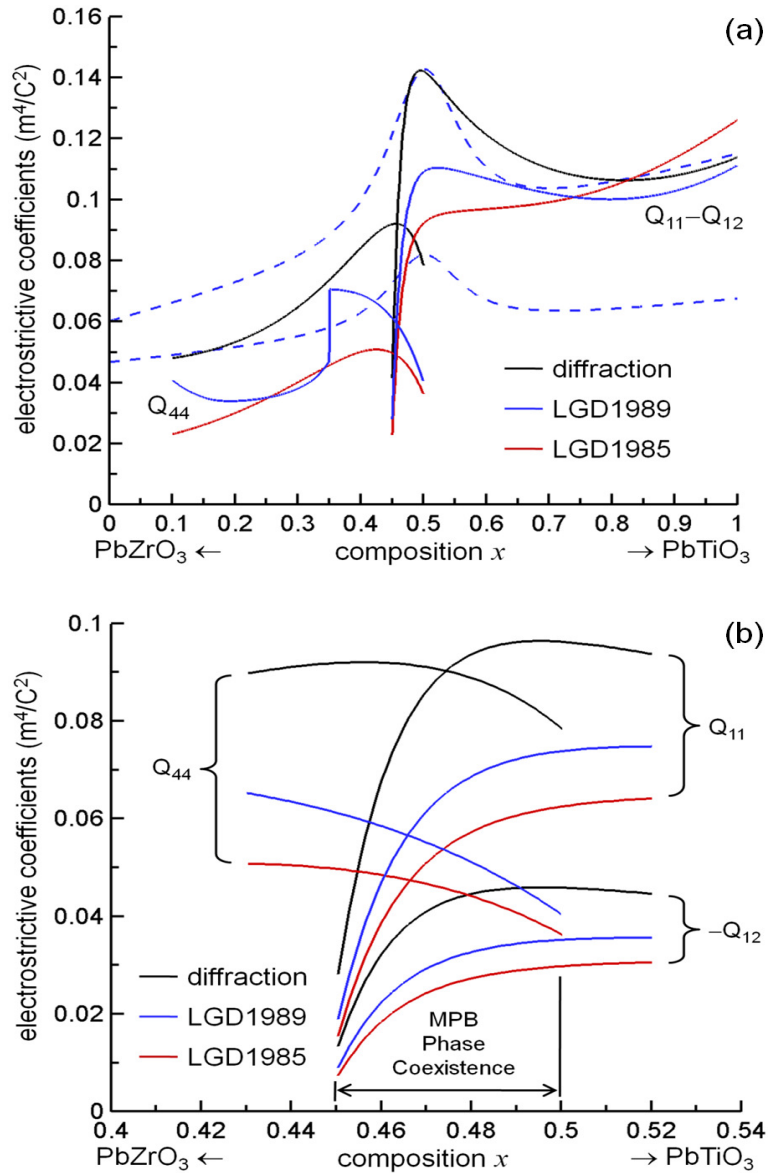


FIG. A-3. (After ref.1) Electrostrictive coefficients of PZT at room temperature, as determined from the diffraction data and Rietveld refinement results reported in the literature.<sup>16-30</sup> (a)  $Q_{44}$  and  $Q_{11}-Q_{12}$  within respective rhombohedral and tetragonal phase composition ranges. (b)  $Q_{11}$ ,  $Q_{12}$ , and  $Q_{44}$  within MPB composition range of phase coexistence. Black curves are determined by using diffraction-derived polarization. Red and blue curves are determined by using polarizations calculated from LGD theories.<sup>3-9</sup> For comparison, the composition-dependent electrostrictive coefficients used in LGD theory<sup>9</sup> are also plotted in (a), as shown in blue dashed curves.



Electrostrictive coefficients are used to calculate spontaneous strain from spontaneous polarization, and to predict piezoelectric coefficients from LGD theory. For this purpose, experimentally-fitted LGD polynomial is needed. As shown in Fig. A-2, the developed LGD theory that takes into account the oxygen octahedron tilting in  $F_{R(LT)}$  phase of  $R3c$  space group<sup>4-9</sup> seems to reasonably describe the general behavior of composition-dependent spontaneous polarization in PZT system; it also provides a good description of the relative free energy states of different phases.<sup>4-9</sup> The developed LGD theory<sup>3-9</sup> has been widely used, which, in fact, is the only theory available for PZT system up to date. Therefore, it is convenient to adopt the LGD theory<sup>3-8</sup> to describe the free energy and spontaneous polarization of PZT system, while recalculate the electrostrictive coefficients based on the diffraction-determined lattice parameters in Fig. A-1. And consequently, using the electrostrictive coefficients in Fig. A-3 together with the corresponding LGD theory<sup>3-8</sup> gives the diffraction-determined lattice parameters and spontaneous strains in Fig. A-1.

In Fig. A-3(a), the composition-dependent electrostrictive coefficients used in LGD theory<sup>9</sup> are also plotted as blue dashed curves for comparison. Discrepancy between the blue solid curves and blue dashed curves is apparent, in particular around MPB, which means that the LDG theory<sup>3-8</sup> does not reproduce well the strain and lattice parameters as directly determined by diffraction experiments.<sup>16-30</sup> To show this, we calculate the lattice parameters  $90^\circ-\alpha$  and  $c_t-a_t$  and plot them as black curves in Fig. A-4. For comparison, we also plot the diffraction-determined lattice parameters in red and blue. It is clear that the LGD theories<sup>2-8</sup> are not accurate around MPB, which could be due to the lack of diffraction data around MPB at the time of the LGD theory development, and implies the

electrostrictive coefficients around MPB are much different to those values reported in literatures.

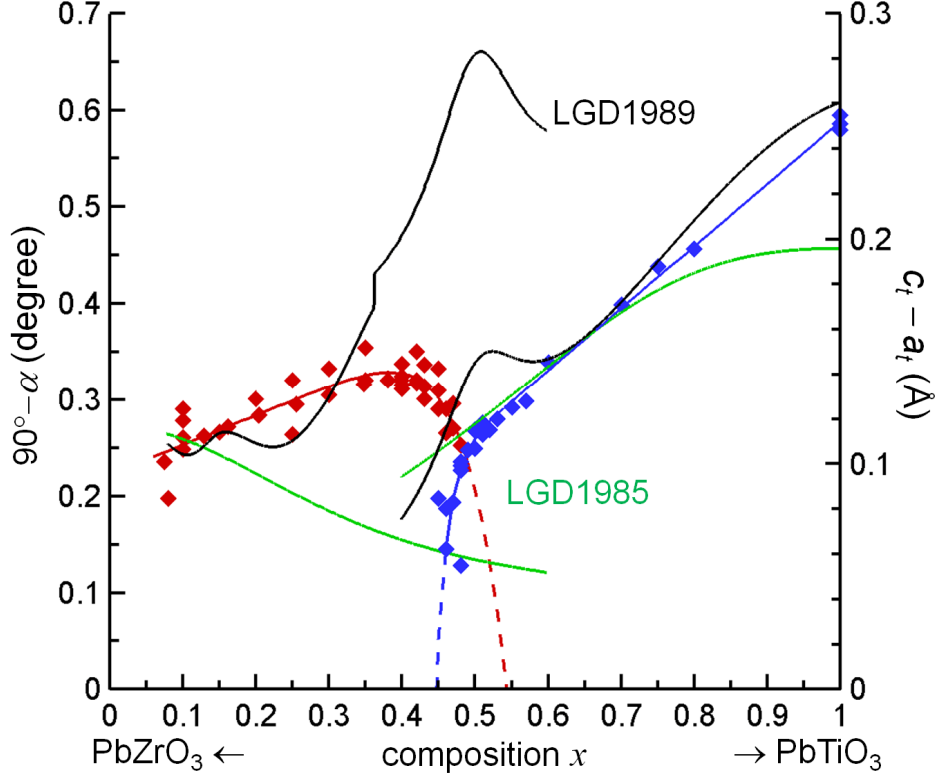


FIG. A-4. (After ref.1) Calculated lattice parameters of tetragonal and rhombohedral phases of PZT by using the LGD theories,<sup>3-9</sup> as shown in black and green lines. The diffraction-determined lattice parameters<sup>16-30</sup> are also shown in red and blue for comparison.

It is worth noting that, since the volume per formula unit  $\text{Pb}(\text{Zr}_{1-x}\text{Ti}_x)\text{O}_3$  is well described by a linear function of composition  $x$  in the range of  $0.1 \leq x \leq 0.8$ ,<sup>29</sup> the equality of the volume strain of tetragonal and rhombohedral phases is expected, and leads to:

$$a_r = \frac{c_t + 2a_t}{3}, \quad (\text{A.12})$$

and

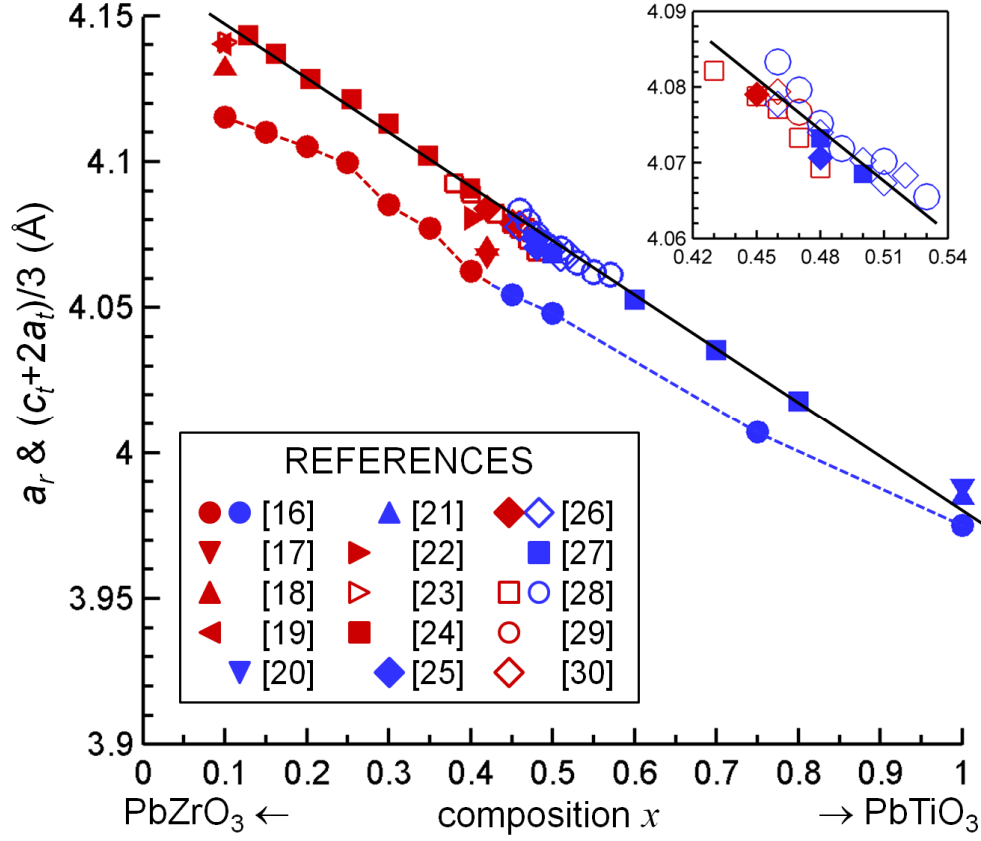


FIG. A-5. (After ref. 2) Rhombohedral lattice parameter,  $a_r$  (red symbols), and weighted average of tetragonal lattice parameters,  $(c_t + 2a_t)/3$  (blue symbols), of PZT as a function of composition at room temperature, as determined from the diffraction data and Rietveld refinement results reported in the literature.<sup>16-30</sup> Color symbols represent data points and indicate their original experimental literature, as listed in the figure legend. Black solid straight lines serve to guide the eye. The inset shows details of data points at MPB. Dashed line emphasizes a systematic deviation of the data in a particular 1952 experiment.<sup>16</sup>

$$P_R = P_T, \tag{A.13}$$

Figure A-5 plots the rhombohedral lattice parameter,  $a_r$ , and weighted average of tetragonal lattice parameters,  $(c_t + 2a_t)/3$ , of PZT as a function of composition at room

temperature. It is shown, especially in the inset, that the data points are well distributed along a straight line,<sup>2</sup> and confirms the lattice parameter relationship given in Eq. (A.12). Further analysis on the diffraction data and Rietveld refinement results shows that this relationship also holds well in PMN-PT and PZN-PT solid solutions.<sup>2</sup> Together with the equality of the ionic part of the spontaneous polarization of both phases at MPB, as shown in Fig.A-2, Fig.A-5 and Eq.(A.12) demonstrate the continuity of thermodynamic properties across the MPB, in agreement with the Landau theory of second-order and weak first-order phase transitions at MPB,<sup>34</sup> and support our analysis on the electrostrictive coefficients around MPB.

The piezoelectric properties can be calculated by using the elastic Gibbs free energy function developed in the LGD theory.<sup>4-9</sup> Such calculations have shown strong crystal orientation dependence (i.e., anisotropy) of piezoelectric properties of PZT.<sup>13-15</sup> We follow the approaches provided in the literature<sup>13-15</sup> and calculate the orientation dependence of piezoelectric coefficient  $d_{33}$ . It is shown in Fig. A-6 that the piezoelectric anisotropy is very sensitive to the electrostrictive coefficient ratio  $Q_{44}/Q_{11}$ , which varies significantly with composition around MPB, as shown in Fig. A-3(b).

Fig. A-6 plots the  $d_{33}$  surfaces and the cross-sections as calculated by using the LGD theory<sup>4-8</sup> with different ratios of  $Q_{44}/Q_{11}$ . It is worth noting that for given  $Q_{44}/Q_{11}$  and  $Q_{11}/Q_{12}$ , the value of  $Q_{11}$  only affects the absolute value of the calculated  $d_{33}$  while does not affect its orientation dependence or anisotropy. It shows that, while the maximum  $d_{33}$  is obtained along a direction close to [001] axis of the rhombohedral crystal rather than the polar [111] axis, the anisotropy is sensitive to the ratio  $Q_{44}/Q_{11}$  and decreases with increasing  $Q_{44}/Q_{11}$ . Moreover, for  $Q_{44}/Q_{11}=3$  as shown in Fig. A-6(c), the maximum  $d_{33}$  is

no longer confined to direction close to  $[001]$  axis rather instead is degenerated to all directions forming the same angle with  $[111]$  axis.

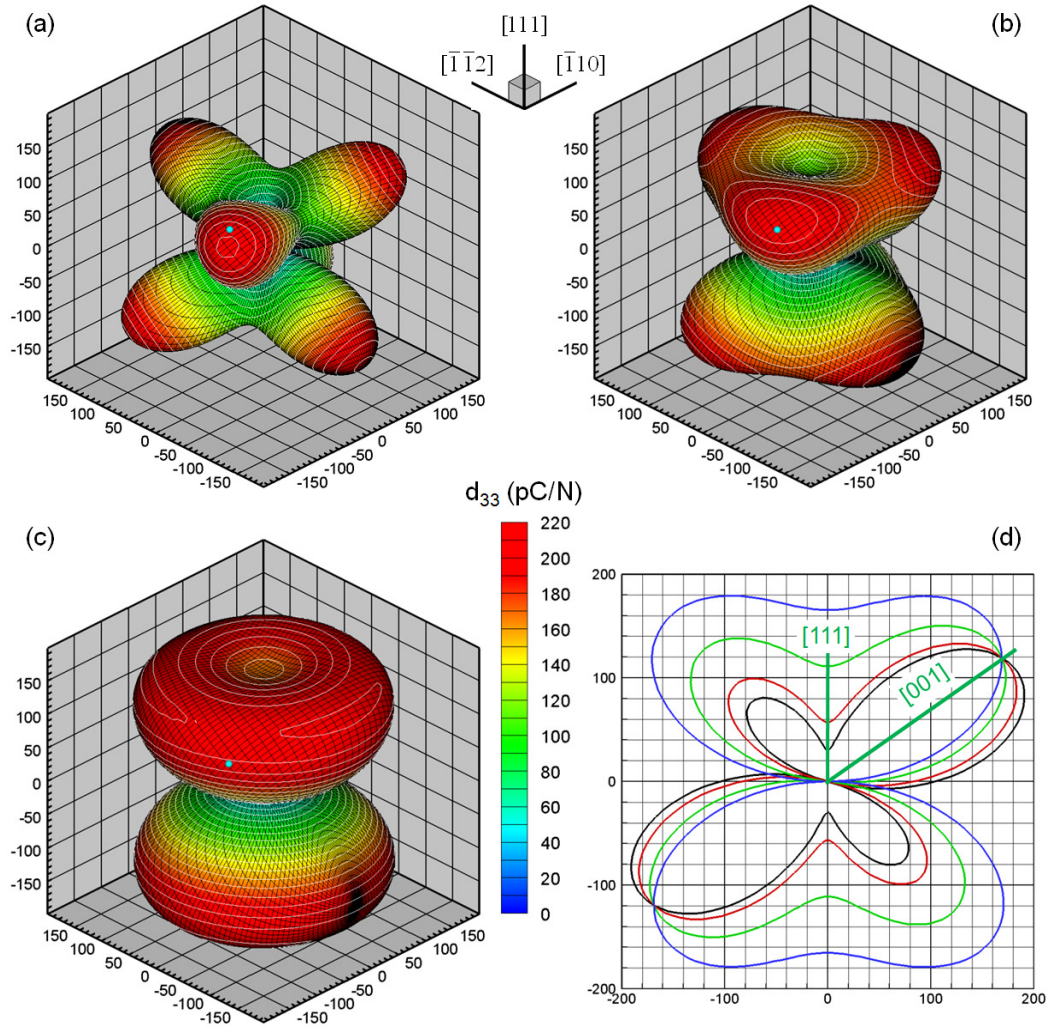


FIG. A-6. (After ref. 1) Effect of electrostrictive coefficient ratio  $Q_{44}/Q_{11}$  on piezoelectric anisotropy of rhombohedral PZT at MPB composition  $x=0.46$ . The orientation-dependent piezoelectric coefficient  $d_{33}$  is calculated by using the LGD theory<sup>4-8</sup> with different ratios: (a)  $Q_{44}/Q_{11}=0.5$ , (b)  $Q_{44}/Q_{11}=2$ , (c)  $Q_{44}/Q_{11}=3$ .  $Q_{11}/Q_{12}=-2.1$ . The cyan symbol on the surface indicates  $[100]$  direction. (d) Cross-sections of the  $d_{33}$  surfaces as cut through  $[111]$  and  $[001]$  directions. Black, red, green and blue curves correspond to  $Q_{44}/Q_{11}=0.5$ , 1, 2 and 3, respectively.

To show the effects of all three electrostrictive coefficients  $Q_{11}$ ,  $Q_{12}$  and  $Q_{44}$  on the piezoelectric anisotropy of PZT, we systematically vary the ratios  $Q_{11}/Q_{12}$  and  $Q_{44}/Q_{11}$  and calculate the orientation-dependent  $d_{33}$  surfaces of rhombohedral PZT. The maximum  $d_{33}$  is found and the ratio of maximum  $d_{33}$  to the  $d_{33}$  along polar [111] axis is evaluated in each case, which is a measure of the degree of piezoelectric anisotropy. Figure A-7(a) plots the piezoelectric anisotropy versus the electrostrictive coefficient ratios  $Q_{11}/Q_{12}$  and  $Q_{44}/Q_{11}$  for MPB composition  $x=0.46$ . It shows that the piezoelectric anisotropy is insensitive to the ratio  $Q_{11}/Q_{12}$ , while is very sensitive to the ratio  $Q_{44}/Q_{11}$ . In particular, piezoelectric anisotropy is very small (i.e.,  $d_{33\text{Max}}/d_{33[111]}\sim 1$ ) for large ratio  $Q_{44}/Q_{11}$ , and becomes strong only when the ratio  $Q_{44}/Q_{11}\sim 1$  and smaller. This is a general behavior for rhombohedral PZT, as observed in the calculations for compositions  $0.4\leq x\leq 0.48$  (the composition range of  $F_{R(\text{HT})}$  phase). Fig. A-7(b) plots the calculation results for composition  $x=0.4$  (cyan) and  $x=0.48$  (purple), and other composition cases are distributed between them (not shown for clarity). For the same ratio  $Q_{44}/Q_{11}$ , larger anisotropy is observed for composition closer to MPB at  $x=0.48$ .

It is worth noting an error in the shear strain as used in the LGD theory,<sup>9</sup> which makes  $Q_{44}$  smaller by a factor of  $\pi/2$ ,<sup>35</sup> and predicts very strong piezoelectric anisotropy,<sup>13-15</sup> as demonstrated in Fig. A-7. Thus, it is believed that the enhanced properties along the non-polar direction are not exclusively from the intrinsic responses of MPB-based ferroelectrics, and can only be fully explained together with the extrinsic contributions, e.g., the evolutions of complex domain microstructures around the MPB.

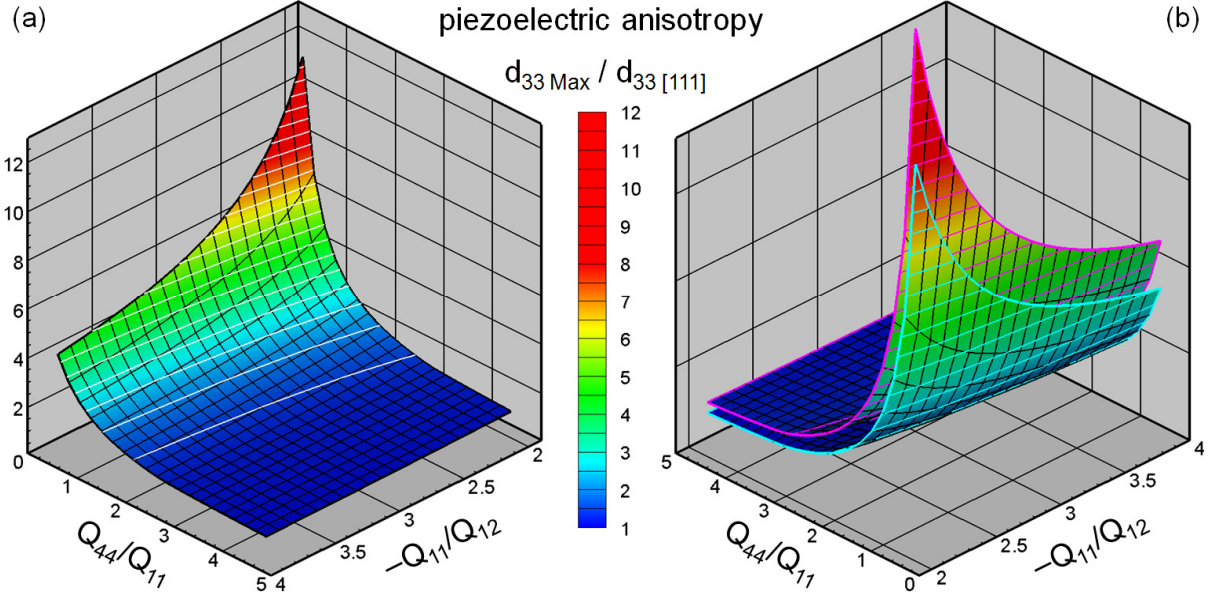


FIG. A-7. (After ref. 1) Effect of electrostrictive coefficients  $Q_{11}$ ,  $Q_{12}$  and  $Q_{44}$  on piezoelectric anisotropy of rhombohedral PZT at composition range  $0.4 \leq x \leq 0.48$ . (a)  $x=0.46$ . (b)  $x=0.4$  (cyan) and  $0.48$  (purple). The orientation-dependent piezoelectric coefficient  $d_{33}$  is calculated by using the LGD theory<sup>4-8</sup> with different ratios  $Q_{11}/Q_{12}$  and  $Q_{44}/Q_{11}$ . The ratio of maximum  $d_{33}$  ( $d_{33\text{Max}}$ ) to  $d_{33}$  along polar [111] axis ( $d_{33[111]}$ ) is plotted as a measure of the degree of piezoelectric anisotropy.

### A.3. References

1. W.F. Rao and Y.U. Wang, “*Intrinsic Electrostrictive and Piezoelectric Properties of Lead Zirconate Titanate (PZT): Analysis of Diffraction Data*” (to be published).
2. W.F. Rao and Y.U. Wang, “*Continuity around MPB*” (to be published).
3. A. Amin, M.J. Haun, B. Badger, H. McKinstry, and L.E. Cross, *Ferroelectrics* **65**, 107 (1985).
4. M.J. Haun, E. Furman, S.J. Jang, and L.E. Cross, *Ferroelectrics* **99**, 13 (1989).

5. M.J. Haun, E. Furman, H.A. McKinstry, and L.E. Cross, *Ferroelectrics* **99**, 27 (1989).
6. M.J. Haun, Z.Q. Zhuang, E. Furman, S.J. Jang, and L.E. Cross, *Ferroelectrics* **99**, 45 (1989).
7. M.J. Haun, E. Furman, T.R. Halemane, and L.E. Cross, *Ferroelectrics* **99**, 55 (1989).
8. M.J. Haun, E. Furman, S.J. Jang, and L.E. Cross, *Ferroelectrics* **99**, 63 (1989).
9. M.J. Haun, Z.Q. Zhuang, E. Furman, S.J. Jang, and L.E. Cross, *J. Am. Ceram. Soc.* **72**, 1140 (1989).
10. L.D. Landau and E.M. Lifshitz, *Statistical Physics*, 3rd edition (Pergamon Press, Oxford, 1980).
11. A.F. Devonshire, *Philos. Mag.* **40**, 1040 (1949).
12. B. Jaffe, W. R. Cook, and H. Jaffe, *Piezoelectric Ceramics* (Academic, London, 1971).
13. X. Du, U. Belegundu, and K. Uchino, *Jpn. J. Appl. Phys.* **36**, 5580 (1997).
14. X. Du, J. Zheng, U. Belegundu, and K. Uchino, *Appl. Phys. Lett.* **72**, 2421 (1998).
15. D. Damjanovic, *J. Am. Ceram. Soc.* **88**, 2663 (2005).
16. G. Shirane and K. Suzuki, *J. Phys. Soc. Japan* **7**, 333 (1952).
17. E. Sawaguchi, *J. Phys. Soc. Japan* **8**, 615 (1953).
18. C. Michel, J.M. Moreau, G.D. Achenbach, R. Gerson, and W.J. James, *Solid State Communications* **7**, 865 (1969).
19. A.M. Glazer, S.A. Mabud, and R. Clarke, *Acta Cryst. B* **34**, 1060 (1978).
20. A.M. Glazer and S.A. Mabud, *Acta Cryst. B* **34**, 1065 (1978).
21. S.A. Mabud and A.M. Glazer, *J. Appl. Cryst.* **12**, 49 (1979).
22. A. Amin, R.E. Newnham, L.E. Cross, and D.E. Cox, *J. Solid State Chem.* **37**, 248 (1981).
23. H. Ito, Y. Shiozaki, and E. Sawaguchi, *J. Phys. Soc. Japan* **52**, 913 (1983).
24. D.L. Corker, A.M. Glazer, R.W. Whatmore, A. Stallard, and F. Fauth, *J. Phys.: Condens. Matter* **10**, 6251 (1998).
25. B. Noheda, D.E. Cox, G. Shirane, J.A. Gonzalo, L.E. Cross, and S.E. Park, *Appl. Phys. Lett.* **74**, 2059 (1999).
26. B. Noheda, D.E. Cox, G. Shirane, R. Guo, B. Jones, and L.E. Cross, *Phys. Rev. B*



- 63**, 014103 (2000).
27. J. Frantti, J. Lappalainen, S. Eriksson, V. Lantto, S. Nishio, M. Kakihana, S. Ivanov, and H. Rundlöf, *Jpn. J. Appl. Phys.* **39**, 5697 (2000).
  28. M.R. Soares, A.M.R. Senos, and P.Q. Mantas, *J. Europ. Ceram. Soc.* **20**, 321 (2000).
  29. J. Frantti, S. Ivanov, S. Eriksson, H. Rundlöf, V. Lantto, J. Lappalainen, and M. Kakihana, *Phys. Rev. B* **66**, 064108 (2002).
  30. J. Frantti, S. Eriksson, S. Hull, V. Lantto, H. Rundlöf, and M. Kakihana, *J. Phys.: Condens. Matter* **15**, 6031 (2003).
  31. J.P. Remeika and A.M. Glass, *Mater. Res. Bull.* **5**, 37 (1970).
  32. V.G. Gavrilyachenko, R.I. Spinko, M.A. Martynenko, and E.G. Fesenko, *Fiz. Tverd. Tela* **12**, 1203 (1970) [*Sov. Phys. Solid State* **12**, 1203 (1970)].
  33. K. Tsuzuki, K. Sakata, and M. Wada, *Ferroelectrics* **8**, 501 (1974).
  34. G.A. Rossetti, Jr. and A.G. Khachaturyan, *Appl. Phys. Lett.* **91**, 072909 (2007); G.A. Rossetti, Jr., A.G. Khachaturyan, G. Akcay, and Y. Ni, *J. Appl. Phys.* **103**, 114113 (2008).
  35. Instead of conventional  $\varepsilon_4 = \pi/2 - \alpha$ , engineering shear strain was defined as  $x_4 = (90^\circ - \alpha)/90^\circ$ .<sup>9</sup> Upon converting degree to radian, it shows  $\varepsilon_4 = x_4\pi/2$ . Using  $x_4$  instead of  $\varepsilon_4$  in Eq. (4) results in  $Q_{44}$  smaller by a factor of  $\pi/2$ .